Circular Dichroism of Distorted Structure-Photonic Materials

Masterarbeit aus der Materialphysik

Vorgelegt von
Johannes Hielscher
15. März 2015

Institut für Theoretische Physik
Friedrich-Alexander-Universität Erlangen-Nürnberg

Betreuer: Gerd Schröder-Turk
Matthias Saba

FAU Erlangen
Institute for Theoretical Physics, LS Mecke

Date of submission: March 16, 2015
This edition: Revised for typographical errors, May 2, 2015

Printed on recycled paper
Steinbeis TrendWhite 80

Typeset by LaTeX 2$_{\varepsilon}$
(pdfTeX 3.14159265-2.6-1.40.15, TeX Live 2014/Arch Linux)
from Utopia + Fourier GUTenberg + Heuristica, CM Bright, TX Typewriter

Abstract

The *single Gyroid* is a triply periodic negative curvature surface of BCC cubic symmetry, frequently occurring in nature, *e. g.* in the wing scales of the butterfly *Callophrys rubi*. Within there, it gives rise to structural colour (Simulation parameters are chosen to meet experimental data, to easily embed the work into the context of bio-photonics). The inevitable deviations of biological systems from perfect periodic order, as well as the possible tolerances for synthetic photonic devices adopting Gyroid structures, will motivate the main question of this work: the influence of *distortion* on the Gyroid's photonic properties.

The Gyroid is a handed (chiral) structure, so a natural question is its response to handed light (circular polarisation, CP). As an approach to quantify chiro-optical behaviour, we will introduce and discuss the Cumulative Circular Contrast (CCR) as an appropriate, setup-conscious way to measure CP-light response of media in slab-like geometry.

We will give a comprehensive overview of three distinct Gyroid construction routes: Nodal approximation to TPMS/CMC, **1srs** network graph with finite wire thickness, and assembly from discrete helices, each including analysis of volume filling fraction and characteristic length scales.

A Fourier synthesis approach for a distortion field with finite correlation scales will be developed, and deployed to create geometries derived from the Gyroid via controlled distortion. On these, FDTD simulations are carried out, to measure reflectance and transmission. Additionally, systems with finite absorption or at non-normal incident angle will be included into comparisons.

The ranges of distortion correlation will be probed and discussed, with a focus on the Cartesian [001] direction of the Gyroid: Short correlations (high-frequency "structural noise") give rise to smearing-out and to partial loss in circular contrast. Long-wavelength distortions, however (resembling a *chirp*, *i. e.* pitch gradient throughout the slab), will be found to influence the coupling behaviour, with a pronounced sensitivity of transmission enhancement on the pitch/density gradient.

The helical model of the Gyroid is "disassembled" into its uniaxial subsets, and a separability of the characteristic reflectance behaviour by the helix orientation relative to the incident light is observed.

Contents

1

Introductory Words

Carl Spitzweg: „Der Schmetterlingsjäger“ (1840)

1.1. Structural colour and minimal surfaces—From Life's biotechnology laboratory

Within the manifold phenomena of *physics by geometry*, minimal surfaces (surfaces of minimal area fulfilling given boundary conditions), are one of the topics astonishing the professional world with their persistent recurrence. Their apparent intrication contradicts with their obvious ubiquity, *e. g.*, in various functions for all kinds of organisms. It was only recently that the "double Diamond" membrane, known from plants' ethioplasts, proved "non-photonic", when viewed on the biological scales of length and dielectric contrast [Dec14]—but is nonetheless biology's structure of choice. The envelope of the *stratum corneum* skin layer fibres forms a "Gyroid" surface [ER14]. So it is, present even on atomic scales—arguing for nature's *parsimony* in resolving complex geometric problems—it is found to describe an exotic high-pressure allotrope of elementary nitrogen [Ere+04], and beyond.

The wing scales of various butterflies exhibit structural colouration [GR76; MS08]. As a such, the greenish wings of *Callophrys rubi* with their microscopic[1]/meta[2] structure discovered to be a single Gyroid [Sar+10; Sch+11; MTC11; MTC13] (see sec. 3.2) will play the pivotal role in this thesis.

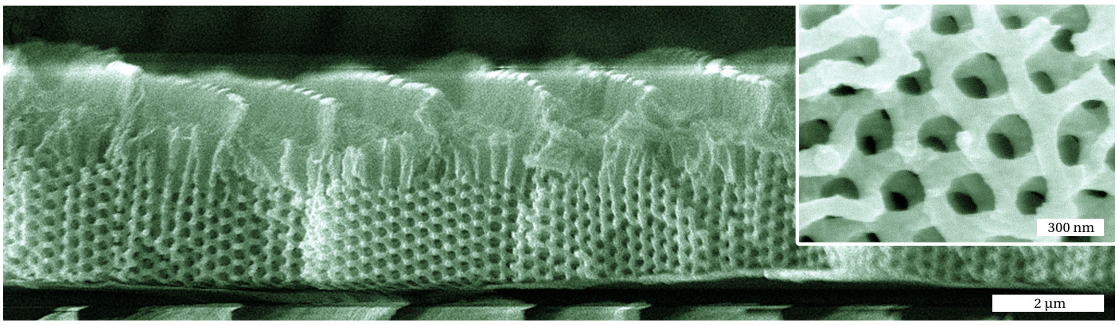

Figure 1.1.: Scanning electron micrograph of *C. rubi* butterfly wing scale surface. The bulk of the depicted cross-section (inset: detailed view) consists of a structure-photonic polycrystalline single Gyroid medium, consisting of chitin. Image source: [Sab+14]

The most striking features rendering the Gyroid in continuous attention, are, beyond (or perhaps on account of) its various occurrences in nature, its friendliness to bottom-up techniques of self-assembly as an "intelligent" structure. Moreover, essential in geometric argumentation, it is bi-continuous (dividing space in two not interconnected parts), it is cubic, *i. e.* with a high intrinsic symmetry, and *handed*, hence occurring in "concurrence with itself".

The deployment of the Gyroid by butterflies to create structural colour has triggered research of its structure-photonic properties, unveiling a lot of remarkable properties [Dol+14].

1.2. "Photonics"—an attempt to clarification

Photonics: This word seems to have become an inevitable terminus in the last few decades' effort of research in the "modern" fields of optics (which once had "monopolised" the entire field of the physics of light).

---

[1] "Microscopic" from the anthropocentric view through a microscope's eyepiece.

[2] The single Gyroid can be regarded as a crystal consisting of dielectric "meta-atoms" shaped to bi-continuously tessellate space.

Originally introduced as a denomination for light-driven analogue to electronics in the field of information technology—hence the name, a portmanteau from *φωτός* (Greek: light) and *electronics*, but rather likely with a connotation towards "photons", the light *quanta*—the name *photonics* was shifted in focus on the "modern" implications quantum nature of light, especially Laser technology, nonlinearity, and quantum optics [Men01]. Due to the stretchability of this term, the introductory chapters of the majority of textbooks avoid a concise definition, and rely instead on an "intuitive" understanding on what photonics means.

Maximum possible scaling dependence The general, recurrent motif is the highlighting of the particulate properties of light (quantum statistics, quantum-mechanical light-matter interaction, etc.) as a separation criterion towards "classical" optics. This implies a intimate dependence on the scales of length, energy, and time characterising the system.

As an example, think of an atom, whose characteristic energy scale (essentially the RYDBERG energy) determine the light frequencies of atomic light emission and absorption. Its energy levels and spatial extent are the very consequences of its quantum nature (classical electrodynamics is not, due to its scale-freeness, *i. e.* ignorance against atomic details of the electromagnetic interaction, *cf.* sec. 2.1.6).

1.2.1. The "photonic" "crystal" (PhC)

The term *photonic crystal* has been coined by Yablonovitch, Gmitter, and Leung [YGL91] with their report on the first full band-gap PhC, somewhat in between the seminal publications of John [Joh87] and Yablonovitch [Yab87], and the textbook of Joannopoulos, Meade, and Winn [JMW95], to describe a periodic structure impeding (or, more generally, manipulating) the propagation of electromagnetic radiation. In all cases, the light–matter interaction is not driven by matching the *energy* scale, but the *length* scales of light and the crystal.[3] So, using the word component "photonics" (to describe some light–matter interaction having to be distinguished from "classical" optics) within the term "photonic crystal" ("[light] physics governed by geometry") is, at best, an un-instructive misnomer.[4] Besides geometrical optics (all relevant lengths $\gg \lambda$), PhC are on the "least photonic" (photon-as-particle) scale structures you can think of.

At least, photonic crystals integrate seamlessly into "core photonics" by usage of their beneficial properties in providing environments for "photonic devices" like Lasers, non-linear materials, or in information transport [Joa+08; Yab87; Men01; Oba11].

1.2.2. The structure-photonic length scale

The "photonic crystal" deals with light–matter interaction phenomena not covered by "classical" photonics: precise knowledge of quantum-mechanical details of both matter and the radiation field is neither exactly known nor relevant; the interplay of the arrangement of continuous (coarse-grained to hide atomic details) bodies in space (called *geometry* further on) and the spatial variation of the electromagnetic field is the sufficient and appropriate scope of view.

This is the case when the length scales of the geometry are not too small to just get averaged by light, but not too large to be covered by classical geometrical optics. Seeking the limiting cases may be part of the comprehensive study of particular systems, *cf.* below in sec. 2.3.

---

[3] Note, that for physically relevant systems staying below the Vacuum-UV frequency limit, vacuum wavelengths are, typical, orders of magnitude larger than interatomic distances within condensed matter.

[4] Note that photonic crystals exploit the wave properties of light rather than its constitution of photons (!).

"Buzzing" and "Un-Buzzing" The terms "photonics" and "photonic crystal" are in good company with a plethora of ambiguous, context- and scale-dependent terminology, of which arbitrary compound words of *micro*, *nano*, *sub-microscopic* (anthropocentric view on length scales), or *meta* (see also sec. 2.3.5) may serve just as a non-representative selection. The benefit of preferring self-reference over self-explanatory for the respective professional fields is certainly dubious.

Structure-photonic materials/media When you want to address PhC behaviour, but want to avoid the ambiguous word "photonic", and just as well the notion of "crystal" (for greater generality towards structures without [more or less strict] translational symmetry), you run into an apparent nomenclature shortage.

Physics of light was traditionally called "optics", but you have to exclude quantum and (macroscopic) geometrical optics. But "physics of light within geometries of the light's length scales" or "dealing with electromagnetic interaction of media structured within the *scale invariant regime* (*cf.* sec. 2.1.6)" appear too bulky. As literature and reader get accustomed to misnomers, sticking to has its advantages. So we will, as a compromise, refer to (dielectric) structures within the "photonic" length scale as "Structure-photonic materials (or media)", and will (not consistently, by recognition reasons) abbreviate this terminus by "PhC".

1.3. Is Light a good probe for geometric chirality?

Figure 1.2.: Nail scissors for right and left hands: enantiomers of obviously opposite "handedness".

When connecting the geometric chirality to the chiral properties of light (most prominent in presence as with circular polarisation), two contexts of handedness meet. We will discuss how much (or how little) we can say about the complex interplay of those, complicated by the subtle non-localities of light–geometry interaction.

The [geometric] notion of handedness Chirality of a geometric object is commonly defined as the "lack of mirror/inversion symmetry", being dependent on the number of spatial dimensions available for generalised off-plane rotations [Arn97; Ama09].

Equivalently, an object is called chiral, when it cannot be congruently superposed with its mirror-image by applying translation or proper rotations alone. Not only the obvious standard example *human hand*, but also the respectively appropriate scissors (fig. 1.2) exhibit chirality.

The handedness of light *(This paragraph is an anticipation to sec. 2.2, and will be soundly introduced there.)* Electromagnetic plane waves in free space can be described within the *circular* basis, in which the field vectors **E** and **H** behave helical in their spatial structure along the propagation direction. It is therefore suggestive to study the interrelation of the *geometric* chirality of a given structure with the *optical* chirality of the light. This has been subject to several investigations already [LC05; Sab+11; Sab+13; Was13], and will also be the main scope of this work.[5]

The paramount question: Is light an appropriate probe for geometric handedness?

Depending on the question we ask, it is. Paralleling the decay of (handed) geometric distinctness from distortion with electromagnetic observations may be inappropriate for a fundamental understanding of the interrelation of chirality and distortion—but it is perfectly appropriate from the *photonic* point of view, *i. e.* when you look on the implications for light response as a “measure for non-crystallinity”.

We have to bear in mind, that we test the properties of *light* as well as those of the geometry when interrelating the two.

So this thesis will ask for the implications of the interrelation of geometric and light chirality, will search for approaches to quantification, and illuminate its results in the light of these intrications.

---

[5] Note, however, that the “smoothness” prerequisites (as implied from field differentiability) cause subtle implications in how “stiff” the electromagnetic fields follow features of geometric chirality, *i. e.* how accurate they are able to trace geometry.

2

Physics of Light and Geometry

Pink Floyd: The Dark Side of the Moon (LP back cover, 1973)

2.1. Maxwell's Equations and Light in Matter

2.1.1. The Maxwell Equations

Classical electrodynamics usually start with implying [Jac98] or postulating [Jon89] the Maxwell equations (2.3)–(2.6) as the governing equations for the electric and magnetic fields.[6] They express, in terms of differential equations, the spatial and temporal interrelations of the *electric* field $\tilde{\mathbf{E}}$, and the *magnetic* field $\tilde{\mathbf{B}} = \tilde{\mathbf{H}}$ (In the non-magnetic case assumed here, this relation becomes trivial, which is not the case in a more general case). By choice[7] of the constitutional relation

$$\tilde{\mathbf{D}} = \varepsilon \tilde{\mathbf{E}} \tag{2.1}$$

the permittivity[8] is introduced to relate the electric field with the dielectric material response within the *electric displacement field* $\tilde{\mathbf{D}}$. The *geometry* becomes determined by the "material function" $\varepsilon(\mathbf{r})$ (defined by spatial dependence of ε) as the "input quantity" for these electromagnetic studies.

The action of the fields in terms of Newtonian mechanics is expressed by the Lorentz force

$$\dot{\mathbf{p}} = q\left(\tilde{\mathbf{E}} + \frac{1}{c_0}\mathbf{v} \times \tilde{\mathbf{B}}\right) \tag{2.2}$$

of impulse change (force $\dot{\mathbf{p}}$) on a particle of charge q moving with speed $\mathbf{v}$.

The Maxwell equation divide into two divergence equations (connecting fields with source densities), and two curl equations (linking field curls with temporal variations). The common distinction into homogeneous (eqs. (2.3) and (2.6)) and inhomogeneous (eqs. (2.4) and (2.5)) equations only arises from the "asymmetric" existence of *electric* charges ϱ and currents $\tilde{\mathbf{j}}$ (and not their magnetic counterparts). This is irrelevant in the absence of free electric charges, *i. e.* $\varrho = 0$, $\tilde{\mathbf{j}} = 0$.

The equations read as [Jac98]: Gauss laws:

$$\nabla \cdot \tilde{\mathbf{D}} = \varrho \tag{2.3}$$

$$\nabla \cdot \tilde{\mathbf{B}} = 0 \tag{2.4}$$

and curl equations:

$$c_0 \nabla \times \tilde{\mathbf{E}} + \partial_t \tilde{\mathbf{B}} = 0 \tag{2.5}$$

$$c_0 \nabla \times \tilde{\mathbf{H}} - \partial_t \tilde{\mathbf{D}} = \tilde{\mathbf{j}} \quad . \tag{2.6}$$

One major implication of the Maxwell equations are their inherent charge conservation, known as the *continuity equation*, which reads in its differential formulation[9]:

$$\partial_t \varrho + c_0 \nabla \cdot \tilde{\mathbf{j}} = 0 \quad , \tag{2.7}$$

and shows the equivalence of divergence equations with continuity/flux conservation

---

[6] Due to focusing on the scope of this work, we skip the introduction of the Maxwell equations in all-vacuum space, and magnetic materials ($\mu \equiv 1$). Moreover, the charge density and current, $\varrho = 0$ and $\mathbf{j} = 0$, will be zero, and are only expressed within eqs. (2.3) and (2.6) for abstract argumentations, rather than existing in the real simulation (except for the light sources, of course).

[7] Several field parametrisations exist to conceal microscopic details of non-vacuum electromagnetic field interactions into response fields, the one adopted here is to use $\tilde{\mathbf{D}}$ and $\tilde{\mathbf{H}}$ fields, avoiding explicit dealing with electric polarisation and magnetisation.

[8] In general, the interconnection of the electric and displacement field will have to be described by a *tensorial* ε, translating anisotropic microscopic polarisation into the constitutional relation. See sec. 2.2.2.

[9] This is simply derived from $\partial_t\,(2.3) + \nabla \cdot (2.6) = 0$.

The choice of units and interconversions is performed to emphasise the *natural* interrelations between the quantities (*e. g.*, for the electric and magnetic fields to have the same units). Permittivites are always relative: the assistant constants ε_0 and μ_0 familiar from the SI electrodynamics are set equal to unity.

Even though the vacuum speed of light c_0 can be chosen to unity in practice (leading to a *non-dimensionalised* "unit" system, the units of time and space becoming equivalent), c_0 is, by convention, explicitly written into the formulae to distinguish spatial from temporal coordinates. See sec. 2.1.6 for the physical motivation of natural units.

Complex field notation

The quantities $\tilde{\mathbf{E}}$, etc. have been introduced as the fields of *physical* relevance, *e. g.* for the Lorentz force (2.2). However, for most calculations it proves sensible to introduce a *complex field notation* [Jac98], which simplifies calculations of harmonic fields, and assists in elegant Fourier formulations of many problems. The complex-valued field $\mathbf{X}$ replaces the physical field $\tilde{\mathbf{X}}$ in calculations, and every time a physical quantity is computed, its real part is evaluated: $\tilde{\mathbf{X}} = \mathrm{Re}(\mathbf{X})$.

With this, one can easily apply the *harmonic* ansatz, *i. e.* a temporal field propagation in terms of a complex time dependence $\mathbf{X}(t) = \mathbf{X}\exp(-\imath\omega t)$, when the problem does not exhibit explicit time dependence. It is *monochromatic* in the sense of enabling *frequency-wise* treatment, and enables elegant formulations by temporal Fourier transformation ($\partial_t \equiv -\imath\omega$).

When real observables which are quadratic in the fields are computed:

$$\begin{aligned} \mathbf{X}(t) =& \mathbf{X}\exp(-\imath\omega t) \equiv \mathbf{X}\varphi \\ \tilde{\mathbf{A}}\cdot\tilde{\mathbf{B}} = \mathrm{Re}\left(\mathbf{A}(t)\right)\cdot\mathrm{Re}\left(\mathbf{B}(t)\right) =& \frac{1}{4}\left((\mathbf{A}\varphi + \mathbf{A}^*\varphi^*)\cdot(\mathbf{B}\varphi + \mathbf{B}^*\varphi^*)\right) = \\ =& \frac{1}{2}\,\mathrm{Re}(\mathbf{A}^*\cdot\mathbf{B}) + \frac{1}{2}\,\mathrm{Re}(\mathbf{A}\cdot\mathbf{B}^*\varphi^2) \quad , \end{aligned} \tag{2.8}$$

and subsequently time-averaged (observation times commensurable or long with respect to $2\pi/\omega$, in reminiscence with long-time limits, and feasible experimental measurement times), the second term (oscillating with $\varphi^2 = exp(-2\imath\omega t)$ cancels out due to its time dependence $\propto \cos(2\omega t)$.

Electromagnetic waves

From the Maxwell equations, the electromagnetic *wave equation* can be derived[10]

$$\begin{aligned} c_0^2\nabla\times(\nabla\times\mathbf{E}) + c_0\partial_t\nabla\times\mathbf{B} =& 0 \\ \left(c_0^2\nabla^2 - \varepsilon\partial_t^2\right)\mathbf{E} =& 0 \\ \text{Harmonic:} \qquad \left(c_0^2\nabla^2 + \varepsilon\omega^2\right)\mathbf{E} =& 0 \end{aligned} \tag{2.9}$$

A successful ansatz[11] to find solutions for the spatial dependence $\mathbf{E}(\mathbf{r})$ is a (spatial harmonic) *plane-wave* basis, *i. e.* $\mathbf{E} \propto \exp(i\mathbf{k}\cdot\mathbf{r})$, each mode described by its *wavevector* $\mathbf{k}$.

These solutions of the Maxwell equations prove to describe *transverse plane waves*, and introduce an additional degree of freedom of *polarisation* (direction of $\mathbf{E}$). In vacuum and isotropic media, the modes are degenerate. Further at 2.2.1

---

[10] From $c_0\nabla\times$ (2.5) with (2.6) and (2.3)—remember the absence of charges.

[11] In this introduction, we restrict to plane waves, but other solutions emerging from more intricate mathematics are in existence and of some practical relevance: Think of Gaussian beams modeling beam shape of finite lateral extent, or spherical waves.

The spatial derivative converts to $\nabla \equiv \imath \mathbf{k}$, and the *dispersion relation*

$$\begin{aligned} \left(-c_0^2\mathbf{k}^2 + \varepsilon\omega^2\right)\mathbf{E} = & 0 \qquad \forall \mathbf{E} \\ \omega^2 = & \frac{c_0^2}{\varepsilon}\mathbf{k}^2 \\ \omega = & \frac{c_0}{\sqrt{\varepsilon}}|\mathbf{k}| = \frac{c_0}{n}|\mathbf{k}| \end{aligned} \tag{2.10}$$

evolves naturally from eq. (2.9). By convention, the *refractive index* $n = \sqrt{\varepsilon}$ is introduced as the ratio of the light speed within medium to its value in vacuum.

2.1.2. Energy density and flux

The local energy densities of the electric and magnetic field

$$\begin{aligned} \tilde{w}_{\mathrm{el}} = & \frac{1}{2}\tilde{\mathbf{E}}\cdot\tilde{\mathbf{D}} = \frac{\varepsilon}{2}\tilde{\mathbf{E}}^2 = \frac{1}{2\varepsilon}\tilde{\mathbf{D}}^2 \\ \tilde{w}_{\mathrm{mag}} = & \frac{1}{2}\tilde{\mathbf{H}}\cdot\tilde{\mathbf{B}} = \frac{1}{2}\tilde{\mathbf{H}}^2 \end{aligned} \tag{2.11}$$

(for linear media) are derived in textbook electro-/magnetostatics, and are also proven for time-dependent fields [Jac98]. They consider both the charge/current density self-interaction and the contributions stored in the build-up of the polarisation state within the media.

Energy conservation law in electromagnetics is usually referred to as Poynting's theorem [Jac98]: By considering an electromagnetic field exerting the Lorentz force, eq. (2.2), on a moving probe charge (representing a current density $\tilde{\mathbf{j}}$), and the above expressions for field energies, the continuity equation for field energy reads, in its differential form, as

$$\partial_t\left(w_{\mathrm{el}} + w_{\mathrm{mag}}\right) + c_0\nabla\cdot\tilde{\mathbf{S}} = -\tilde{\mathbf{j}}\cdot\tilde{\mathbf{E}} \quad , \tag{2.12}$$

introducing (by use of the Maxwell equations, and some vector calculus) the Poynting vector

$$\tilde{\mathbf{S}} = \tilde{\mathbf{E}} \times \tilde{\mathbf{H}} \tag{2.13}$$

as the field of *energy flow* carrying energy density. By application of the harmonic ansatz for the fields (see sec. 2.1.1), this becomes $\tilde{\mathbf{S}} = 1/2\,\mathrm{Re}(\mathbf{E}^* \times \mathbf{H})$. The Poynting vector describes energy transport by electromagnetic waves, and is, for plane waves, directed along $\mathbf{k}$. As a such, it is a useful and natural measure of *intensity*, combining the contributions of electric and magnetic fields irrespective of polarisation state, and as a such it is implemented into the software used for the presented simulations [MIT].

2.1.3. Fresnel formulæ: Field matching at interfaces, and reflection

This section describes the *reflection* behaviour of electromagnetic waves at interfaces between media exhibiting *dielectric contrast, i. e.* different ε. From integrating the Maxwell equations surrounding a finite area of the surface, which is described by its normal vector $\mathbf{n}$, two kinds of field continuity conditions can be derived generically: $\tilde{\mathbf{D}}\cdot\mathbf{n} = 0 = \tilde{\mathbf{B}}\cdot\mathbf{n}$ (normal components stay continuous), and $\tilde{\mathbf{E}} \times \mathbf{n} = 0 = \tilde{\mathbf{H}} \times \mathbf{n}$ (tangential components continuous).

For electromagnetic waves, the situation at a material interface is a reflection problem, involving an incoming, a reflected and a transmitted wave. Applying complex notation, the problem is formulated as matching their amplitudes (complex, including phase factors $\mathbf{k}\cdot\mathbf{r}$ at the boundary, which is located at $\mathbf{r}$) for all times. This leads to the famous FRESNEL formulae [Jac98], quantitatively describing reflection and transmission dependent on incident angle $\arccos(\mathbf{n}\cdot\mathbf{k}/k)$ and the dielectric contrast ε (usually expressed in terms of the two refractive indices n_1 and $n_2 = n_1\sqrt{\varepsilon}$ of the involved media). The treatment requires the following choice of the plane-wave basis: linear polarisations, with polarisation vectors tangential to the surface either of the electric field (TE) or the magnetic field (TM). Only at normal incidence, they are degenerate, giving rise to a particularly simple formula to compute the absolute value of reflection:

$$|r| = \frac{n_1 - n_2}{n_1 + n_2} = \frac{\sqrt{\varepsilon} - 1}{\sqrt{\varepsilon} + 1} \tag{2.14}$$

2.1.4. Thin-film interference: a slab of finite thickness

Computing the transmittance of a "thin film"[12] is a standard exercise in any optics textbook [Men01]. It will be presented here, as its effect, the FABRY-PÉROT interference, will be a prominent part of any slab-like transmission or reflectance measurement, both in simulations and experimentally.

Given a material of dielectric contrast ε to its exterior (vacuum), constituting a *slab* of the thickness L, with perfectly plane faces and infinite lateral extent: $\varepsilon(\mathbf{r}) = 1 + (\varepsilon - 1)\Theta(L/2 - |z|)$. The slab be irradiated in normal direction with a plane wave of incoming electromagnetic radiation. This light wave is described by the wavevector $\mathbf{k}_\mathrm{i} = k_\mathrm{i}\mathbf{e}_z$, and $\mathbf{E}_0$, the incident electric wavevector at the origin: As long as the slab is disregarded, its electric field is given by $\mathbf{E}(\mathbf{r}) = \mathbf{E}_0 \exp(\imath(\mathbf{k}_\mathrm{i}\cdot\mathbf{r} - \omega t))$, and the (electric) field intensity by $I_\mathrm{i} = |\mathbf{E}|^2 = |\mathbf{E}_0|^2 = E_0^2$.

Each time the light crosses the interface between the medium and vacuum, observing the field matching rules 2.1.3 will cause part of the amplitude to be reflected:

$$\begin{aligned} \text{Transmission:} \quad & |E_\mathrm{f}^\mathrm{t}| = |t|\cdot|E_\mathrm{i}| \\ \text{Reflection:} \quad & |E_\mathrm{f}^\mathrm{r}| = |r|\cdot|E_\mathrm{i}| \\ \text{Amplitude conservation per interface:} \quad & t^2 + r^2 = 1 \\ \text{Global flux conservation:} \quad & T + R = 1 \end{aligned} \tag{2.15}$$

with the reflection and transmission amplitudes r and t (as introduced in the previous section) being a property of the single interface, and the total transmitted/reflected intensities, denoted by capital R and T (which are, in contrast to r and t, properties of the whole arrangement).

The fraction of intensity immediately transmitted (through both the front and back interface) is thus $I_\mathrm{i}|t|^2$, but is accompanied by infinite multiple internal reflections, giving rise to interference due to their difference in phase.

While passing through the material for a length ℓ, a wave accumulates a phase angle of $\Gamma = k\ell = k_\mathrm{i}\sqrt{\varepsilon}\ell$, and at the back face an additional phase jump of π. For every two additional internal reflections (one at the back face, one at the front face), the intensity is each time diminished to the remaining $|r|^2$ (remainder from two transmissions) and the phase advances by $\Gamma = 2kL\sqrt{\varepsilon} + 2\pi$, giving for the total

---

[12] This *relative* definition of thickness has to be understood in the sense of *thin enough to not be disturbed by the finite coherence of the incident light, i. e.* in the validity regime of idealised monochromatic plane waves. There is no length scale.

series:

$$\begin{aligned} \frac{|E^{\mathrm{t}}|}{|E_{\mathrm{i}}|} &= |t|^2 \sum_{m=0}^{\infty} \left(|r|^2 e^{\imath\Gamma}\right)^m = |t|^2 \frac{1}{1-|r|^2 e^{\imath\Gamma}} \\ \left[1-\frac{I^r}{I_{\mathrm{i}}} = 1-R=\right] T = \frac{I^{\mathrm{t}}}{I_{\mathrm{i}}} &= \frac{|t|^4}{|1-|r|^2 e^{\imath\Gamma}|^2} = \frac{|t|^4}{|1-|r|^2 e^{\imath\Gamma}|^2} = \\ &= \frac{(1-|r|^2)^2}{1-2|r|^2\cos\Gamma+|r|^4} = \frac{1}{1+4|r|^2(1-|r|^2)^{-2}\sin^2\left(\frac{\Gamma}{2}\right)} \end{aligned} \tag{2.16}$$

The latter result is known as the Airy formula [Air33]. It describes the interference-modified transmittance (or, complementary, reflectance) of a material interface "knowing" about another interface not too distant away, dependent of wavelength and material thickness $L\sqrt{\varepsilon}/\lambda_0 = \Gamma \bmod 2\pi$.

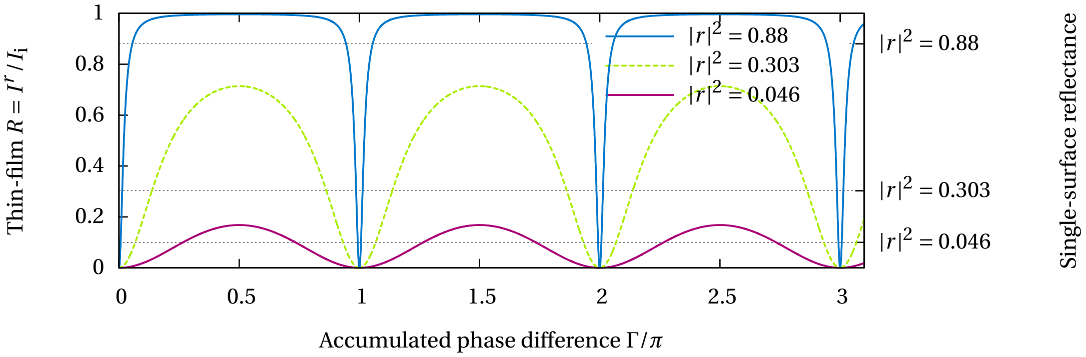

Figure 2.1.: Reflectance, at normal incidence, of a homogeneous lossless-dielectric slab of surface reflectance $|r|^2$ as a function of phase accumulation $\Gamma = \sqrt{\varepsilon}L/\lambda_0$. Selected single-surface reflectances correspond to dielectric contrasts of $\varepsilon = 2.4$ ($|r|^2 = 0.046$), $\varepsilon = 11.9$ ($|r|^2 = 0.303$), and $\varepsilon = 10^3$ ($|r|^2 = 0.88$).

It is depicted in figure 2.1 and shows, irrespective of how high the actual reflectance is, full transmission on Γ being an integer multiple of π, as a consequence of destructive interference of reflected beams. On half-integer Γ, however, reflectance reaches remarkably higher values than anticipated from the single-surface case, reaching a maximum value of $\overline{R}$, being dependent on the dielectric contrast as

$$\begin{aligned} R \leq \overline{R} &= 1 - \frac{1}{1-4|r|^2(1-|r|^2)^{-2}} = \left(\frac{\varepsilon-1}{\varepsilon+1}\right)^2 \\ \varepsilon(\overline{R}) &= \frac{1+\sqrt{\overline{R}}}{1-\sqrt{\overline{R}}} \quad . \end{aligned} \tag{2.17}$$

The idea to utilise Fabry-Pérot extrema heights and frequency locations to extract some kind of "effective refractive index" from slab reflectance data might be some contribution to a heuristic effective medium data acquisition. But once subject to distortion on a scale which is not tiny compared to the wavelength (see chapter 5), the rigorous assumption of predictable and uniform phase accumulation irrespective of the position within the structured medium becomes questionable, blurring effective slab thickness. In effect, with finite distortion, the minima get less pronounced, impeding the benefit from explicitly exploiting Fabry-Pérot features to gather structural information.

2.1.5. Absorption

A convenient way of representing light absorption within the given electromagnetic framework is to allow the permittivity ε to be *complex*: Consider a slab-like geometry of an absorbing medium at $0 < z < L$, in the approximation of attenuation lengths large compared to the wavelengths ($\alpha\lambda_0 \ll 1$, hence $\mathrm{Im}(\varepsilon) \ll \mathrm{Re}(\varepsilon)$, see below). It becomes obvious that a complex wavenumber $\underline{k} = k + \imath\alpha/2$, describing an exponential decay of waves incident on the absorbing medium, is connected to $\mathrm{Im}(\varepsilon)$ by:

$$\begin{aligned}
\frac{|\mathbf{E}(z)|}{|\mathbf{E}(0)|} &= \left|e^{\imath\underline{k}z}\right| = \left|e^{\imath(k+\imath\alpha/2)z}\right| = e^{-\alpha z/2} \\
\underline{k}^2 &= k^2 + \frac{\alpha^2}{4} + \imath\alpha k = \frac{w^2}{c_0^2}\varepsilon \qquad (2.10) \\
\mathrm{Re}(\varepsilon) &= \frac{c_0^2}{\omega^2}\left(k^2 + \frac{\alpha^2}{4}\right) \cong \frac{c_0^2}{\omega}k^2 + \mathcal{O}(\alpha^2) \\
\mathrm{Im}(\varepsilon) &= \frac{c_0^2}{\omega^2}\alpha k = \frac{c_0}{\omega}\alpha\sqrt{\mathrm{Re}(\varepsilon) - \frac{c_0^2\alpha^2}{4\omega^2}} \cong \frac{c_0}{\omega}\alpha\sqrt{\mathrm{Re}(\varepsilon)} + \mathcal{O}(\alpha^3)
\end{aligned} \tag{2.18}$$

The well-known phenomenological Beer-Lambert absorbance relation, connecting the final intensity I_f (normalised to incoming intensity I_i) introduces the *attenuation constant* α (inverse of the $1/e$ attenuation length)

$$\begin{aligned}
\frac{|\mathbf{E}(L)|^2}{|\mathbf{E}(0)|^2} = \frac{I_\mathrm{f}}{I_\mathrm{i}} &= e^{-\alpha L} \\
I(x)/I_\mathrm{i} &= e^{-\alpha x} \quad ,
\end{aligned} \tag{2.19}$$

which can interrelate the imaginary part of the permittivity with transmission flux:

$$\begin{aligned}
I_\mathrm{f} &= I_\mathrm{i} - I_\mathrm{absorb} \cong I_\mathrm{trans} \qquad \text{as long as } I_\mathrm{refl} \ll I_\mathrm{trans} \\
\alpha &= \frac{1}{L}\ln\left(\frac{I_\mathrm{i}}{I_\mathrm{f}}\right) = \frac{1}{L}\ln\left(\frac{I_\mathrm{i}}{I_\mathrm{trans}}\right) \\
\frac{\omega L}{c_0}\frac{\mathrm{Im}(\varepsilon)}{\sqrt{\mathrm{Re}(\varepsilon)}} &= \ln\left(\frac{I_\mathrm{i}}{I_\mathrm{trans}}\right)
\end{aligned} \tag{2.20}$$

2.1.6. Reduced variables and natural units

The Maxwell equations (and their solutions) exhibit a (trivial, from the mathematics side) invariance under scaling frequencies by α, together with

- either scaling lengths by α^{-1},
- or permittivities[13] by α^{-2}, *i. e.* refractive index by α^{-1}

This is a consequence of the absence of an explicit scale within classical electrodynamics[14] [Joa+08], and enables to reproduce any experiment on any length scale, as long as the scaling rules are observed (and the continuum assumption is justified). This has been often exploited, *e. g.* by [VKH08; PV12].

---

[13] It can even be shown that any coordinate transformation is equivalent to (can be encoded into) a transformation of $\varepsilon(\mathbf{r})$ and $\mu(\mathbf{r})$ [WP96].

[14] The beauty of the classical theory with respect to a numerical treatment is its *exactness* in a sense arising from the same fact: no questionable assumptions and simplifications are needed to conduct simulations, opposed to, *e. g.* ab-initio quantum-mechanical calculations like DFT [Oba11].

As a consequence, the characteristic lengths introduced by the geometry itself are the only relevant scales, so they can easily been reduced to unity, to obtain *natural units* for all quantities.

Be $a$such a characteristic length of a structure (for the structures derived from cubic crystals, this is, by convention, the edge length of the conventional cubic unit cell), then space coordinates can be given relative to a, and so can time (via the speed of light: c_0 in vacuum; phase velocity within the medium: $c = c_0/\sqrt{\varepsilon}$), and especially, frequency:

$$\Omega = \frac{\omega a}{2\pi c_0} = \frac{a}{\lambda_0} \tag{2.21}$$

This dimensionless *natural* frequency (in contrast to the actual frequency ω in units of reciprocal time) is closely linked to the (reduced) vacuum wavelength λ_0/a of the corresponding light. Once an explicit length scale a (in real physical units) has been introduced, the frequency might be translated to a photon quantum energy via the conversion $\hbar\omega = \Omega \cdot hc_0/a$. When a is in the order of the visible light wavelengths, a Ω near unity represents quantum energies in the visible range; then a colour bar can be drawn aside a frequency axis, *cf.* B.3.

The introduction of an explicit scale (meaning the breakdown of validity to an universal natural unit) gets necessary, once interaction is not solely determined by geometry, and the quantum nature of light (and matter) plays a role, *e. g.*:

- Resonances of atomic/meta-atomic systems (absorbance (dyes!))
- Material non-linearities (Higher-harmonic creation)
- Collective excitations (most notably plasmons)
- Non-classical light-matter interactions (Laser gain medium)

2.2. Chirality and Light in homogeneous media

2.2.1. The Polarisation state

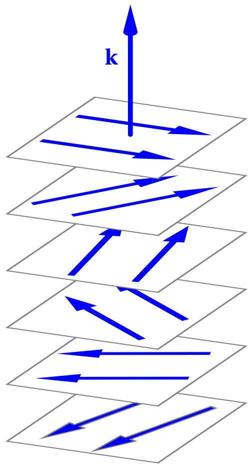

Figure 2.2.: Circular polarised plane wave: spatial $\tilde{\mathbf{E}}$ (or $\tilde{\mathbf{H}}$) field pattern at an instant in time.

Electromagnetic waves are described by vector fields, so their amplitude has to be described by a vectorial quantity. For plane waves, the MAXWELL equations only imply the condition of *transverse* waves, *i. e.* $\tilde{\mathbf{E}} \cdot \mathbf{k} = 0 = \tilde{\mathbf{B}} \cdot \mathbf{k}$ (and $\tilde{\mathbf{E}} \cdot \tilde{\mathbf{B}} = 0$) at all places in space. The dispersion relation (2.10) cannot determine the particular spatial structure of the waves—rather this proves to be a degree of freedom of the system: For any wavevector $\mathbf{k}$, two orthogonal polarisation vectors can be found to describe a plane wave.

The most familiar (and most readily imaginable) choice for basis functions is *linear polarisation*, *i. e.* both the $\tilde{\mathbf{E}}$ and $\tilde{\mathbf{B}}$ field *oscillating* (in space and time) in planes tangential to $\mathbf{k}$.

However, the oscillations are not restricted to be in the amplitude's absolute value alone, but can also exhibit, in general, periodic change in the *direction* (elliptic polarisation), or solely so (circular polarisation,[15] CP): The field vectors are of the same length at all points in

---

[15] Note that, conversely, linear polarised light itself can be interpreted as a superposition of LCP and RCP light of the same amplitude, and its node surfaces (propagating along $\mathbf{k}$ with time) can be understood as the nodes of azimuthally standing waves.

space, and exhibit spatial dependence of direction according to their wavelength: see fig. 2.2.[16]

Description of the polarisation state

The complex field notation (sec. 2.1.1) provides an elegant way to describe the basis functions of light. The choice of one (lateral) direction x perpendicular[17] to $\mathbf{k}$ determines the linear polarisation basis functions (up to a uniform phase shift, which can always be absorbed in choosing the temporal zero point) of the lateral electric[18] field $\mathbf{E}_\parallel = (E_x, E_y)^\mathrm{T}$ as

$$\begin{aligned} &x\text{-polarised} \qquad \mathbf{E}_\parallel = E\begin{pmatrix}1\\0\end{pmatrix} \\ &y\text{-polarised} \qquad \mathbf{E}_\parallel = E\begin{pmatrix}0\\1\end{pmatrix} \quad , \end{aligned} \tag{2.22}$$

The circular basis encodes its spatial phase offset between x and y into a complex spatial amplitude:

$$\begin{aligned} &\text{LCP} \qquad \mathbf{E}_\parallel = \frac{E}{\sqrt{2}}\begin{pmatrix}1\\-\imath\end{pmatrix} \\ &\text{RCP} \qquad \mathbf{E}_\parallel = \frac{E}{\sqrt{2}}\begin{pmatrix}1\\\imath\end{pmatrix} \end{aligned} \tag{2.23}$$

This notation equals, once normalised to the absolute field amplitude E, the JONES vector known from classical optics [Men01].

The rotation sense convention Due to the existence of contradicting conventions regarding to what is LCP and what is RCP, we will stick to the "time-frozen" definition from [LC05]: This light shall be called right-handed CP, whose tips of $\tilde{\mathbf{E}}$ vectors around some axis directing in $\mathbf{k}$ direction, forms a RH helix.

Later on, once the handedness of a given geometry got assigned (be it by convention or analysis, but definitively, see sec. 3.2.2 for the Gyroid's handedness) we can re-label the CP states *relatively* according to the geometric handedness: as "in the same rotation sense": ↺↺, or in the opposite sense: ↻↺.

This way, the complete mirror inversion of both the structure and the rotation sense of the light won't change anything to both physics (which is obvious), and nomenclature (which underlines a gain in universality, referring to, in some sense, expressing geometric and light chirality in the *natural unit* of the relative rotational sense).

2.2.2. Chiral response from geometry

Homogeneous media: intrinsic chirality

In the context of linear polarisation, degeneracy between basis modes is destroyed when "cross-talk" of the different electric field components is allowed within the constitutional polarisation equation (2.1)

---

[16] It turns out that CP is in fact the fundamental base state of light, reflecting the intrinsic "rotatory sense" (spin/helicity) of the photons.

[17] You may consider, w. l. o. g., $\mathbf{k}$ poẏnting in Cartesian $+z$ direction.

[18] By convention, the polarisation is formulated for the electric field. This uniquely determines the according magnetic field components.

(called *birefringence*: dependence of refractive index from the polarisation plane). It is conveniently expressed by a tensorial dielectric permittivity ε.

Conceptually related is "bi-anisotropy" (see, *e. g.*, [Arn97; SS15]), allowing, in addition, the displacement field to be also dependent from the magnetic field components.

The positioning of these relations within electrodynamics shows up its meaning as an *intrinsic* property of the respective material. In contrast to geometry-inherited handedness, it may thus be called *intrinsic chirality*, caused microscopically (lengths scales small compared to the wavelengths) by objects/(meta)atoms being able to interconnect electric and magnetic effects, *e. g.* metallic wire helices [JMP79; EJ88], or (based on experimental evidence) sugar solutions.

Once translated to the language of phenomenology and experiments, the intrinsic chirality causes effects like *optical rotation* (either CP sense experiencing a different phase accumulation during passing the material, causing a rotation of the polarisation ellipse).

Chiral objects and CP light

When (as in the case of dielectric structures of length scales in the order of the light wavelengths), a microscopically averaging view becomes inappropriate, and other ways of dealing with system response to light chirality must be found.[19] The route of some spatial density of objects leads (due to the subtle non-locality arising from the Maxwell equations) naturally to the intrication of the "basis" (single objects) and "lattice" (site distribution) dependencies of any obtained result. In any case, the lateral (perpendicular to $\mathbf{k}$ in free space, and appropriately chosen within vacuum) continuity of CP light will be broken down by the presence of objects (at most to the discrete translation rules of a crystal).

However, there have been some explicit studies of the structure-photonic functionalisation of helices. Referring to the success of PhC in which helices serve "only" as bandgap-functional elements [YGL91; Joa+08], Chutinan and Noda [CN98] investigated dielectric PhC made with helices as basis elements—disregarding possible implications due to their handedness. Uniaxial and cubic arrays of helices have been subject to several studies regarding CP response [TJ01; LC05; Fre+10; Thi+10; Was13]; however, without conclusive links from circular-dichroic effects to local geometry or reverse.

A crucial issue in inhomogeneous media is the loss of the notion of circular polarisation (as a basis state of light), replaced by Bloch modes (see sec. 3.1), which becomes even worse in non-periodic media, when the Bloch theorem does no longer assist by its elegant constructive rules for modes.

2.3. Structure-Photonic Crystals—theory and examples

This section describes the implications of a system consisting of periodically arranged matter (a *crystal*), on its way to support the propagation of electromagnetic waves. It will focus on the dielectric permittivity $\varepsilon(\mathbf{r})$ as an spatially inhomogeneous material function.

2.3.1. The Bloch Theorem and the Band Structure

Arising from the question how the periodicity of a crystal lattice reflects in the structure of wavefunctions, Bloch [Blo29] introduced his famous theorem, nowadays named after him—although it has thorougly

---

[19] Even the charming route of "assembling" structures from single objects, probed as a single, is infeasible.Alone the idea to test a localised, finite object with a plane wave (with its infinite spatial extent in lateral direction), is ill-defined, let alone the "superposition" of single-particle behaviour. By introducing finite transversal and longitudinal coherence lengths, things might become a little better, but the "multi-body" problem within the coherence volume stays.

been pioneered earlier, *e. g.* by Floquet [Flo83]. It states that the eigenstates ψ of an operator with a potential exhibiting translational symmetry with respect to a crystal lattice $\{\mathbf{R}\}$, can be chosen as

$$\psi_{\mathbf{k}}(\mathbf{r}) = e^{\imath \mathbf{k}\cdot\mathbf{r}} u_{\mathbf{k}}(\mathbf{r}) \tag{2.24}$$

to separate into a *lattice periodic* function $u_{\mathbf{k}}(\mathbf{r}) = u_{\mathbf{k}}(\mathbf{r}+\mathbf{R})\ \forall \mathbf{R}$, and a *phase factor*, introducing the *crystal wavevector* $\mathbf{k}$ to characterise the mode [AM76]. Any function of this form is infinitely extent over the whole (infinite) crystal, and its absolute value is lattice-periodic.

Indexing wavevectors: the Brillouin zone

The space holding the crystal wavevectors is called the *reciprocal space*. It exhibits some crystalline structure by the *reciprocal lattice* $\{\mathbf{G}\}$, the sites at which the phase factor in eq. (2.24) equals unity irrespective of $\mathbf{r}$, thus being the Fourier transform of the real-space crystal lattice.

The Bloch theorem now readily shows that, for any $\mathbf{k}$ of the crystal wavevectors a $\mathbf{G}$ from the set of reciprocal lattice vectors can be found to let the vector $\mathbf{k}-\mathbf{G}$ be closer to the reciprocal lattice origin Γ than to any other point, in effect reducing the effective volume to be considered to the Voronoi cell[20] of the Γ point, which is commonly called the (first) Brillouin zone (BZ).

When mapping infinitely many Wigner–Seitz cells of the reciprocal space on one single, the arising ambiguity is resolved by introducing a *band index* n, storing the “umklapp” information (length and direction) of the $\mathbf{G}$ lattice vector as a second index characterising the Bloch waves.

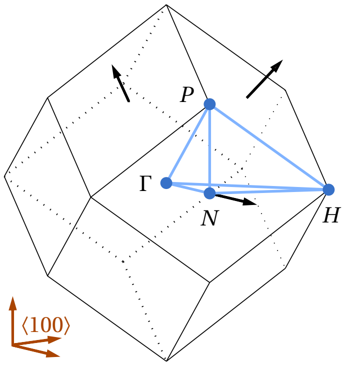

Figure 2.3.: The Brillouin zone of the BCC lattice, and its high-symmetry points. Derived from [SC10]. Black arrows: primitive reciprocal lattice vectors (not to scale).

As the BCC crystal lattice will play a central role within this thesis, its BZ is depicted in figure 2.3. The high-symmetry points (low Miller indexing) on the BZ surface are named by convention, in order to identify the translational symmetry of the modes between real-space and *band diagrams*: Plots of the dispersion relation $\Omega(\mathbf{k})$, *i. e.* the eigenfrequencies of the modes resulting from evaluating of the constitutional wave equation (which deviates from eq. (2.10) due to the influence of the periodic potential) are usually parametrised by the way along high-symmetry directions (edges of the distorted tetrahedron in the image).

Evanescent and propagating modes

The Bloch theorem claims exactness only for infinitely extent “propagating” modes, spanning the whole crystal with constant amplitude. At an interface, *e. g.* a surface towards a homogeneous medium like vacuum, the eigenmodes of the two media have to couple, to enable finite transmission. By the violation of translational symmetry in the region around the interface, the Bloch theorem (intended to describe behaviour in the undisturbed bulk crystal) or the free-space solutions (plane waves) are not expected to provide accurate solutions without modification.

In general, the infinite propagation is not guaranteed (see below) for all waves crossing the interface. This gives rise to near-field *evanescent* modes decaying exponentially into the respective material.[21] This

---

[20] In case of a periodic lattice, this is usually referred to as the Wigner–Seitz cell.

[21] Or even *surface states* being evanescent in both the vacuum and the material, thus localised at/around the surface itself.

situation, depicted in fig. 2.4, can, once rigorously formulated, be described with complex wavevectors, which (by their finite $\mathrm{Im}\,\mathbf{k}$, hence amplitude damping in real-space) have to be included to deal with generalised interface transmission problems [SS15].

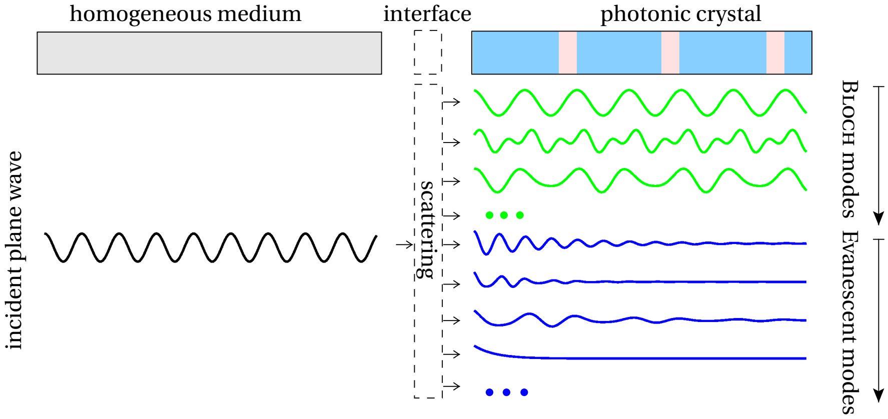

Figure 2.4.: Schematic of wave patterns at an interface of a PhC illuminated by a plane wave from homogeneous space. The waves (excluding the exponential phase factor $\exp(\imath\mathbf{k}\cdot\mathbf{r})$) separate into Bloch modes with a truly lattice-periodic shape function $\mathbf{u}(\mathbf{r})$ (see eq. (2.24)), whereas the evanescent modes carry the real exponential leading to decay into the PhC. Image adapted from [SS15].

In the case of a slab-in-vacuum geometry, these damped modes give rise to light "tunneling" when $\mathrm{Im}(\mathbf{k})$ is small enough to allow the field penetrate the material into a depth not small against the slab thickness. Even though the mode is not truly propagating (not an eigenmode of the geometry in the strict Bloch sense), it exhibits finite transmission (with an exponential dependence from slab thickness).

2.3.2. Band Gaps and Reflectance

Analytic and numeric evaluation of the dispersion relation confirm the (experimental) observation of *band gaps*, *i. e.* intervals of frequency within no crystal wavevector can be found to represent propagating modes. In the case of electron waves, this is the base of success of semiconductor technology [AM76], but it also occurs in dielectric structures [YGL91; Joa+08].

A band gap may only exist along one particular direction of the crystal, and is then called a *partial* band gap. Frequency regions with partial band gaps in all directions are named *total* band gaps.

An Explanation Adopting the analogue argumentation for electronic band gaps [AM76], an illustrative explanation for the occurrence of a band gap in periodic dielectrics along a given direction is based on the energy density (introduced in sec. 2.1.2) [Joa+08]: When the wavevector approaches the BZ border (*i. e.* its distance to the Γ point and the origin of the adjacent translational copy BZ gets the same), the spatial periodicity due to the phase contribution becomes commensurable with the crystal structure periodicity in this direction. The mode basis constituting the bands as they meet at the BZ border (at the same frequency if the potential were zero), superposes to form standing waves.

The finite potential discriminates the two modes according to the energy density, *i. e.* the field intensities within material or vacuum into a *dielectric* and a *air* band, as the energy density, hence the mode frequency, depends on if the knots of the standing waves lie in high-dielectric (air band) or in vacuum (dielectric band, energy reduced by $1/\varepsilon$ for the majority of field "profiting" from the material's internal displacement currents/polarisation) [Joa+08].

Gap size The frequency interval $\Omega_- \cdots \Omega_+$ of the band gap is commonly expressed [YGL91] in terms of the gap-midgap ratio

$$\Delta\Omega/\overline{\Omega} = 2\frac{\Omega_+ - \Omega_-}{\Omega_+ + \Omega_-} \tag{2.25}$$

being properly reduced to stay invariant under structure rescalings (*cf.* sec. 2.1.6).

Dichroic band gaps When a crystalline structure is analysed with respect to its response to circular polarised light, it may exhibit *dichroic band gaps*, meaning that modes within this frequency interval do not exhibit the character of a given circular polarisation. Such features are known to appear in the [001] direction of the single Gyroid (see [Sab+11] and sec. 3.4) and, in particular strength, of the **4srs** quadruple Gyroid (*cf.* sec. 5.3.3).

Analogue to the generic band gap argumentation above, an energy discrimination for light circular polarisations, fed by field energy analysis, can be found in Thiel et al. [Thi+07] and Lee and Chan [LC05]: When the rotatory spatial structure of the wave matches the one of the dielectric structure, a breaking of quasi-continuous variation of field energy concentration with continuous wavelength change occurs, being equal to a forbidden energy interval—a dichroic band gap (for an example, see sec. 2.3.4). This approach conceptually suffers from an asymmetry in lateral direction: On the one hand, the circularly polarised plane wave exhibits continuous translation symmetry, but on the other hand, the helicoidal PhCs are built from discrete lateral translations.

A qualitatively different reasoning applies to *cholesteric* structures, *i. e.* spatial structure within the orientation of an anisotropic $\varepsilon(\mathbf{r})$ rather than the absolute value itself: In case the pitch and rotation sense of a CP plane wave matches the one of the anisotropic permittivity orientation, frequency continuity of adjacent field configurations gets lost, giving rise to true dichroic band gaps, accompanied with high reflectance [Abd08].

Reflectance, band gaps, and low coupling When, for a given frequency being irradiated from free space, no appropriate Bloch mode (in terms of the conserved parallel wavevector, *cf.* sec. 2.1.3, and frequency) exists within the material, this wave cannot propagate within the crystal and must be *fully reflected* (apart from tunneling described above as a consequence of finite penetration depth).

The inverse reasoning is more complicated due to the possibility of *low coupling*: Even if, for a given frequency, propagating modes exist, the reflectance can be high due to little energy transfer between vacuum and Bloch modes.

2.3.3. Laterally (quasi)homogeneous PhC

The Bragg mirror

The simplest case of a structure-photonic crystal is, that the material function alternating along one direction in space with a period of a, while continuous in the other (lateral) directions: the Bragg mirror. It is equivalent to a repeated array of thin films as those described in section 2.1.4. Its first investigation dates back to Rayleigh [Ray87], and is nowadays in use as a versatile module in optics and technology [Men01]. The case of anisotropic ε has been studied by Yeh [Yeh79].

The Bragg mirror exhibits a band gap related to the border of its one-dimensional Brillouin zone (at π/a), at frequencies around $\Omega \lesssim 0.5$ (or lower, depending on the value of ε) [Joa+08; Dec14]. Analogue to the field matching at a single plane interface, the eigenmodes of the Bragg mirror are naturally labelled according to the TE/TM (see sec. 2.1.3), *i. e.* linear polarisations. With respect to circularly polarised light, the Bragg mirror behaves accordingly in projecting the waves on the respective TE/TM constituents. This *achiral* response is not astonishing at all, due to its geometric achirality (from the high (continuous) lateral symmetry).

Helicoidal films: Chiral 2-D PhC

Helicoidal bianisotropic media are uniaxial (with an accentuated direction), laterally homogeneous media with a helicoidal variation of the orientation of the permittivity, which is extended to 2nd-rank tensors. Hence they exhibit chirality, labelled left-handed or right-handed according to their inherent (natural) rotatory sense.

A highly interesting experimental preparation method for media is *glancing-angle deposition* (GLAD) of: PVD (physical vapour deposition) growth of dielectric columns on a substrate, while rotating with a large inclination angle. This way "beards" of helical material are created, consisting of helices homogeneously aligned to each other [RBL95; RB97]. Due to the controlled manner of crystalline growth, they exhibit bi-anisotropy 2.2.2, effectively representing a material of *cholesteric* material anisotropy (inherited from the anisotropy of the deposited crystalline materials). Helical GLAD films reflect preferentially ↺↺, and transmit ↻↺ CP light.

Popta, Sit, and Brett [PSB04] showed that GLAD helix beards made of TiO_2 perform much better in terms of optical activity than conventional chiral materials such as quartz or fluorite. The construction of a circular discriminator from GLAD helicoidal films has been demonstrated by Park, Sobahan, and Hwangbo [PSH09].

2.3.4. "Truly" 3-D dielectric, chiral PhC: Helix arrays

Motivated by the "occurrence" of network topologies resembling helical structures within the diamond network of full-bandgap structures [YGL91], Chutinan and Noda [CN98] calculated band structure for helices arranged in cubic Bravais lattices. They found the BCC arrangement exhibiting the largest band gap of the cubic structures, better than SC or FCC. There were no reports on analysis with respect to circular polarisation equivalence of the computed Bloch modes, so the (obvious geometric) chirality of the helices has not been treated at all.

Experimental investigations of various tetragonal arrays of helices with alternating phase shift/rotation inversion have been carried out by Thiel, Fischer, Freymann, and Wegener [Thi+10] and give a visible CD signal in transmission for globally chiral systems.

Lee and Chan [LC05] study, in order to cast the photonic response known from helicoidal films into a model treatable with frequency-domain theory, a hexagonal[22] lattice of helices ($\varepsilon = 9$ $P6_1$ (No. 169 [Int04])), with particular respect to the chiral character of its Bloch modes.

Departing from the findings of Toader and John [TJ01]: a complete but achiral bandgap for a tetragonal array of overlapping square helices (dielectric contrast of $\varepsilon = 11.9$), they report markedly increased chirality by decreasing the helix radii, thus isolating the helices from each other: They conduct band

---

[22] This *uniaxial* symmetry gives rise to the distinction of lateral and normal directions within the infinite structure, rather than determined by the relative position within a symmetry-reducing slab-like geometry alone—in contrast to inherently isotropic structures like the cubic Gyroid of chapters 3 and 5.

structure calculations via a plane-wave expansion, and reflectance computations off a finite slab, inclined in uniaxial direction, by a scattering matrix method This reveals a dichroic (partial) band gap (↺ reflectance, ↻ transmission) of remarkable bandwidth ($\Delta\Omega/\overline{\Omega} = 26\,\%$) for irradiation in axial direction (parallel to the helix orientations), besides reporting from a narrower single-mode band in lateral direction (↻ reflectance, no proof/picture).

2.3.5. Non-geometric frequency matching: Metamaterials

To conclude the section on chiro-optical physics-by-geometry systems, we want to mention metamaterials, a relative to structure-photonic media, often mentioned in the same breath.

They received their name from consisting of “meta-atoms” (atoms made of atoms, in the bottom-up view: you can design them as you want). In a narrower sense, metamaterials designate structural materials made out of “atoms” staying well below the “visibility” (diffraction) limit of the probing radiation: Structure sizes are typically much smaller than the structure-photonic length scale (*cf.* 1.2.2). Response is rather due to matching in resonance frequencies (metamaterials are usually metallic, hence exhibiting collective electronic, *i. e.* plasmonic resonances) rather than the geometry of field configurations.

(Plasmonic) metamaterials have in common with structure-photonic media the idea to tailor spatial dependence of material response by geometry (but rather the plasmonic, *i. e.* periodic current, distribution, than the electromagnetic radiation field itself). As an example, Gansel et al. [Gan+09] investigated an uniaxial tetragonal array of gold helices, and found considerably circular dichroism from ↺-major attenuation. Pioneering studies in disordered chiral metamaterials were carried out by Hollinger, Varadan, Ghodgaonkar, and Varadan [Hol+92] and Busse, Reinert, and Jacob [BRJ99], reporting considerable optical rotation for a “liquid” of metal helices in the microwave regime.

In contrast to purely dielectric structures, metamaterials suffer from high losses (short-circuit currents of plasmonic resonances). Even in the presence of a dye within structure-photonic media (finite absorption, see sec. 2.1.5), the system keeps, essentially, its photonic properties, subject to attenuation. Typical plasmonic metamaterials, in contrast, rely on the emergent phenomena connected with their non-zero conductivity.

3

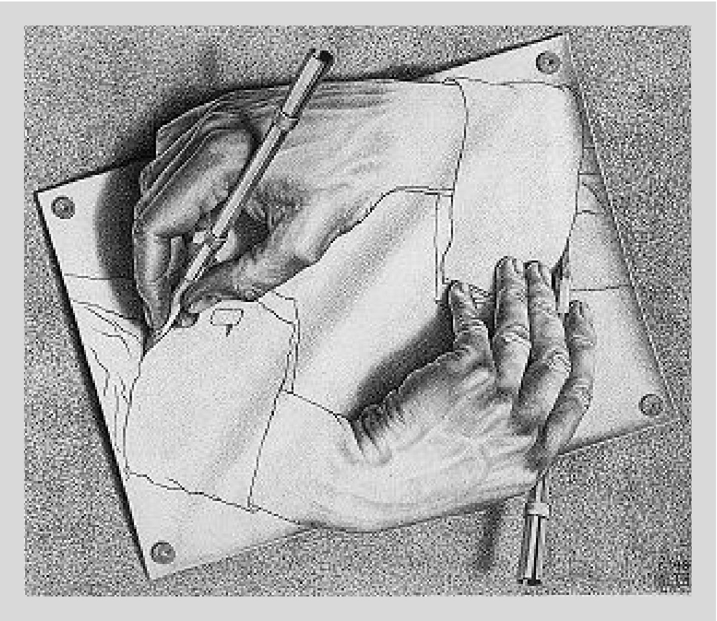

Bi-continuous Geometries and Chirality

M. C. Escher: Drawing Hands (1948)

3.1. Quantification of chirality and circular dichroism

3.1.1. Intrication of geometric and optical chirality

Various approaches have been elaborated to quantify geometric chirality, usually with the aim to develop a convincing[23] chirality measure by the enantiomers' dissimilarity from nearest achiral "neighbours" [Pap+03], HAUSSDORF distance-like approaches, and some other ad-hoc variations.

However, when asking for the chiral *response to light*, a quantification of chirality is naturally based on the chirality of the light, within the structure, and reflected from it.

Crystals and disordered systems For crystalline media, a closer look to the nature of BLOCH modes is appropriate in any case. [LC05; Sab10; Sab+11] have introduced, as (continuous) measures of the handedness of BLOCH modes, circular dichroism indices, by comparing them to (discretely chiral) plane waves. These data contains information on coupling to vacuum modes on a per-mode basis, thus the maximum possible information from mode analysis for the interaction with the incident light field. Note that these measures refer to unitcell-averages, *i. e.* represent a property of a BLOCH mode, and is as independent from the actual (finite) geometry of the crystal as the band structure, inheriting its conceptual difficulties to link to interface phenomena and their interpretation.

However, in systems bearing crystalline order, there is no well-defined mode basis (which is universal, or at least to be developed in a constructive way). So for a programme for quantification feasible for both crystals and disordered systems, we need either some ad-hoc hypothesis based on approaches from geometry or fundamental physics[24], or some effective measure creating an "empirical" link between handedness of light and material response.

3.1.2. Cumulative circular contrast

As a such, we now argue in favour of the cumulative view on the reflectance (CCR) or transmission (CCT) difference between ↺↺ and ↻↻ light in a particular given geometric and electromagnetic situation. These measures are then inherently geometry-dependent.

The requirements are

- Applicable to arbitrary structured media, especially non-periodic (in which the prerequisites to the BLOCH theorem are not fulfilled, hence BLOCH wavevectors and a BZ are not defined),
- Depicting response on circular polarised light,
- Being sufficiently "phenomenological" (offering interpretation in a context which is easily extendible to a experimental context)
- Additivity (proportional to circular dichroism, *i. e.* twice the single-CP reflectance yields twice the CD measure),
- No overrepresentation of the *relative* difference in favour of the absolute difference,

---

[23] In a natural way, a chirality "measure" has to overcome the traditional binary and point-centred perception concept of chirality. So *continuity* and a sensible approach to deal with *locality* and *translational "invariant"* aspects of geometry have to be concise.

[24] Subject to current considerations is LIPKIN's Z^{00} Zilch quantity [Lip64], probably representing some "flow of chirality" [BN11], see on page 107 for a short outlook.

- At least, preserving the frequency resolution.[25] In fact, this makes this measure be a *spectrum* itself.

The cumulative contrasts fulfilling these points are defined, in terms of the intensity reflectance R^e and transmittance T^e of the circular polarisation senses e = LCP or RCP (and $-e$ the other) as their respective difference, cumulated from some starting frequency Ω_0 on (which will usually set to zero, unless a variant choice appears reasonable):

$$\begin{aligned} \mathrm{CCR}^e(\Omega) &= \int_{\Omega_0}^{\Omega} \mathrm{d}\Omega' \left(R^{-e}(\Omega') - R^e(\Omega')\right) \\ \mathrm{CCT}^e(\Omega) &= \int_{\Omega_0}^{\Omega} \mathrm{d}\Omega' \left(T^{e}(\Omega') - T^{-e}(\Omega')\right) \end{aligned} \tag{3.1}$$

The abbreviation CCR/CCT stands for Cumulative Circular Contrast in Reflectance/Transmission, respectively.[26] For lossless media, *i. e.* when the “macroscopic” flux conservation $R + T = 1 \forall \Omega$ holds true, the both quantities are complementary to each other: then $\mathrm{CCR}^e - \mathrm{CCT}^e \equiv 0$ is obvious (Note the minus sign corresponding to the sign switch between the equations in (3.1) to not to have to switch CC sign on comparing CCR and CCT of the same structure).

CC data can be easily *a posteriori* generated by point-wise evaluation of FDTD reflectance/transmittance spectra, or from any other source of reflectance, such as computed from complex band structure calculations [SS15], or from experiments.

Dimension CCR[27] is “dimension-less”, as it inherits its (natural) units from Ω, so that they implicitly depend on a, some inherent length scale of the system even in absence of crystalline structure. If you think of an ensemble of systems with polydisperse a: then smearing of the CCR’s Ω dependence shows up that the most relevant part of a CCR curve is its end-value (at best, spectra end within a region of high transmission and negligible CD).

Relative handedness Given a structure with a well-defined handedness (such as an unbalanced arrangement of helices—for the decision of the Gyroid’s handedness see sec. 3.2.2), the relative “sign” of e will be chosen to fit into the respective handedness convention. In those cases, the CC measure(s) will be used without indicating the polarisation—reflecting the “scale-free-ness” (relativity) of handedness.

Interpretation—How to read CCR data Though sounding naïvely to just subtract the two reflectances of opposite handedness, we will discuss now the benefits and implications of CCR data.

It has to be read left-to-right, as it depicts (in effect, averages over) the difference *within this finite frequency interval*, starting at its lower bound at zero.

CC visualises the *effective dichroic band-gap width* (by its end-value), and the *frequency range* over which this growth can be observed.

---

[25] Similar routes, but with out-integrated frequency dependence, have been applied formerly, *e. g.* by Saba et al. [Sab+11], Wasserka [Was13], and Saba, Wilts, Hielscher, and Schröder-Turk [Sab+14], to quantify circular dichroism. However, any kind of an data evaluation routine looking at a fixed frequency (or frequency range) will then be susceptible to red- and blue-shift trends (caused by changes in volume filling, *e. g.*), and mislead to conclude on either false-positive or false-negative trends. Moreover—as those effects are physical, actually—this implies special care to be taken for both finding robust measures for effects otherwise described just qualitatively, and to the actual experiments designed not to alter the nature of the structure by excessively altering the volume filling.

[26] Which “C”s originates in which words is left to the reader’s imagination.

[27] In the following, we will predominantly stick to the CCR as long as it differs from CCT only by artefacts of the numerical method.

Note that, in all CC plots, a "‘Full-CD line"’ line of slope 1 will be included, in order to quantitatively compare different CC data with different scales in frequency and absolute value.

Possible further normalisation steps You can think of normalising CC data to some CC efficiency: CCR $/\phi$, quantifying the efficiency of material deployment. Such a normalisation might also deal with ε, but is problematic, as the qualitative scattering behaviour changes with the dielectric contrast.[28]

The CC measures, when derived from averaged, “macroscopic” energy flux measurements, are insensitive towards the very polarisation of the reflected/transmitted light. A possible generalisation might include a polarisation analysis of , giving rise to a set of 2×2 “partial CC” spectra

3.2. The (single) Gyroid

In his seminal work in the late 1960s, Schoen [Sch70] described the Gyroid as a particularly remarkable member of the family of *minimal surfaces*[29] *i. e.* surfaces representing local minima of the surface energy (area and mean curvature) among all possible curved surfaces extending in space. It is a triply-periodic minimal surface (TPMS) exhibiting BCC cubic symmetry (see next section 3.2.1), dividing space into two (not interconnected) *channels* smoothly linked in all three spatial dimensions (hence the name TPMS).

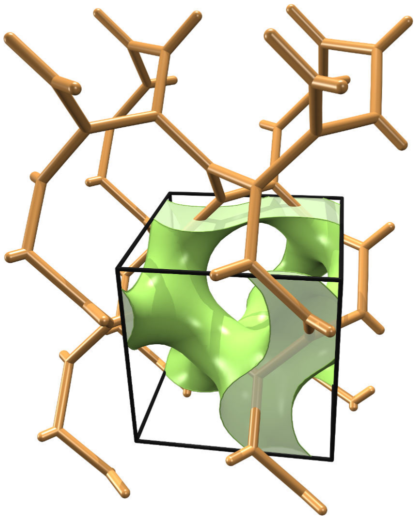

Figure 3.1.: The single Gyroid: Nodal approximation within a conventional cubic unit cell (green), superimposed with the **srs** network graph (orange), continued $2 \times 2 \times 2$ unit cells. Especially the helical network elements parallel to the Cartesian axes are visible in the upper right part of the image. Source: [Sab+14]

Single Gyroid A single of the Gyroid channels, when viewed separately, is *handed*, *i. e.* chiral, the other channel representing the opposite enantiomer, so with no translation-rotation operation, the both channels can be exactly superimposed.

When the channel is the regarded object (rather than the surface itself), it is commonly referred to as the *single Gyroid*; by making the channels distinguishable (here: by filling with different material)

---

[28] Think, *e. g.*, of the $\phi \not\ll 1$ and $\varepsilon \not\gg 1$ shift to weak diffraction well governed by the first Born approximation—which is, in fact, a *very* bad approximation to the diffraction behaviour of structure-photonic crystals.

[29] For a comprehensive list of minimal surfaces and their nodal approximations, see [SN91] and (illustrated) [MK03]. A comprehensive historical overview over the history of discovery can be found in [HOP08].

the symmetry is lowered (removal of inversion symmetry) by the breakthrough of the chiral (non-symmorphic) symmetry of the single channel.

The TPMS Gyroid is a surface of constant mean curvature (CMC), the natural solution of the surface [tension] minimisation problem.[30] By allowing the two channels to have different volumes, the relaxation yields the family of CMC Gyroids, characterised by the *volume filling fraction* ϕ of the (in this study) channel filled with high-dielectric material.

Lowest Fourier modes, and the Nodal surface The lowest Fourier mode of the balanced ($\phi = 50\,\%$) single Gyroid CMC channel (*cf.* eq. (3.3.1)) is a smooth function of space. Its nodal surface (surface of zero points) is a remarkably accurate approximation to the TPMS Gyroid [SN91], as are the (generalised) equipotential surfaces of this formula to CMC surfaces (see sec. 3.3.1).

The network graph The $(10,3) - a$ graph introduced by Laves [Lav32] and Heesch and Laves [HL33] and named LAVES' graph thereafter by Coxeter [Cox55], has been shown to be topologically equivalent to a single Gyroid channel—in fact precisely tracing its geometry. It is customarily abbreviated to **srs** (or **1srs** in order to distinguish from multiple interlaced **srs** networks [Sab+11]) This name arises from its occurrence in the network of silicon atoms in the cubic LAVES phase alloy SrSi_2 [HOP08].

3.2.1. Symmetry

The Gyroid TPMS (and all other forms of balanced Gyroid representations) exhibits $Ia\bar{3}d$ (No. 230 [Int04]) symmetry, including a spatial inversion centre, hence being achiral. Introducing a distinguishing criterion between the channels (referred to as *solid/material*, and *void/vacuum* phase), or inherently asymmetric realisations (wires along the network edges, *cf.* sec. 3.3.2) reduces the symmetry to the non-symmorphic $I4_132$ (No. 214) space group.

The solid and void phases exhibit opposite handedness, whereas topologically (and for the balanced cases even geometrically) identical otherwise. This symmetry is remarkable and unusual for chiral objects.

Another noteworthy property of the Gyroid geometry is the possibility to interweave several (three [Sab10], four [Sab+11] or eight [Sab+13]) networks (each with sufficiently wide hollow space, of course) to form geometries called **4srs** and **8srs**, respectively. This will be described and performed in more detail later in sec. 5.3.3, for the transition **1srs** →**4srs**, to "interpolate" the chiral properties of these two geometries.

3.2.2. Handedness, Chirality

As already mentioned in connection with fig. 3.1, the Gyroid is a subtle join of helical elements. We may refer to the thorough discussion within [Sab+14], and mention only some details: The "triangular" helices of the $\langle 111 \rangle$ directions, and the "octagon" helices of the $\langle 100 \rangle$ directions (the ones the Gyroid will be built from by the helical model, *cf.* sec. 3.3.3) hence show the characteristic conventional helical sense of the Gyroid, whereas the "hexagonal" $\langle 111 \rangle$ and "quadratic" $\langle 100 \rangle$ helices exhibit the opposite turning sense.

---

[30] This is realised, *e. g.*, in an experiment by a soap film relaxing within a wire frame determined by symmetry, or in its simulation counterpart, *cf.* BRAKKE's *Surface Evolver* [Bra92]. To yield the Gyroid minimal surface, one has to ensure the volumes of each channel balanced at 50 %. This will be implied by following the boundary conditions from topology and symmetry.

Along the mere number of helices of left and right handedness, no decision on an "absolute" handedness can be made, so it will be *defined* by convention, introduced in [Sab+11]: The handedness of the Gyroid equals the one of the 3_1 axes surrounded by the "triangle" network helices of the $\langle 111 \rangle$ direction. This thesis will sticks to the handedness convention.

3.3. Ways of representing and creating the Gyroid

In this section, we will discuss remarkably distinct approaches to structure space in order to reproduce some or all of the properties of a Gyroid, such as the bi-continuity, topological equivalence, and symmetries.

A special focus will be drawn on the volume filling fraction ϕ, arising from the different model approaches, as the eigenfrequencies of BLOCH light waves in the material are dependent in a complicated (but largely monotonous) way from the fraction of space filled with high-dielectric [Joa+08].

Three distinctly different modelling paths for the Gyroid will be presented, each with its own strengths and disadvantages. Table 3.1, at the end of the section on page 42, will summarise their parameters, and gives some values preferentially used in the course of this study.

3.3.1. Nodal approximation to CMC surfaces

The lowest Fourier harmonic of the balanced single TPMS Gyroid, shifted by a *threshold* t, reads as

$$g(\mathbf{r}) = \sin(Gx)\cos(Gy) + \sin(Gy)\cos(Gz) + \sin(Gz)\cos(Gx) - t = 0 \tag{3.2}$$

with nondimensionalisation $Ga = 2\pi$ [SN91; MK03].

Its zero iso-surface ($t = 0$) proves to be a ready approximation of the Gyroid TPMS, sharing its symmetry between void and material phase, and inherent smoothness. Moreover, by varying t, the volume fractions of the channels can be easily manipulated.

1-D volume filling fraction of a shifted sinusoid

Due to the nonlinear dependence on spatial coordinates in eq. (3.2), evaluation of the volume filling fraction as a function of the threshold is not possible analytically.

As a one-dimensional toy example for the analytic computation of a volume filling fraction (refer to figure 3.2 for visualisation), consider the "volume" defined by the fraction of a sinusoid[31] function lying below some (spatially constant) *threshold* t (analogue to the nodal approximations to TPMS):

$$g(x) = \cos(x) + t \tag{3.3}$$

Being inside the testing material at x is equivalent to the conditional $g(x) \overset{?}{\geq} 0$, or the value of the HEAVISIDE step function $\Theta(-g(x))$. For $-1 < t < +1$ we know (from continuity) $g(x)$ has two zeroes x_i: the first when $g(x)$ crosses the zero axis ("surface") from positive to negative values, "switching on" the Θ conditional, the second x_2 when $g(x)$ switches to positive values again. Inversion of (3.3) provides

$$\begin{aligned} x_1 &= \arccos(-t) \\ x_2 &= 2\pi - \arccos(-t) \quad , \end{aligned}$$

---

[31] Choosing w. l. o. g. the cosine in eq. (3.3) avoids ambiguities in root-finding.

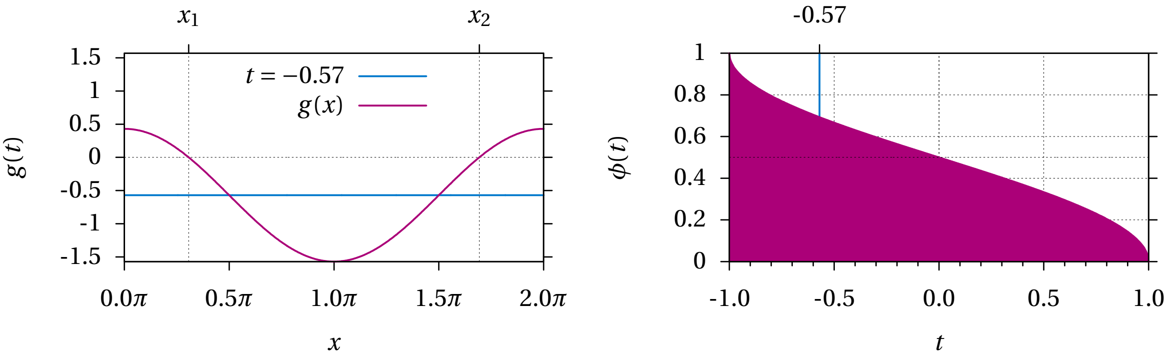

Figure 3.2.: Visualisation of filling-fraction computation from a one-dimensional nodal formula $t \mapsto \phi$ with an example threshold $t = -0.57$.

so that the computation of volume filling

$$\phi(t) = \int_0^{2\pi} \frac{\mathrm{d}x}{2\pi} \Theta(-g(x)) \tag{3.4}$$

simplifies to the interval balancing (by knowing $g(x) < 0 \Longleftrightarrow \Theta(-g(x)) = 1 \Longleftrightarrow x_1 < x < x_2$)

$$\phi(t) = 1 - \frac{1}{2\pi}(x_2 - x_1) = \frac{\arccos(t)}{\pi} \tag{3.5}$$

to be steadily continued from the interval borders to $\phi(x \le -1) = 1$ and $\phi(x \ge 1) = 0$.

From Sinusoid to 3D Nodal Formulae

The constraint (3.2) defines the single Gyroid in its nodal approximation. Viewing line-wise with constant y and z (interpreting the $\mathrm{d}z$ integral in the RIEMANNian sense as regarding a column along its height $0 \cdots 2\pi$ over its base square of area $\mathrm{d}x\,\mathrm{d}y$), the integration over the x direction is reducible to the one-dimensional case described above by eq. (3.5):

$$\begin{aligned} 0 \overset{!}{\ge} g(x,y,z) &= \big(\sin(x)\cos(y) + \cos(x)\sin(z)\big) + \big(\sin(y)\cos(z) + t\big) = \\ &= \sqrt{\sin^2(z) + \cos^2(y)}\cos(x+\varphi) + \big(\sin(y)\cos(z) + t\big) \\ \Longleftrightarrow \quad \cos(x) &+ \frac{\sin(y)\cos(z) + t}{\sqrt{\sin^2(z) + \cos^2(y)}} \overset{!}{\le} 0 \end{aligned} \tag{3.6}$$

Choosing the phase shift φ (arising from the used trigonometric identity) to zero is justified by the arbitrary choice of the x interval to evaluate (as long as its length of 2π is maintained).

So, for fixed y and z (a single RIEMANN "summand" within the y and z integrals) we know the "x-partial filling fraction" (from eq. (3.5)) to be

$$\phi_x(y,z) = \int_0^{2\pi} \frac{\mathrm{d}x}{2\pi} \Theta(-g(x,y,z)) = \frac{\arccos(t_{yz})}{\pi} \tag{3.7}$$

with the effective x- and y-dependent threshold

$$t_{yz} = \frac{\sin(y)\cos(z) + t}{\sqrt{\sin^2(z) + \cos^2(y)}} \quad , \tag{3.8}$$

given the case $\arccos(t_{yz})$ is defined, or, equivalently: the given x "column" (of fixed y, z position) does not consist fully of material nor of vacuum.

We may express this case distinction in terms of a generalised definition of the integrand function:

$$\widetilde{\arccos}(t) = \begin{cases} \pi & t < -1 \\ \arccos(t) & -1 < t < 1 \\ 0 & t > 1 \end{cases} \tag{3.9}$$

With that, in principle, we have the analytical form of the volume fraction (applying the substitutions $a = \cos(y)$ and $b = \cos(z)$, respectively):

$$\begin{aligned} \phi(t) &= \iiint\limits_{[0:2\pi]^3} \frac{\mathrm{d}^3 r}{8\pi^3} \Theta(-g(\mathbf{r})) = \\ &= \frac{1}{4\pi^3} \int_1^{-1} \frac{\mathrm{d}a}{\sqrt{1-a^2}} \int_1^{-1} \frac{\mathrm{d}b}{\sqrt{1-b^2}}\, \widetilde{\arccos}\left(\frac{b\sqrt{1-a^2}+t}{\sqrt{a^2-b^2+1}}\right) = \\ &= \frac{1}{4\pi^3} \int_1^{-1} \frac{\mathrm{d}a}{\sqrt{1-a^2}} \left(\int\limits_{\text{◙}^-} \pi + \int\limits_{\bullet} \arccos(t_{ab}) \right) \frac{\mathrm{d}b}{\sqrt{1-b^2}} \end{aligned} \tag{3.10}$$

where ● denotes the range of $b \in [-1;1]$ in which $-1 < t_{ab} < 1$, *i. e.* the ordinary $\arcsin(t_{ab})$ is defined ($0 < \varphi_x < 1$), and ◙^- corresponds to the area where $t_{ab} < -1$ ($\varphi_x \equiv 1$). In dependence of t and a, the borders for the b integration compute to

$$\begin{aligned} (3.8) \quad & \left|t_{yz}\right| = 1 \\ b_\pm &= \frac{t\,(1-a^2) \pm \sqrt{2-a^4+a^2-t^2}}{a^2-2} \\ b &\in \begin{cases} [-1; b_-] & \text{◙}^- \\ [b_-; b_+] & \bullet \end{cases} \end{aligned} \tag{3.11}$$

This result has the aftertaste of not being solvable algebraically.

A crude but remarkably accurate approximation

Numerical evaluation of either the full-volume Gyroid integral eq. (3.2) or the two-dimensional problem above, *i. e.* eq. (3.10) gives, at a first glance to not too minute filling fractions (*i. e.* looking on the linear graph at the right side within fig. 3.3), a remarkably simple approximation for the Gyroid volume filling fraction:

$$\phi(t)^{\text{approx}} = \begin{cases} 0 & t < -1.5 \\ \frac{1}{2} + \frac{1}{3} t & \text{else} \\ 1 & t > 1.5 \quad , \end{cases} \tag{3.12}$$

which approximates the "exact" (volume filling fraction determined by numerical evaluation, *i. e.* voxel counting) volume filling fraction within the interval $-1.3 < t < 1.3$, corresponding to $6.2\,\% < \phi < 93.8\,\%$

up to a deviation of $\Delta\phi = |\phi^{\text{approx}} - \phi^{\text{exact, num.}}| \leq 1/150$. This linear[32] relationship has at least once been observed in literature [LRT96], but was not subject to further investigation.

Figure 3.3 (linear plot) illustrates the apparent accurateness of this approximate function, which should suffice for any case with a substantial fraction of space occupied by both material and void.

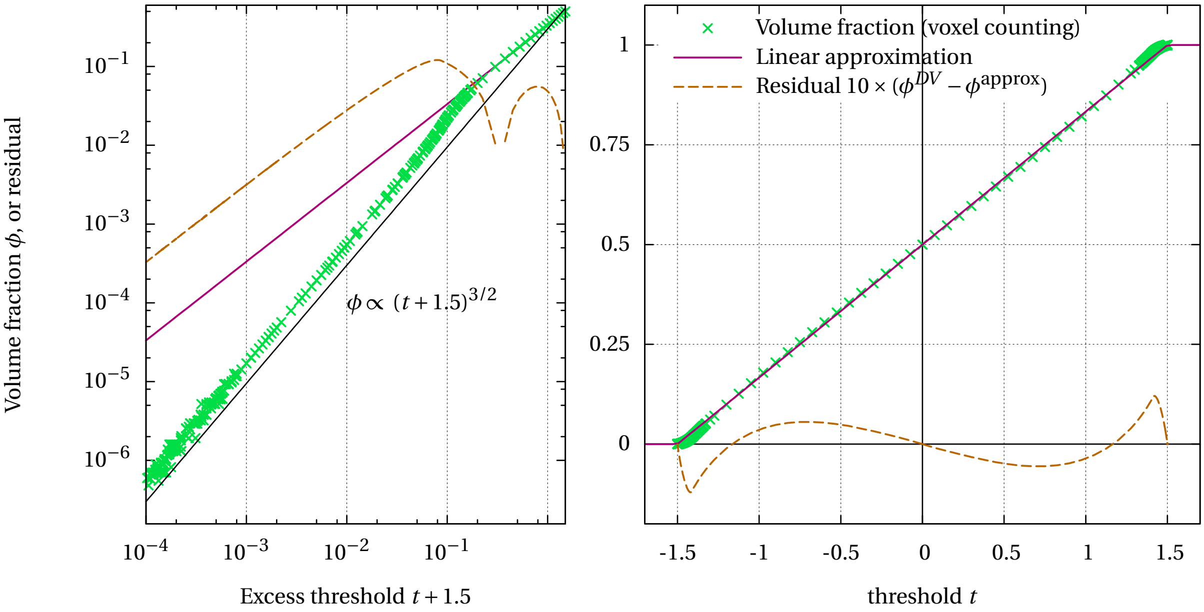

Figure 3.3.: (Voxel counting) Single Gyroid volume filling fraction from nodal approximation, in dependence on the threshold t (left: log-log, right: linear axes). Counting voxels filled at a given t reveals a near-linear behaviour when the distance from the extremal threshold $|t| = 1.5$ is more than about 10^{-1}. At lower distances, the function crosses over to a power law $\phi \propto (t+1.5)^{3/2}$. Residual (logarithmic plot: absolute value) is exaggerated tenfold. Direct Voxels resolution: up to 721 px a^{-1}.

The observed t^1 and $t^{3/2}$ power laws can be argued the following way[33]: With $|t| < \sqrt{2}$, the nodal surface is bi-continuous, the minor channel breaking apart from into isolated chunks of more and more spherical "atoms" at the vertex mid-points, progressing to lower excess t [Woh+01]. The appropriate coordinate system to describe the volume dependence on t (to expand eq. 3.2 in) is

- for the bi-continuous cases, a cylindrical one, viewed at the cross-section through an edge.Volume filling will be proportional to r^2 in leading order.
- spherical when the minor phase is no longer connected, accordingly with a $\phi \propto r^3$ behaviour

(r being each the distance from the nodal surface to the coordinate origin). As $r^2 = \mathcal{O}(t)$ from TAYLOR expansion of the cosine(s) in eq. 3.2, the behaviour of $\phi(t)$ becomes obvious (or, at least, plausible).

Note that for the Primitive and Diamond surfaces' nodal approximations, a similar evaluation might be realisable, but the deviations from linear $\phi(t)$ behaviour occur at much lower t distance from the borders of the allowed interval [LRT96; Dec14].

---

[32] By additionally considering cubic terms (only odd powers of t are allowed due to inflection symmetry at $t = 0, \phi = 50\,\%$), the accuracy may be increased up to 5×10^{-4}.

[33] For this consideration, Matthias SABA should be credited.

“Length scale” and behaviour on distortion

The nodal approximation is a smooth function of space, and as a such has no inherent (model-dependent) length scale, in contrast to the wire models presented in the following. Moreover, as the distortion field operation will uniformly “smoothly” act on all space points (or, in the real case, every voxel), the nodal approximation proves very resistant to changes in volume filling fraction, as long as the viewed space region is commensurable with the distortions (as it will be by construction, see next chapter).

3.3.2. The srs Network Graph

In a regular geometric realisation (locally identical vertices), the **srs** network skeleton graph, created from tracing a Gyroid channel, inherits its full body-centred $I4_132$ symmetry, including the chirality and the possibility for two enantiomers (see introductory section 3.2 and figure 3.1).

Vertices and Edges

The primitive BCC unit cell holds 4 three-connected vertices, linked by 6 edges; hence the conventional cubic unit cell holds 8 vertices with 12 edges.

The positions $\mathbf{V}_i$ of the points (vertices) and connections (edges) building up the **srs** network are taken from the comprehensive structures database RCSR (Reticular Chemistry Structure Resource) [OKe+08; 14]. For this work, they are adapted to stick to the (crystallographic) coordinate origin convention, the same as for the nodal approximation (3.3.1, eq. (3.2)) and the helical models, see section 3.3.3. Moreover, the points have been freed from lattice translation duplicates[34], overall translated, and enantiomer-flipped $z \to -z$.

Finally, the points to present here and duplicated by a primitive BCC lattice vector (half cube body diagonal). So, besides showing up within a cube-shaped unit cell with its easily comprehensible symmetry operations, the choice of (conventional) unit vectors is unique (Cartesian axes, length: a). The points and connections are:

$$(\mathbf{V}_1\,\mathbf{V}_2\,\mathbf{V}_3\,\mathbf{V}_4\,\mathbf{V}_5\,\mathbf{V}_6\,\mathbf{V}_7\,\mathbf{V}_8) = \frac{a}{8}\begin{pmatrix} 1 & 7 & 7 & 5 & 3 & 3 & 1 & 5 \\ 5 & 7 & 1 & 7 & 5 & 3 & 3 & 1 \\ 7 & 7 & 5 & 1 & 1 & 3 & 5 & 3 \end{pmatrix}$$

$$\begin{array}{ll}
\mathbf{V}_6 \longleftrightarrow \mathbf{V}_5 & \quad \mathbf{V}_2 \longleftrightarrow \mathbf{V}_5 + \frac{1}{2}[111] \\
\mathbf{V}_6 \longleftrightarrow \mathbf{V}_7 & \quad \mathbf{V}_2 \longleftrightarrow \mathbf{V}_7 + \frac{1}{2}[111] \\
\mathbf{V}_6 \longleftrightarrow \mathbf{V}_8 & \quad \mathbf{V}_2 \longleftrightarrow \mathbf{V}_8 + \frac{1}{2}[111] \\
\mathbf{V}_5 \longleftrightarrow \mathbf{V}_4 & \quad \mathbf{V}_5 \longleftrightarrow \mathbf{V}_1 + [00\bar{1}] \\
\mathbf{V}_7 \longleftrightarrow \mathbf{V}_1 & \quad \mathbf{V}_7 \longleftrightarrow \mathbf{V}_3 + [\bar{1}00] \\
\mathbf{V}_8 \longleftrightarrow \mathbf{V}_3 & \quad \mathbf{V}_8 \longleftrightarrow \mathbf{V}_4 + [0\bar{1}0]
\end{array}$$

Every point is connected by three edges to points which share one coordinate and differ in the other two by $a/4$ (*i. e.* edges are $\langle\frac{1}{4}\frac{1}{4}0\rangle$ vectors with the length $a/\sqrt{8}$).

---

[34] Of course, the edges *must* have connections to points within adjacent unit cells (see below), in order to create a connected network.

Geometry from the Network

To create a structure to be examined with respect to its photonic properties, the edges are inflated to cylindrical "wires" with finite cross-section, or radius, respectively.

In practice, every edge $\mathbf{V}_a \longleftrightarrow \mathbf{V}_b$ (as defined above) will be replaced by a cylinder between $\mathbf{V}_b$ and $\mathbf{V}_a$, with a radius r. For a first estimate, the *volume fraction* of a regular **srs** will then compute from the number of cylinders, their length and cross-section to

$$\phi^{\text{first}} = \frac{1}{a^3} \cdot 12 \cdot \frac{a}{\sqrt{8}} \pi r^2 = 3\sqrt{2}\pi \left(\frac{r}{a}\right)^2 \tag{3.13}$$

This is an overestimation, as the intersections of the tubes at the vertices are counted twice.

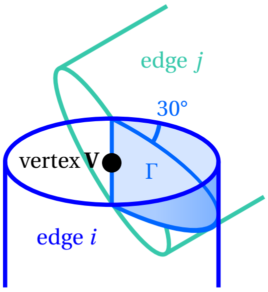

Figure 3.4.: Cylinder intersection at a vertex.

The duplicate per-cylinder intersection volume Γ at a vertex is half-circular and wedge-shaped, as depicted in fig. 3.4 (and accounts for both meeting cylinders). Its volume computes to

$$\Gamma = \int_0^{\pi} \mathrm{d}\varphi \int_0^{r} \mathrm{d}\varrho \varrho \sin(\varphi) \cdot \big(\varrho \sin(\varphi)\big) \tan(30°) = \frac{\pi r^3}{6\sqrt{2} a^3} \quad . \tag{3.14}$$

At every of the eight vertices, six of those wedges have to be subtracted, so that the exact volume fraction is given by

$$\begin{aligned} \phi =& \phi^{\text{first}} - 6 \cdot 8 \cdot \Gamma = \\ =& 3\sqrt{2}\pi \left(\frac{r}{a}\right)^2 - 4\sqrt{2}\pi \left(\frac{r}{a}\right)^3 \end{aligned} \tag{3.15}$$

restricted to the r range of no contact between the distinct wedges, *i. e.* wedge height $\leq$ half edge length, or $r \leq \sqrt{3/32} \approx 0.306\,a$, at $\phi = 73.9\,\%$.

To obtain a wire radius for a given volume filling fraction, one must either conduct a painful inversion of eq. (3.15), or apply a numerical root-finding algorithm.[35] The resulting volume filling fractions are depicted in fig. 3.5. The volume fractions observed by voxel counting on discretised **srs** realisations are in well agreement with the values from eq. (3.15), at least within the relevant range $r/a \leq 0.2$, or $\phi \leq 0.4$.

An additional natural freedom within the geometry construction from the **srs** network is to place "atoms" with finite radius $r_{\mathrm{A}} > r$ at the vertices, resembling *ball-and-sticks* molecular construction kits.

Length scales

With respect to distortive manipulations of the geometry, the explicit and implicit length scales are to be discussed. Note that any distortion of the network will be topology-preserving (or just "adding" topological links into the structure by overlap due to massive distortion distances). Even at distortions large compared to typical edge lengths, the vertex connectivity will persist (though the network may hardly resemble the original **srs**, with acute angles, edge intersections etc.).

Wire cross-section As a globally fixed parameter of the network,[36] the wire thickness r, in the first instance, defines the volume filling fraction, and the short-range surroundings of points. Within

---

[35] The finite precision of the r found by numerical solvers for a given ϕ is tolerable, as the number of voxels is finite, too. Within the structure initialisation, the iterative NEWTON root-finding algorithm `gsl_root_fdfsolver_newton` from the GNU GSL library [Gal09] comes to use. Departing from the first guess from eq. 3.13, the residual $|r_n - r_{n-1}|$ drops below 1×10^{-13}, typically after $n = 12$ iterations, corresponding to an error of the order of one single voxel at a utopian resolution of 10^4 px a^{-1}.

[36] It is, of course, possible to vary r within the network (given, a sound motivation), but with this in mind, the boundary towards dropping the circular shape of cross-section is too nigh to be ignored as well—all those are kinds of short-range correlation fine adjustment with disputable impact on the low-frequency non-local testing which is the scope of this study, but introducing a diverging number of additional degrees of freedom into the system.

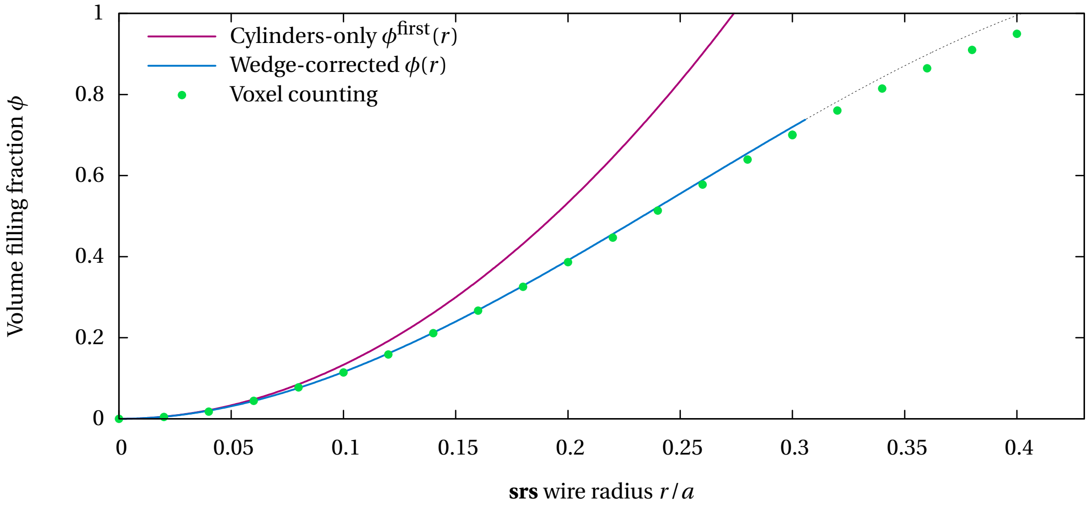

Figure 3.5.: (Analytic and voxel counting) Volume filling fraction of the **srs** network as a function of the wire thickness, approximate by cylinder lengths only (eq. (3.13)) and corrected (eq. (3.15), solid line up to its validity limit, see text). The mediocre voxel counting resolution of 31 px a^{-1} (giving rise to aliasing artifacts for edges perpendicular to voxel edges) may explain the systematic mismatch from the analytic formula.

a distance of the order of r, a point can be characterised by either lying near the surface or deep within a wire, or, at most, near a vertex.

Atom radii If desired, the three-connected vertices can be occupied by spheres with a finite radius r_A, which will be fixed within the whole network for the same reasons as the wire thickness.

Vertex positions and edge lengths The correlations of longer distances than r are implied by the vertices and their relative arrangement. Especially, the local signature of chirality will at first be visible at distances on the order of edge length, when the unbalanced dihedral character of the vertex coordinations are accounted.

Edge subdivisions In order to increase the density of points manipulable by distortion operations, it is possible to divide the edges of the network by arbitrarily many two-connected vertices. At the latest with subdivided edges, it is necessary to build edges from *spherocylinders*, *i. e.* to surround every vertex with a sphere of the same radius as the wire, so that gaps at non-straight junctions will be avoided.

3.3.3. The Gyroid built from distinct Helices

The Gyroid network contains solid helices wound along the 4_1 axes in the Cartesian directions (see fig. 3.1), matching the turning sense chosen for the Gyroid handedness definition, see sec. 3.2.2.

Inspired by the construction or modeling of chiral geometries from distinct helices [Fre+10; Dem+12], a remarkable accurate modelling of the Gyroid by the aforementioned helices has been developed by Wasserka [Was13] and is refined within this thesis.

A single (mathematical) helix will be parametrised by its pitch λ, the (bend) radius R, and the mathematical description of its core fibre

$$H(\mathbf{n},\mathbf{O},\mathbf{a},R,\lambda) = \left\{ \mathbf{x} | \mathbf{x} = \mathbf{O} + D_{\mathbf{n}}^{\mathbf{a}} \begin{pmatrix} -R\cos(2\pi z/\lambda) \\ R\sin(2\pi z/\lambda) \\ z \end{pmatrix} \right\} \quad , \tag{3.16}$$

with $\tilde{z} = (\mathbf{x} - \mathbf{O}) \cdot \mathbf{n}$, and a rotation matrix $D_{\mathbf{n}}^{\mathbf{a}}$ tilting the helix axis into the desired normal $\mathbf{n}$, and spinning around the axis so that $\mathbf{a} - \mathbf{n} \cdot \mathbf{a}$, the perpendicular component of the phasing vector $\mathbf{a}$, points towards the helix path from the origin (centre of mass) of the helix.

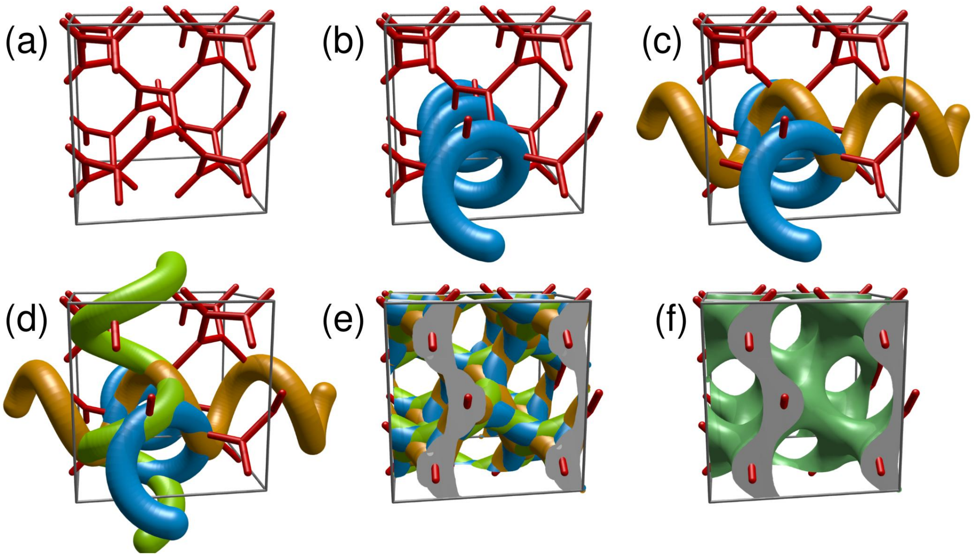

Figure 3.6.: Tracing the helical geometry of the single Gyroid with helices. **(a)** topology represented by its skeletal graph, 2 × 2 × 2 unit cells. **(b-d)** Construction from helices in the three ⟨100⟩ directions. **(e)** Accuracy of the construction: BCC basis helices (in total, 16 helix turns per direction; excess structure cut away). **(f)** The Gyroid from the nodal approximation, in comparison.

Three helices per unit cube

Demetriadou, Oh, Wuestner, and Hess [Dem+12] introduced their "tri-helical model" as a model which can be dealt with analytically, while sharing selected symmetry elements with the Single Gyroid: Oriented in ⟨100⟩ (Cartesian) directions, three isolated conductive helices mimic (some of) the helical channels surrounding the 4_1 screw axes of the Gyroid, while continuously varying the pitch[37], and interconnection between the distinct helices is deliberately circumvented.

While a detailed re-build of a Gyroid structure was not the main scope of that model, it underlines a fact showing up a new way of both seeing and constructing a Gyroid: The helical character of the

---

[37] Note that, only for selected pitch values, this is compatible at all with crystallographic operations. Screw axes (as those of the Gyroid) must have a pitch being an *integer multiple* (1 a for 4_1, and 2 a for 4_2) of the cubic unit length.

Gyroid's topology is well-known from helix-like sub-networks within the **srs** network, *cf.* [Sab+14]. Any edge of the **srs** skeleton graph is a member of multiple helices, each lying in one of the ⟨100⟩ directions.[38]

In his research project (which was the immediate precursor to this work), Wasserka [Was13] has—inspired by the idea from [Dem+12] to build structures from distinct helices—investigated a remarkably accurate Gyroid replica from placing helices along the primitive cubic ⟨100⟩ axes (with the proper pitch of the cubic lattice constant, $\lambda = a$). Per cubic unit cell, a total of three helices are thus positioned in a way that they mimick the Gyroid's 4_1 axes. This process is visualised in fig. 3.6. The helix curves are given by[39]

$$\text{SC Gyroid:} \left\{ \begin{array}{l} H(\mathbf{n} = (0,0,1)^{\mathrm{T}}, \mathbf{O} = a \cdot (0.75, 0.5, 0.25)^{\mathrm{T}}, \mathbf{a} = (-1,0,0)^{\mathrm{T}}, R, \lambda = a) \\ H(\mathbf{n} = (0,1,0)^{\mathrm{T}}, \mathbf{O} = a \cdot (0.5, 0.25, 0.75)^{\mathrm{T}}, \mathbf{a} = (0,0,-1)^{\mathrm{T}}, R, \lambda = a) \\ H(\mathbf{n} = (1,0,0)^{\mathrm{T}}, \mathbf{O} = a \cdot (0.25, 0.75, 0.5)^{\mathrm{T}}, \mathbf{a} = (0,-1,0)^{\mathrm{T}}, R, \lambda = a) \end{array} \right\} \tag{3.17}$$

(in the notation introduced by eq. (3.16)), and inflated to have a circular (normal) cross-section with the desired wire radius r. Helix centre positions $\mathbf{O}$ and phase axes $\mathbf{a}$ are set in a way to match the crystallographic unit cell choice, analogue to 3.2 in section 3.3.1.[40]

Obviously, for wire radii allowing void pores, this creates a bi-continuous network, *i. e.* both void and material space are interconnected throughout the whole structure by construction.

Its topological equivalence to the single Gyroid has not been shown rigorously, but obviously shows up from comparison of the structures (suggested in figure 3.6.

The BCC-trihelical Gyroid

Once one has rebuilt the Cartesian 4_1 screw axes along ⟨100⟩ directions (three per unit cube: [100], [010] and [001]) from helices, forming the solid phase, one has arrived at simple cubic symmetry (originating, in effect, from applying the 3 rotation to rotate-produce the helices onto each other).

Even if the *topology* of this SC Gyroid is that of the **srs** network, the *geometry* can never be true BCC, due to the lack of the explicit duplication vector 1/2[111] (or, equivalently, the 3 axes in all the ⟨111⟩ directions, besides [111]), even though the resemblance works amazingly well already. However, full BCC symmetry can be achieved by explicit execution of the BCC basis duplication. For a side-by-side comparison of SC and BCC helices, see fig. A.4 on page 112.

Look at a point where the wire of a SC helix has wound up to direct into [110] direction from its orientation axis. By the half-pitch of phase distance between the two distinct primitive helix arrays (plugged into each other to form the BCC basis within the unitcube), the complementary helix is directed into $[\overline{11}0]$ direction, hence at the same place. Note that this implies

- the remarkable accuracy of building the (actual BCC, hence six equivalent axes per unit cube) Gyroid from the three-helices model: the second set of helices accounts only for minor structure smoothing and strictly satisfying BCC symmetry, but has no effect on topology (see fig. 3.6 on how the BCC-helical Gyroid looks like in this situation).

- a constraint fixing the helix radius by a simple touch consideration: In order not only for the direction, but also for the radial distance of the two helices to meet, the contact point, hence

---

[38] In fact, this holds also true for the 3_1 helices in the ⟨111⟩ directions, which are not considered at all in this study.

[39] Note that this is not the choice in [Was13], but is re-parametrised/translated to make the distance between centre points **O** of the helices of distinct orientations, and between adjacent unit cells maximal, and the parameters represented in a way to emphasise their inherent symmetry.

[40] This way, the primitive cubic 3 symmetry along [111] is obviously visible in the cyclic permutation of all helix coordinates.

the helix radius R has to be at half the axis distance (when seen from [001] direction), thus at $R/a = \sqrt{2}/4$

Volume filling fraction and translational noise

A (single-turn) helix can be seen as the result of cutting a torus (of elliptical cross section) and shearing along its polar axis. The short semiaxis equals the desired wire radius r, and the long semiaxis computes from the helix radius R and the pitch p (helix "wavelength", *i. e.* repetition length in normal direction) from elementary trigonometry to $r / \cos(\arctan(p/(2\pi R))) = r \cdot \sqrt{1 + p^2/(2\pi R)^2}$.

Let us, for shortness, introduce the $A = \pi r^2 \sqrt{1 + (p/(2\pi R))^2}$, the cross-section area if the helix is cut by a plane containing its axis. By applying Pappus' centroid theorem, the volume of a single-turn helix computes to

$$V_{\text{helix}} = A \cdot 2\pi R = 2\pi^2 r^2 R \cdot \sqrt{1 + \frac{p^2}{4\pi^2 R^2}} = \pi r^2 \cdot \sqrt{4\pi^2 R^2 + p^2} \quad . \tag{3.18}$$

This is, unsurprisingly, the volume of a cylinder of radius r and the un-wrapped length of the helix wire: the hypotenuse of the triangle whose legs are the pitch, and the diameter of the circular base projection of the bend, respectively.

The volumes of the distinct helices are far apart from being additive to yield the overall ϕ, as the overlapping (especially from the explicit BCC basis duplication) renders a major part of an individual helix "redundant" (already covered by another helix). A reasoning for computing ϕ, oversimplifying by reducing helices to a uniform "probability cloud", adopts ideas from the Boolean model:

Be $\overline{\phi_1} \in (0; V_{\text{box}})$ the probability to find no helix at a random place within a finite box, or, equivalently, the volume fraction of the box *not* occupied by a helix. Then

$$\begin{aligned}
\overline{\phi_1} &= 1 - \frac{V_{\text{helix}}}{V_{\text{box}}} = 1 - 2\pi \frac{RA}{V_{\text{box}}} \\
\text{For } n \text{ helices:} \quad \phi_n &= 1 - (1 - \overline{\phi_1})^n = 1 - \left(2\pi \frac{RA}{V_{\text{box}}}\right)^n = \\
&= \sum_{k=1}^{n} \left(\phi_k - \phi_{k-1}\right) \\
\phi_n - \phi_{n-1} &= \overline{\phi_1} \left(1 - \overline{\phi_1}\right)^{n-1}
\end{aligned} \tag{3.19}$$

Figure 3.7 denotes this sequence at its right border. Besides, results from voxel counting "experiments" on structure initialisations reflect the situation for a real BCC-helical Gyroid, depending on the displacement of the helices by a Gaussian-distributed offset of standard deviation σ_r/a. For large distortions (the relevant scale being the wire radius r), hitting the single-helix Boole limit is a mere consequence of the binary evaluation nature—the higher-order "predictions" are completely wrong, as the Boolean model is totally naïve with respect to the real-space correlations arising from the helices being solid bodies. At small/no distortion, the variances of seed statistics is small, and considerable multiple overlap is present, decaying fast on switching on the quasi-random distortion.

Note that the helical character of the building blocks survives any kind of distortion, while the sensitivity of ϕ on the distortion scale exceeds that of the other Gyroid models. The Helices are a mathematical "toy-model", probably badly suited for actual realisation. But they show a natural route to separate the geometrical features (helical elements in the network topology) in different directions, *cf.* sec. 5.3.1.

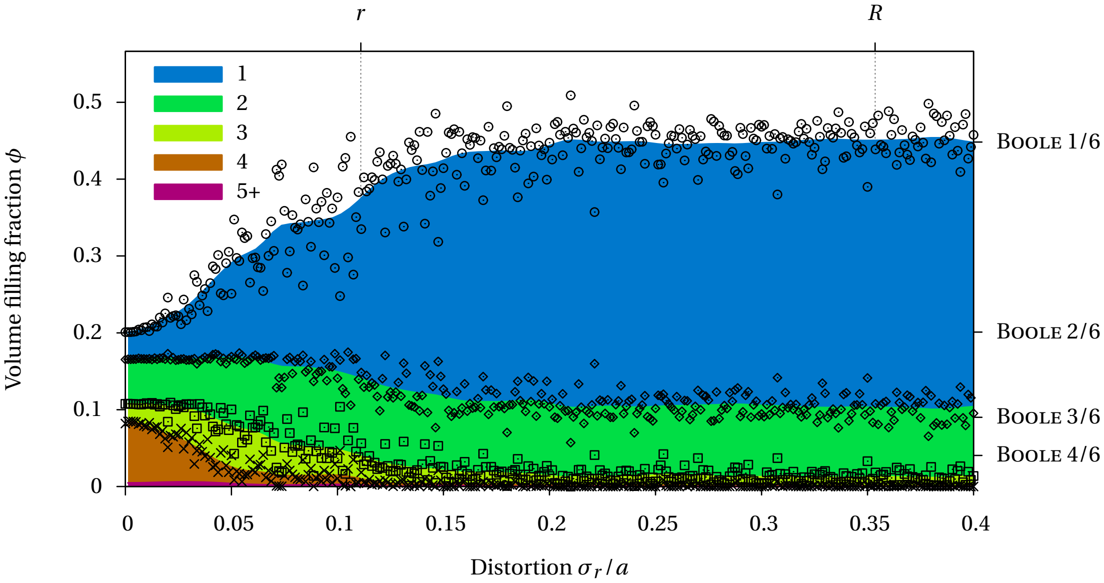

Figure 3.7.: (Voxel counting) Amounts of helix overlapping within the BCC-helical Gyroid (six helices per unit cube, helix radius $8^{-1/2}a$, wire radius 0.111 a, resolution 35 px a^{-1}) when subject to purely translational noise on the helix origins. Data points show the fraction of voxels covered by at least as many helices as noted. Data point noise is due to variable random seeds; solid areas are delimited by splines, as guides to the eye. On imposing distortion (Gaussian profile, $\sigma_q a/(2\pi) = 1$), the helices are moved apart each other from the positions forming the Helix Gyroid approximation. Multiple-overlap volumes decrease, whereas the binary ("net") volume filling fraction "1" rises ($\sigma_r/a \lesssim 0.1$). At higher distortions ($\sigma_r/a \gtrsim 0.2$), overlap fractions equilibrate, at a binary ϕ around 0.45, *i. e.* more than twice the original filling! To emphasise that, this plot does not apply a logarithmic scale for the ordinate.

Table 3.1.: "Standard" parameter choices for the different Gyroid initialisation models to obtain the volume filling fraction of $\phi = 20.5\,\%$, as motivated by its approximate occurrence in the wing scales of *C. rubi* [Sab+14]. For reflectance spectra and CCR in [001] direction, for typical biological contrast $\varepsilon = 2.4$, see in fig. 3.8.

	Nodal	**1srs** network	Helices	
			SC	BCC
Threshold	$t = -0.9$			
Wire radius	*n/a*	$r = 0.1372\,a$	$r = 0.1255\,a$	$r = 0.113\,a$
Helix radius	*n/a*	*n/a*	$R = a/\sqrt{8}$	
Prominent length scale		edge length/subdivisions	helix centre distances	
	(continuous)	$a/\sqrt{8}$	$(3/8 = 0.375)\,a$	$(8^{-1/2} = 0.354)\,a$
See sec./page	3.3.132	3.3.2/36	3.3.3/39	3.3.3/40

3.4. The undistorted single Gyroid as a PhC

The single Gyroid, arising from its natural occurrence in systems known for their structural colour (*cf.* introduction), has been subject to investigation as a structure-photonic crystal [**TODO**; MDS09; Dol+14; Sab+11; Sab+14]. See table 3.1 for which parameters to apply to get appropriate ϕ from the different Gyroid models. This section will, in short terms, present the known behaviour, with a focus of band structure features/inclination in high-symmetry (low MILLER-indexed) directions.

All data within this section (for the introduction of methods, see chapter 4) has been extracted from simulation at dielectric contrast $\varepsilon = 2.4$ (biological material/chitin vs. air/vacuum), with typical filling fractions ϕ known from butterfly wing scales, and at frequencies equivalent to optical/near-UV light, when the cubic lattice constant a is of the typical order of 315 nm of butterfly wing scales [Sch+11; MTC13].

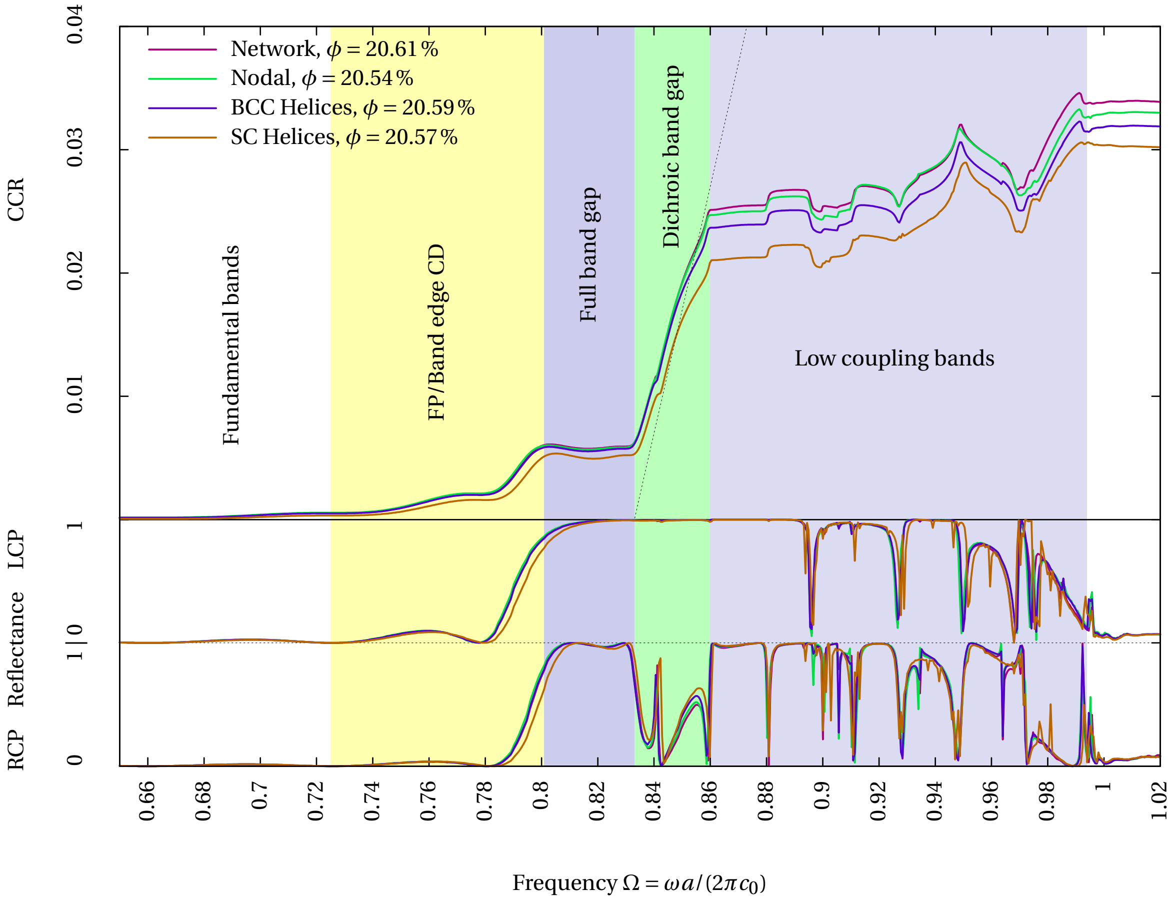

Figure 3.8.: (MEEP reflectance) Comparing the undistorted single Gyroid initialisations by their PhC response of [001] inclined slabs of the thickness 6 a. LCP (middle graph) and RCP (lower) reflectance; above, the cumulative circular contrast. Shadings demarcate regions of qualitatively distinct regions, as identified along the description of band structure and reflectance (sec. 3.4 and [Sab+14])

Briefly summarised, itemised by inclination/high-symmetry direction:

Cartesian [001] direction (See also fig. 3.8) Subsequent to the fundamental bands, at $\Omega \gtrsim 0.8$, a narrow (partial) high-reflectance band gap causes high reflectance, irrespective of circular polarisation.

Around $0.83 < \Omega < 0.86$, a circular-dichroic band gap exists due to the existence of a band consisting of modes of nearly full ↺↺ character, giving rise to high transmission, hence substantial CD.

At higher frequencies, multiple bands exist which couple poorly to incident plane waves, thus showing high reflectance in general.

Cubic face diagonal [110] This is the primitive direction of reciprocal lattice, hence the direction within the BZ of least distance to BZ translation copies. For a given low frequency (*i. e.*, not exceeding the eigenfrequencies of the primitive modes at the band edge in the primitive direction too much), within the material no other BLOCH modes are available to couple into with help of additional crystal impulse (reciprocal lattice vector), so that, in effect, the diffraction problem remains one-dimensional, giving rise to a BRAGG mirror-like, simple band gap and reflectance behaviour, insensitive on circular polarisation [Sab+14].

Body-diagonal [111] The band structure in [111] direction is complicated by the long distance up to the next Γ (reciprocal lattice) point, forcing to view the direction in the extended zone scheme (regard wavevectors effectively outside the first BZ) [Sab+14]. First-BZ-only band structures show up several narrow, essentially achiral band gaps, but extended view unveils low-coupling modes over the whole frequency range. Note that this direction, being the primitive real-space direction of the BCC lattice, hosts the highest number of repetition units per given length. Thus, in resemblance/reversal of the [110] argument, the frequencies necessary to reach the BZ edge are sufficient high to excite sufficiently many higher diffraction orders to achieve major transmission (or, equivalently, to hinder the build-up of a wide band gap).

Figure 3.8 compares the reflectances and CCR performance of undistorted single Gyroids created by either the nodal approximation, the network graph, the BCC or the SC helix sets (as described in sec. 3.3). The former three share exact BCC symmetry, hence qualitatively (in frequency position and slope) the same details in reflectance, and deviations are solely due to the minute differences of how the initialisations differ in detail (straight vs. curved “wires” for network vs. helix Gyroid, *e. g.*). The agreement is remarkable.

The SC helix behaviour, behaving in terms of CCR (which smoothens out narrow details by its integration) rather similar to the BCC structures, exhibits subtle, but pronounced deviations from the BCC reflectance spectra in sharp resonances. Moreover, although the volume filling fraction is essentially unaltered, the CCR always lies below the true BCC structures, and a blue-shift of about $\Delta\Omega = +0.02$ is visible. This may hint at a high importance of fulfilling the geometrically strict BCC symmetry.

3.5. Finite incident angles

By applying true BLOCH-periodic boundaries, setting $\mathbf{k}_\parallel$ as an input parameter, and a spatial modulation of the source profile with the same BLOCH phase factor $\exp(\imath \mathbf{k} \cdot \mathbf{r})$, a FDTD simulation can be carried out at *finite incident angle* with respect to the inclination direction/slab surface normal.

More precisely, this is a simulation run at constant $\mathbf{k}_\parallel$, with the actual incident angle being dependent on the frequency Ω, determining the normal component k_z of the incident wavevector: The polar angle computes, per frequency, to $\vartheta = \arctan(c_0 k_\parallel / \omega)$ and is a nonlinear function of both $k_\parallel$ and ω One "finite-angle" simulation run carries the finite-width frequency spectrum of the source, so the lines of constant angle lie curved within the graphs parametrised by $(\Omega, k_\parallel)$. An additional degree of freedom comes with the azimuthal angle of the wavevector (lateral direction of $\mathbf{k}_\parallel$), chosen (and named adopting the directions) to tilt towards other high-symmetry directions.

Figure 3.9 depicts, starting from the high-symmetry directions [111] (upper row) and [001] (lower row), the angle dependence of circular contrast in an undistorted Gyroid.[41] Similar angle-resolved data (both from simulations and experiments) has been obtained by Pouya [Pou12] and Pouya and Vukusic [PV12] for single Gyroid reflectance of *linearly* polarised light, and used to identify the Bragg orders involved in the formation of the reflexes.

The prominent reflectance signal of the band gap/low-coupling regime of the [001] direction systematically red-shifts with increasing parallel wavevector. Whereas the low-coupling regime and the dichroic band gap (blue) gradually diminish, the full band gap reflectance stays rather robust, even at incident angles on the order of 25°.

The [111] direction, "outstanding" by its complicated band structure and both low absolute and dichroic reflectance, shows up very sensitive to finite incident angles, and its minute ↻↺-dominated yet faint reflectance is, depending on tilt direction, outshined by a moderate increase in reflectance (with signals at least as complicated); some of the emerging "bands" exhibit distinct CD (intense colours) in both ↺↺ and ↻↺ CP senses. Compare this complicated behaviour with the observation made for the normal-incidence [111] direction data in the presence of finite absorption, sec. 5.4.2.

Its distinctly low reflectance becomes overlaid with medium-reflectance "bands", exhibiting weak ↺↺-major reflection, impeding possible experimental observations of the features in [111] direction when subject to (inevitable) finite angular divergence.

---

[41] Compare fig. 3.9 with fig. 5.17 on page 103 for the influence of translational noise and a sinusoidal chirp in the [001] direction.

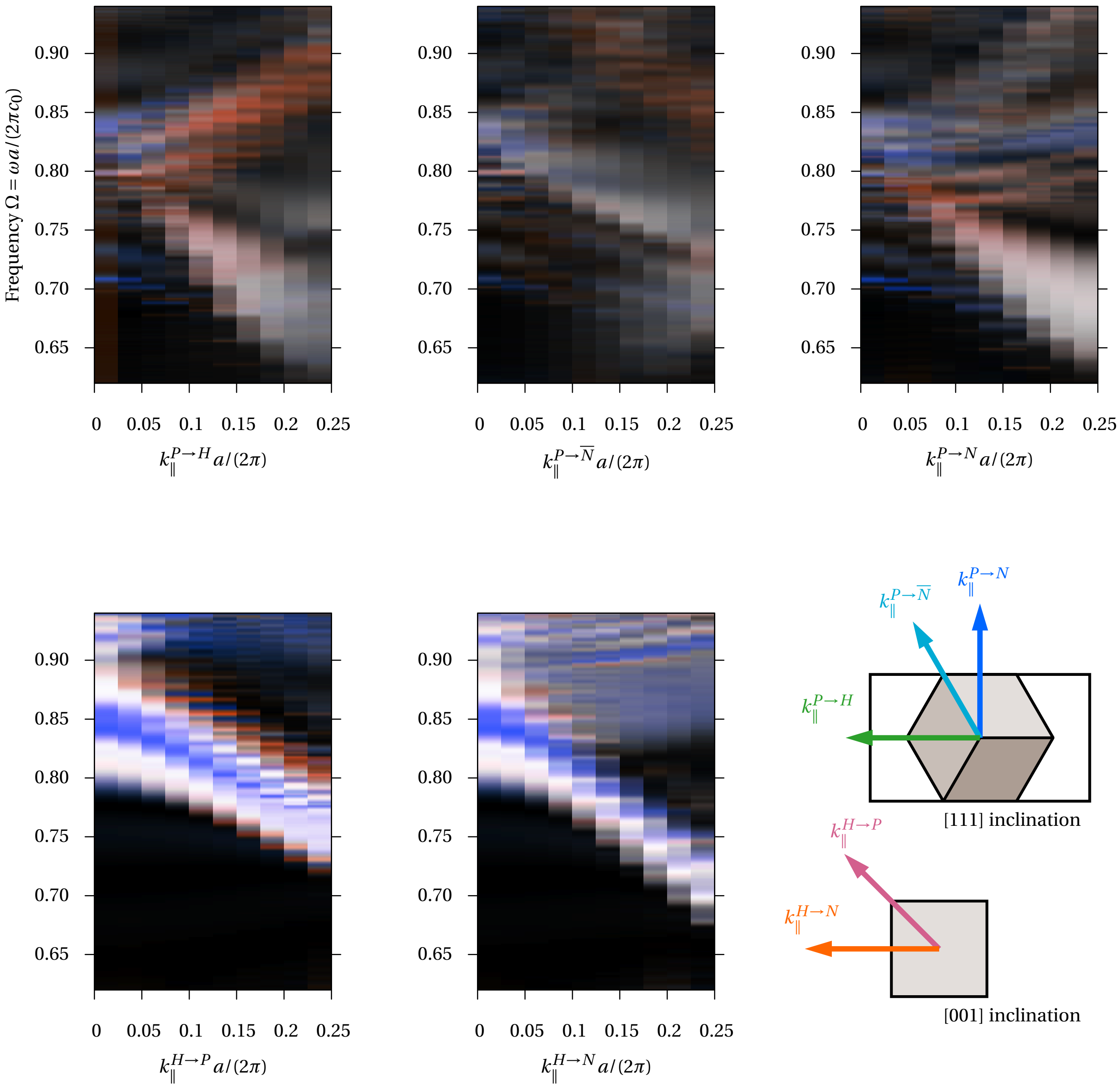

Figure 3.9.: (MEEP reflectance) Irradiation with finite $k_\parallel$ (in effect: tilting the angle of incidence) of the undistorted network single Gyroid ($\phi = 20.5\,\%$, $\varepsilon = 2.4$), inclined in [111] direction (upper row) and [001] (lower row) and its consequences on reflectance. The polar angles cover a range from zero to approx. 25° in these pictures. The azimuthal angles are chosen (see real-space lattice drawing at the lower right) to mix the **k** vector from the surface normal (inclination) with some amount of another high-symmetry direction, denoted by indexing $k_\parallel$ with the respective directions. Brightness is proportional to reflectance (black: zero, white: full reflectance for both ↺ and ↻). Colour intensity depicts degree of circular polarisation (red: ↻-major, blue: ↺-major reflectance).

4

Constructing Distorted Structures and Probing by FDTD

Adolph von Menzel: „Eisenwalzwerk“ (1875)

4.1. Computational Electrodynamics

The usual way for testing results from theoretical predictions or from experiments against each other, when the "direct" cross-link is inaccessible, is the substitution of generalising exactness—with minimal approximations (esp., discretisations)—by brute-force computing power: numerical simulations. Once the (small) subspace of analytically solvable problems has been fully explored, numerical approximations to the governing equations have to be applied to compute (approximations of the) solutions.

For the field of electrodynamics (*i. e.*, approximate dealing with the MAXWELL equations), several numeric methods come to use, each with its distinct approaches [Oba11]:

Time-domain Forward-integration on discrete meshes. FDTD (finite-differences time-domain), FEM (finite elements), FVTD (finite volumes). In essence these differ in the approach to subdivide space.

Frequency domain/indirect Plane-wave expansion and relatives: seek for the mode structures and their associated eigenfrequencies (*cf.* sec. 2.3.1).

4.1.1. Finite Differences Time-Domain (FDTD)

The both most naïve and straightforward approximation to numerically compute electrodynamics is to replace the real-space time-domain MAXWELL equations' differential operators (spatial and temporal derivatives) by their respective first-order *finite differences*, partitioning space and time in a suitable uniform lattice, and simple iterative computation of time-evolution (hence the name).

Regular spatial discretisation—the Yee lattice

Yee [Yee66] pioneered the FDTD calculations, deploying the now-standard YEE lattice space-time tessellation (in two-dimensional space): The space is divided into voxels[42], *i. e.* a simple cubic (in 3D; square in 2D) lattice of distinct sites. At any of those lattice points, the six **E** and **H** field components are stored component-wise on different positions within the voxel, so that they form a spatial chessboard-like pattern, further structured by the pattern which components are stored at which sites: The YEE lattice storage sites hold the triple of H and E components placed at each site of an imaginary *fcc* lattice (without the origin itself) originating from the body centre, or an edge centre, respectively.[43] For a closer look to the details, see [Yee66] or any basic FDTD text [TH05; Oba11; MIT].

FDTD, as a *time-domain* technique, applies a temporal update scheme. It is designed in a *leap-frog* manner, in that the $\mathbf{H}(t)$ components are computed from $\mathbf{E}(t-\Delta t/2)$ half a time step earlier, and from this, the $\mathbf{E}(t+\Delta t/2)$ values, to compute the fields (not only in space, but also in time) alternately, rather than simultaneously. For computing field quantities from both the electric and the magnetic fields, this implies that the accuracy is disturbed by the time-offset of $\Delta t/2$, giving rise to a field synchronisation routine, which interpolates in time, enabling a more accurate calculation of those derived quantities [MIT].

---

[42] As this study will cover 3D only, I will use the term *voxel* ("volume pixel") throughout the document. Though, I will denote linear dimensions in terms of the (YEE) lattice given in "pixels" (px) in accordance to ordinary 2D computer graphics.

[43] You can also think of the YEE lattice storage as a "rocksalt – *bcc*" structure, *i. e.* the two-atom (E and H) basis *fcc* rocksalt structure with the unit cube origin and body centre (*bcc* lattice) cleared out.

Bloch-periodic boundaries

In an infinite system with discrete translational symmetry, the value of any function at any point can be determined once its decomposition into a unit cell function (invariant under lattice translations), parametrised by its respective crystal wavevector **k**, is know (which is the main message of the BLOCH theorem, see sec. 2.3.1).

For an incoming field consisting of plane waves, a laterally infinite structure (periodic or not) would be appropriate, but is—of course—not realisable with both finite spatial resolution and finite computer memory. For crystals (true translational symmetry), the natural way to "truncate" the structure is by (parallel) planes commensurate with the crystal lattice (apart a lattice vector **R**), and to impose *periodic* boundary conditions: The opposing planes are connected, so the system at one side sees itself on the other as its neighbourhood (toroidal connection), periodically concealing the translation by **R**. To make (complex) fields fulfil the BLOCH condition for a given **k**, the phase factor $\exp(\imath\mathbf{k}\cdot\mathbf{R})$ is added on the interaction terms involving each lattice vector **R** which collapses parallel box termination planes onto each other.

These BLOCH-periodic boundaries are the essential (implicit) ingredient in calculations of crystal band structures by plane wave expansion [AM76; JJ01]. In the case of the slab-like transmission/reflectance geometry, the preconditions are slightly altered: Of the three spatial dimensions, only the two *lateral* are indefinitely extended.[44] Thus, periodic boundaries are used only for the lateral faces of the simulation box. Note that the finite lateral extent is a compromise towards disorder systems (*i. e.* an with infinite spatial period).

By constructing distortion with the help of Fourier components of the simulation box (see sec. 4.3.1), periodic boundaries for the structure are automatically fulfilled. For the electromagnetic fields, MEEP provides passing a BLOCH wavevector to define the phase increment at boundary crossings.

Unless non-normal incidence, *i. e.* finite $\mathbf{k}_\parallel$, is requested, this reduces to $\mathbf{k} = 0$ (unity phase factor, *i. e.* ordinary periodic boundaries) in effect, as the normal component of the wavevector is arbitrary (due to absorbing boundary conditions described in the next section). When a non-zero incident angle ϑ is desired, the lateral component $k_\parallel$ of the BLOCH wavevector is adjusted to direct into the incident angle $\vartheta = \arctan(ck_\parallel/\omega)$ direction. In fact, $k_\parallel$ is the given input variable; so the angle is dependent on the frequency, as a whole interval of ω is excited by the source. This "parametrisation" of incident angles by $k_\parallel$ is somewhat more "natural" than the angle itself, as it mimics the conservation of parallel components of the wavevector as well as those of the **E** and **H** fields on crossing material borders—at the price of issues on data analysis, *e. g.* in "distorted" spectra when plotted against ϑ, or due to its distance to realistic experimental conditions.

Reflection-less boundary conditions: (U)PML

For situations where a sensible emulation of infinite free space is desired, a way is needed to suppress reflections in such a way that the actual conditions are (ideally) irrelevant. To reach this goal, the naïve placing of a simple absorbing material at the boundaries has the disadvantage of, in general, causing reflections at the interface. Therefore, Bérenger [Bér94] developed the *perfectly matching layers* (abbreviated: PML; "matching", as it is designed to match the wave impedance of free space) as an artificial medium placed in front of the borders of the simulation box boundaries. Its idea is that, by constructing, plane waves are reflection-less transmitted, and exponentially attenuated. PML have

---

[44] In the direction of the surface *normal*, however, the (material) thickness is fixed, surrounded by hollow space to allow for an onset of far-field behaviour (allow evanescent modes to decay). See next paragraph.

rapidly gained attention as boundary conditions for time-domain simulations [TH05], and have been improved in various ways, especially into the nowadays widespread *UPML*: coordinate transformation towards complex coordinates [Joh10; OJ11; Osk+08].

A failure of PMLs witnessed during this work, and also known from literature [DV11; Osk+08; Dom13] is a *divergence* (exponential grow of field amplitude), especially for non-normal incidence, or PhC reaching near or into PMLs. Long-lived lateral modes within the simulation box void might get excited (during the initial source pulse) which are badly absorbed by PMLs, or even “pumped” by them. The field gets dominated by its exponential growth, rendering simulation data unusable. By the choice of the POYNTING vector z component (see page 53), PML divergences could be effectively prevented in the present study.

Adiabatic absorbing boundary conditions [Osk+08] have been proposed as an alternative to classical PMLs, and have been implemented in MEEP as a PML drop-in replacement. Testing within the framework of this study resulted in no significant advantage over PMLs.

Convergence, Stability

Due to the conceptual simplicity of finite-difference methods for solving initial value problems, convergence has been subject to analysis long before the emergence of electronic computational methods as FDTD: Courant, Friedrichs, and Lewy [CFL28] have shown an interrelation between the spatial and temporal derivative discretisations, nowadays named the COURANT factor S [MIT; Oba11]

$$\begin{gathered}\frac{S}{c\Delta t} = \frac{Sn}{c_0\Delta t} \leq \sqrt{\sum_{j=1}^{d} \frac{1}{\Delta x_j^2}} \quad \left[= \frac{\sqrt{d}}{\Delta x} \text{for } \Delta x_j \equiv \Delta x \;\forall \text{ spatial dimensions } j \right] \\ S \leq \frac{n_{\min}}{\sqrt{d}}\end{gathered} \tag{4.1}$$

It assures maximum quadratic convergence [MIT]

Strengths and Weaknesses FDTD can easily be adopted to arbitrary problems; the uniformity of mathematical structure leads to low implementation complexity. With respect to frequency-domain techniques, FDTD usually applies wide-band input pulses, enabling simultaneous data acquisition from near-arbitrarily many[45] distinct frequency channels (as long as linearity, *i. e.* strict validity of superposition is assumed).

At the downside of FDTD, the numerical cost weighs heavy: Especially when very different length scales should be represented accurately, the missing option to adapt resolution to structure details obligates a lot of computational work in “boring” (homogeneous) regions of the simulation box.

Another intrinsic drawback of FDTD is *numerical dispersion*: phase velocities become dependent of the orientation relative to the YEE lattice when the space and time discretisation meshes are finite [Oba11].Within to studies excluding examination of time-dependent behaviour, this phenomenon can be safely disregarded, as only the total energy/flux balance is taken into account.

---

[45] The NYQUIST frequency of the YEE lattice $\Omega_\text{N} = \omega_\text{N} a/(2\pi c_0) = a/\text{Resolution}$ defines the magnitude of the natural upper limit of frequency sampling, the lower limit given by the inverse of the time desired to wait for the simulation to finish.

4.1.2. MEEP

The software coming to use for the FDTD simulations of this thesis is *MIT Electromagnetic Equation Propagation*[46] (MEEP) [Osk+10]. By the usage of advanced methods for anisotropic sub-pixel averaging [Far+06; OKJ09], the staircasing effects inevitable on voxelised smooth surfaces get minimised, in effect attaining quadratic convergence for any surface geometry [Far+06].

MEEP is most comfortably operated by its Scheme interface, implementing various useful standard functionality of FDTD software, and offering (in principle) easy extendability. However, the sophisticated route for material function design necessary for this work cannot be "straight-forward" integrated in MEEP's standard work flow (fine-grained "voxel-wise" control of ε conflicts with the "illusion of continuity" [MIT], which otherwise does a great job in keeping users to be distracted from numerical details). So an extensive amount of work had to be accomplished, for the structure construction software dedicated to this thesis, to properly cooperate with MEEP.

4.2. Reflectance of PhC via FDTD

4.2.1. Designing the simulation box

The simulation box geometry

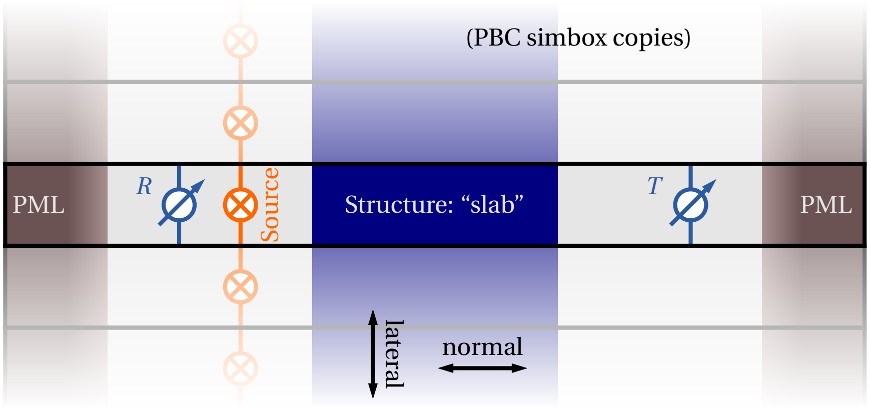

Figure 4.1.: 2-D Sketch (by scale for a system size of 2 × 2 × 6 unitcells) of the simulation box for FDTD simulation with MEEP Geometry, with the PhC material within the slab, surrounded by hollow space. Simulation area boundaries in normal directions are terminated by PML absorbers, and laterally quasi-infinite, from continuation by (Bloch-)periodic boundary conditions, which duplicates the source, too. Reflectance and transmission measurement planes are indicated by R and T.

This section gives a short overview over the FDTD simulation box, depicted in fig. 4.1. By convention, the normals of the slab surfaces, sources, measurement planes, and PML direct in z direction.

---

[46] `http://ab-initio.mit.edu/wiki/index.php/Meep`

Boundary conditions

Periodic Boundary Conditions On the lateral faces of the simulation box, the fields are subject to Bloch boundaries, as introduced in sec. 4.1.1. For $\mathbf{k} = 0$ (or, more concisely, $\mathbf{k}_\parallel = 0$), they reduce to the special case of regular periodic boundaries, like the ones holding implicitly for the material function $\varepsilon(\mathbf{r})$.

Reflection-less boundary conditions: (U)PML In the *normal* direction, space should ideally behave as if it were infinite vacuum, *i. e.* no effect of boundaries should be visible at all. This is achieved by Uniaxial PML layers, as introduced in sec. 4.1.1. Their thickness is chosen by a trade-off between simulation effort (PML volume accounts to the simulation box) and the achievement of full absorption while reflection-less. From experience, a PML thickness of 50 px (at light wavelengths of 20 px and above) proves robust; considerably thinner PMLs may exhibit finite transmission, or even trigger *PML divergence*, an exponential growing of field energy, due to the PMLs effectively acting as a negative absorption, *i. e.* gain medium.

Since PMLs are optimised for absorbing light of *normal* incidence, their absorbing performance falls behind for non-normal incidence. Especially, the zero-reflectance condition is no longer fulfilled when PMLs are superposing inhomogeneous structures [Osk+08].

Special care must be taken to not locate flux/decay measurement, or photonic crystal material too near to PMLs, as the evanescent mode patterns leaking some Yee lattice points outwards may adulterate data, or give rise to inferior field decay, or PML divergences.

Light sources

Circularly polarised light is created within MEEP by the inversion of basis change from circular to linear polarised light as described within sec. 2.2.1: MEEP offers sources for linear polarised light, and two sources with same geometry are superimposed at the same place. The first source creates the x component of the electric field, the second the y component, with its phase advanced by $\pi/2$ for LCP, or $3\pi/2$ for RCP light (which will, relative to the right-handed choice of the Gyroid enantiomer sense (*cf.* sec 3.2.2), be labelled LCP=↻↺, and RCP=↺↺ in the following).

The temporal envelope of source emission in FDTD simulations is typically Gaussian-shaped [Oba11; MIT]. Therefore, the amplitude spectrum in frequency space is also Gaussian, and in both the time and frequency domain the function runs maximum smoothly.[47] The response of several such frequency pulses may be combined to increase the effective band-width.

Measuring the fluxes

The data acquisition takes place by *flux planes*, geometrical objects (source- and surface-parallel planes) collecting the Poynting flux through themselves [MIT]. Time-domain data will be internally Fourier-transformed to yield frequency-resolved intensity data. The frequency range is naturally in congruence with the input spectrum of the Gaussian source, and the selected number of frequency bins defines the resolution.

---

[47] In detail, this is not perfectly true, as the Gaussian pulse has to be cut off at some point in time. Such a sudden (though low-amplitude) gives rise to high-frequency noise causing Yee lattice aliasing artefacts [Oba11]. Thus, FDTD software offers and recommends long Gaussian cut-off times [MIT]. As the time constant of mode decay from the PhC typically exceeds the pulse width by orders of magnitude, this is a “cheap” way to reduce slowly decaying high-frequency noise within the FDTD simulation box.

Measuring reflectance flux is complicated by the fact the primary source contributions get measured along the reflected light. Therefore, any “real” measurement is preceded by a “reference” run *without* the structure (or, equivalently, with $\varepsilon = 1$ at all space points), so that the free space signal of the source can be collected for subsequent subtraction from the reflection flux *with* the structure. Moreover, the reference simulation run creates intensity reference data of the source spectrum, against which the flux data can be *normalised*, *i. e.* reduced to unity.

4.2.2. Determination and analysis of simulation “convergence”

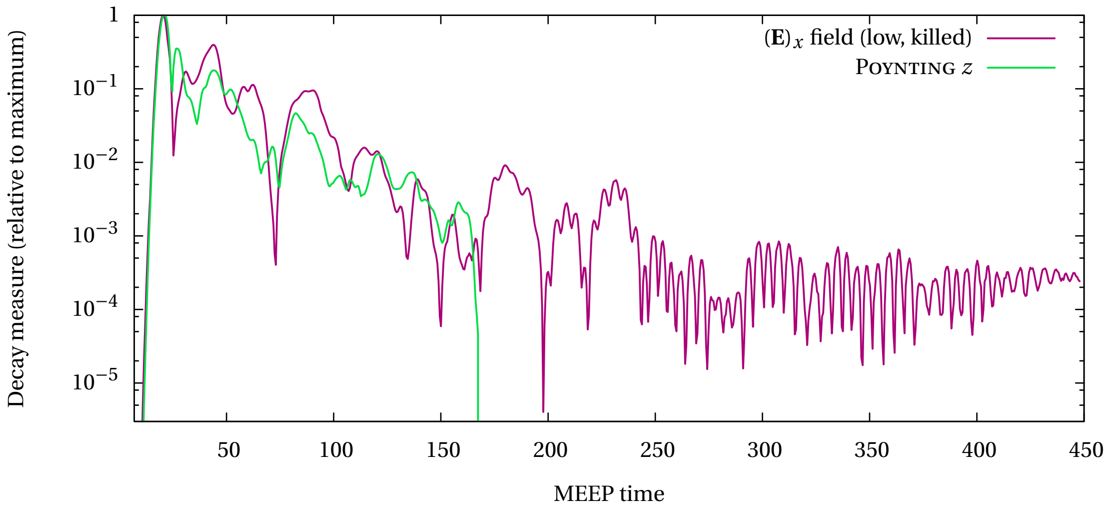

Figure 4.2.: (MEEP time-domain) Field decay monitors (at the transmittance flux plane centre) of either the x component of the electric field, or the z component of the Poynting vector of energy flux. Geometry: SC Gyroid distorted with $\sigma_r / a = 0.2$, $\phi = 0.271\,66$, thickness 5.7 a, ↻↺ irradiation. Simulation by **E** field decay measure killed due to onset of PML divergence (time $\gtrsim 400$).

As for any numerical forward-integration technique, also FDTD needs a stop criterion. The temporally bounded field excitation (Gaussian source amplitude envelope) suggests measuring *field decay*, *i. e.* the observation of field strengths (“decay measures”) at some given point(s), until the assumption that most of the energy imposed by the sources has radiated into the PMLs for subsequent absorption holds sufficiently plausible. Technically, the ratio between the current field measure and its maximum value over the simulation, has to lie below a given *cut-off threshold* for a sufficiently long time.

Watching (the absolute value of) a field component over its time evolution (as proposed by the MEEP tutorial [MIT]) exhibits major oscillatory behaviour, thus proves susceptible to zero passages, causing premature “convergence”. Figure 4.2 depicts such a *pathogenic* case, where field decay (x component of the electric field) would have “falsely” terminated the simulation if the cut-off were higher, and finally a creeping PML divergence takes over (until the run was terminated by hand).

As a more robust measure, the z component of the Poynting vector comes to use, driven by the following considerations:

- Measuring flux is, by also introducing the magnetic field components, less susceptible to zeros, prematurely terminating the simulation.

- Instead of a scalar (energy density, *e. g.*), a vector has direction information, making it possible to detect tendencies to PML divergences:

- If PMLs start emitting, by what reason ever, radiation of intensity comparable to the initial source pulse field, or numerical errors accumulate in a similar fashion, the radiation will be directed from the PMLs to the PhC slab, thus will switch the sign of the Poynting vector at the location of flux measurement. So the onset of divergence will terminate the simulation by itself (see fig. 4.2). One drawback of this method is, that this "automatic" mechanism will cause early termination in cases of low overall-transmission, leading to intense residual ripple.

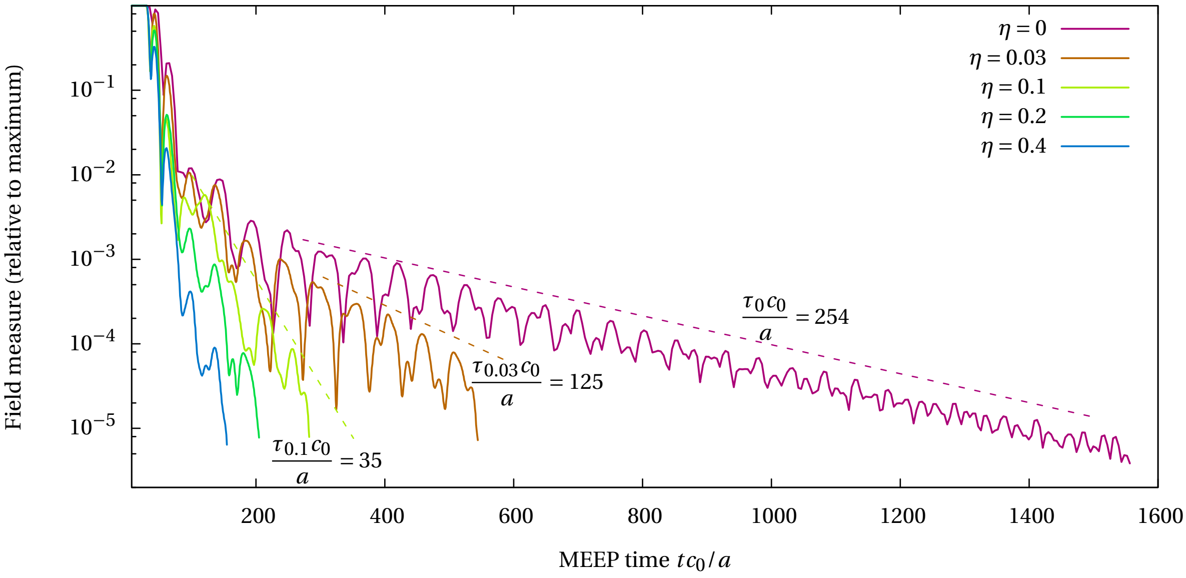

Figure 4.3.: (MEEP time-domain) Decay measure monitors diminishing field intensity (nodal Gyroid, $t = -0.9$, ↺↻ irradiation). After transient response ($tc_0/a \lesssim 50$), decay behaviour gradually crosses over to exponential decay ($tc_0/a \gtrsim 200$). Switching on Lorentzian absorbance (increasing η, as described in sec. 5.4) shortens the time constant τ_η of exponential decay. Data acquisition from [Sab+14].

Absorption and field decay

It is natural to ask for the influence of absorption on the time constants. Figure 4.3 depicts the field measure in its time evolution. The exponential decay envelopes show up the anticipated response to losses, in a substantially more rapid decay.

It may be noted that, even though absorption could be considered to "speed up" FDTD convergence, this means either a substantial alteration of the system behaviour (*cf.* sec. 5.4), or (for $\eta \ll 1$) not a that substantial advantage.

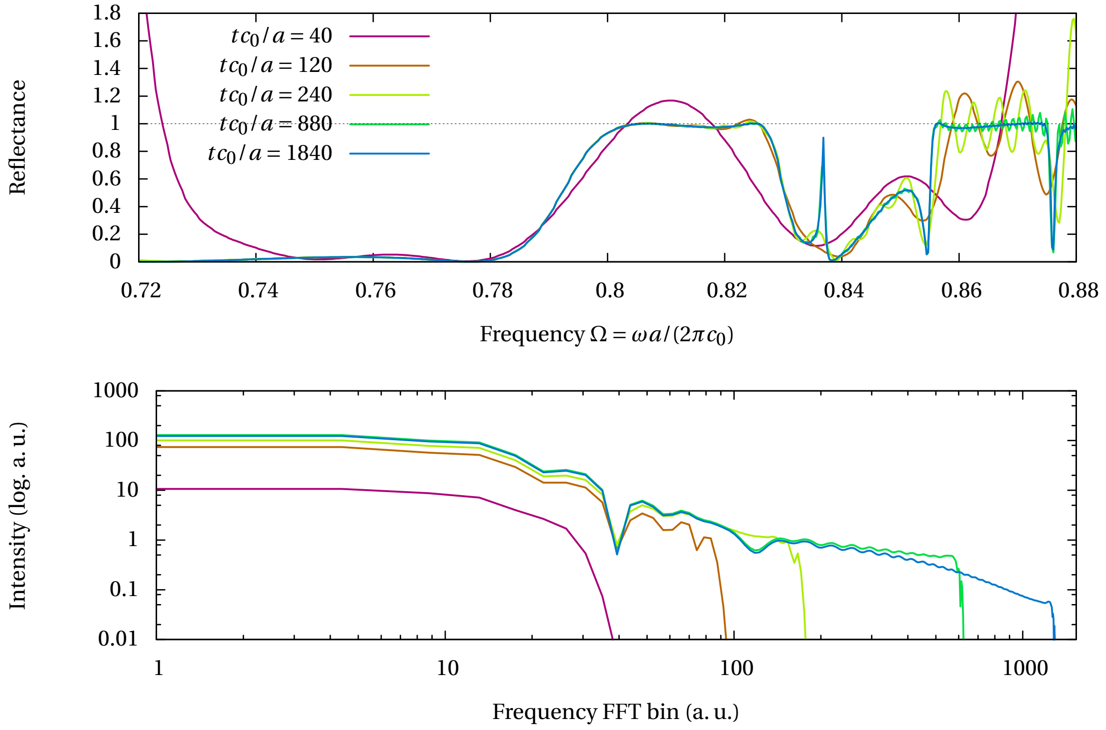

Figure 4.4.: (MEEP reflectance) Intermediate ⟲ reflectance spectrum output while the simulation is running. Ripples in frequency-space spectra (upper graph) increase in frequency and decrease in amplitude during the simulation time tc_0/a. Lower graph: Fourier transform of the spectra in the upper graphs: The maximum ripple frequency gets visible by a sharp signal break-down.

Development of spectra along simulation time

Flux planes accumulate the flux information during the whole simulation, and are capable of computing the "current" spectrum not only at the very end of the simulation. So we may have a look on how the "convergence" proceeds: by outputting intermediate spectra during the simulation. This is shown in the upper part of figure 4.4. Clearly, the "$R \overset{!}{<} 1$ energy conservation" is "violated"; especially at early times and at the edges of the frequency interval[48]. However, during the ongoing simulation, these overshoots level out gradually.

The ripples in the signals of figure 4.4 increase in frequency with progressing simulation time. The lower graph visualises this observation, in form of the abrupt cut-off frequency frequency shifting higher with time. To explain this behaviour, it is necessary to look how MEEP computes the fluxes frequency-wise: each flux plane continuously collects (POYNTING) field amplitude information in the time-domain, and computes, by numerical Fourier transformation, the frequencies from it. When the frequency data is "prematurely" requested (field amplitudes too high to be safely ignored), the time-domain cut-off introduces a jump function in the (periodically continued) time signal. Once

---

[48] Note that this data is reduced, *i. e.* divided by the reference run spectrum, and the numeric values at the tails come from division of two very small numbers.

subject to FFT to yield the spectrum, the latter is superimposed, essentially, with the harmonics of the simulation time window. The natural countermeasure is to wait until the field has sufficiently decayed to make its cut-off noise either negligible, or exceed the frequency resolution of the flux plane.

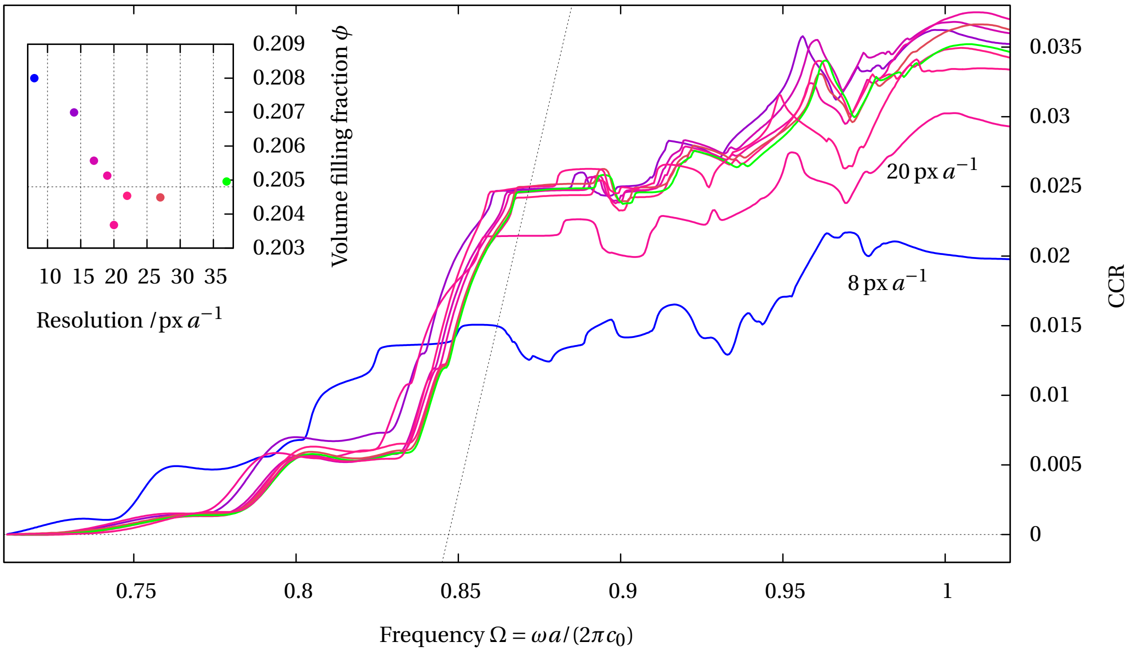

Figure 4.5.: (MEEP reflectance) How the lattice resolution impacts FDTD results: Cumulative circular contrast of the same nodal Gyroid (see sec. 3.3.1, $t = -0.9$, $\phi = 20.480\,\%$ analytically (dashed line in the inset, from eq. (3.15))) initialisation with different discretisation resolutions. At some resolutions, the reflectance spectra (and volume fractions) differ qualitatively and quantitatively from the general trend.

Grid resolution

The resolution of grid discretisation has to be traded off realised between a reasonable representation of the structure with all major details, and on the other hand the finite computational power (CPU time for FDTD iterations, and, perhaps, memory consumption for holding the lattice, for very large systems) and the demands on data quality.

To test for an optimal grid resolution, several runs of an otherwise identical structure have been carried out, differing in discretisation resolution. This comparison is presented in fig. 4.5 in terms of CCR data. It is no wonder that deviations from the main trend become marked at very low resolutions—alone, the survival of qualitative behaviour is remarkable (at EUCLIDean distances between network vertices of length $\sqrt{8}$px, and wire diameters of 2.16 px!).

In contrast, at some intermediate resolutions, *e. g.* 20 px a^{-1}, data markedly deviates from the otherwise common behaviour (Note that this effect may not be due to a simple *aliasing* artefact, as the nodal approximation completely consists of curved surfaces). This calls for the necessity of, once you simulate on a new system, to go through a multi-resolution scan like the one in fig. 4.5 in order to estimate the "average-ness" of single-resolution data from a more exposed viewpoint.

4.2.3. Inclination and Orthorhombic unitcell supersets

When the structure initialisations, as discussed in chapter 3 are realised within a simulation, we do not want to be restricted to their natural (*i. e.* Cartesian) coordinate orientation. Rather, an *inclination* should be selectable, in order to specify the relative orientation of the light wavevectors' parallel component $\mathbf{k}_\parallel$ with respect to

- (in the *crystalline* case) the band structure, *i. e.* determining the frequency-matching condition in the reciprocal space of the crystal, or
- given a system exhibiting any kind of directional order (be it inherited from a formerly crystallinity, or orientational order superimposing an otherwise spatial random structure), its predominant direction.

This work (and the underlying software) formally restricts to processing "orthonormal"[49] coordinate systems, partly to adapt to the rectangular "voxel" structure natural to the YEE lattice, see sec. 4.1.1.

Following the notation for plane cuts through PhC in literature [Sab+11], the inclination is the conventional cubic MILLER index $[hk\ell]$ of the surface normal, *i. e.* at normal incidence ($\mathbf{k}_\parallel = 0$), the incoming plane waves are directed in $[hk\ell]$ direction within a fictional continuation of the cubic (real and reciprocal) lattice from the material into the surrounding free space.

Orthorhombic unitcell supersets For the embedding of non-$\langle 00\ell \rangle$ inclinations (*i. e.* with not all crystal coordinate axes coinciding with the simulation box coordinate system) into the simulation box, we cut out, from a crystal chunk of sufficient size, a rectangular box with faces parallel or perpendicular to the desired inclination. For an arbitrary inclination, the minimal box chosen to hold commensurability with the crystal lattice this way is not cubic nor a square cuboid, but a general rectangular cuboid. This unitcell superset[50] must hold an integer number of primitive unit cells to be a valid crystallographic unit cell, and exhibits at least *orthorhombic* symmetry. It can be used as a convenient container for the construction of the structure by simple translational copy along the normal (= inclination) and lateral directions.

By convention, the slab surface normal, hence the inclination, will direct into z direction of the simulation box, *i. e.* the (conventional) orthorhombic supercell will be oriented such that its [001] axis coincides with the inclination direction.

Non-Cartesian inclination To fill such a orthorhombic unit cell with a cubic structure, the cubes have to be rotated to get the inclination $[hk\ell]$ the new z axis, hence the orthorhombic [001] direction.

The first step is a rotation around the axis $\mathbf{n}$ in between the normal and the inclination direction:

$$\mathbf{n} \propto [001] + \frac{[hk\ell]}{L_z} \tag{4.2}$$

(with $L_z = |[hk\ell]|$ the axial lattice constant of the orthorhombic cell), by an angle of π.Through this, $[hk\ell] \equiv \mathbf{z}'$ and z (the former cubic [001]) will swap places.

---

[49] The [conventional] unit cells are cubes, but without demanding a cubic space group, *i. e.* threefold symmetry along the body diagonal

[50] In this section, the terms *unitcell superset* and *supercell* will be used synonymously. Later on, *supercell* will name the whole simulation box, consisting of the orthorhombic unitcell supersets introduced here.

Next, a rotation around the new z axis will be conducted to make the other Cartesian directions x and y being represented by low-indexed crystallographic directions (in order to minimise supercell volume).

Therefore we construct the lattice direction

$$\mathbf{x}' = \begin{pmatrix} h \\ k \\ \ell \end{pmatrix} \times \begin{pmatrix} 0 \\ 0 \\ 1 \end{pmatrix} = \begin{pmatrix} k \\ -h \\ 0 \end{pmatrix} \tag{4.3}$$

(which is perpendicular to the new z axis and thus an appropriate Cartesian axis) to become the new x direction. By construction, the third axis

$$\mathbf{y}' = \mathbf{z}' \times \mathbf{x}' = \begin{pmatrix} h \\ k \\ \ell \end{pmatrix} \times \begin{pmatrix} k \\ -h \\ 0 \end{pmatrix} = \begin{pmatrix} -h\ell \\ k\ell \\ -h^2 - k^2 \end{pmatrix} \tag{4.4}$$

will then point in y direction. The rotation angle is determined by $\varphi = \arccos([100] \cdot \mathbf{x}' / \sqrt{h^2 + k^2}) = \arccos(k/L_x)$.

Miller indexed direction vectors $[hk\ell]$ are great in predicting *minimum* spatial periodicity

$$\begin{aligned} u(\mathbf{r} + [hk\ell]) &\equiv u(\mathbf{r}) \quad \forall \text{ lattice-periodic } u(\mathbf{r}) \\ |[hk\ell]| &= \sqrt{h^2 + k^2 + \ell^2}, \end{aligned} \tag{4.5}$$

as long as they are *normalised* following the rule of minimum integer indices: Whenever a new lattice vector $\mathbf{z}'$, $\mathbf{x}'$, or $\mathbf{y}'$ is computed, it has to be divided by the greatest common divisor of each their components.

Obeying this, the *orthorhombic supercell dimensions*

$$\begin{aligned} L_z &= \sqrt{h^2 + k^2 + \ell^2} \qquad L_x = \sqrt{h^2 + k^2} \qquad L_y = \sqrt{h^2\ell^2 + k^2\ell^2 + (h^2 + k^2)^2} \\ V &= \sqrt{k^4\ell^4 + 2h^2k^2\ell^4 + h^4\ell^4 + 2k^6\ell^2 + 6h^2k^4\ell^2 + 6h^4k^2\ell^2 + 2h^6\ell^2 + k^8 + 4h^2k^6 + 6h^4k^4 + 4h^6k^2 + h^8} \end{aligned} \tag{4.6}$$

are only defined *modulo* an integer factor, as the computations of eqs. (4.3) and (4.4) do not guarantee minimal length, thus have to be further reduced to get the minimal orthogonal unit cell.

[110]: Cubic face diagonal inclination

$$\begin{aligned} [hk\ell] &= [110] = \mathbf{z}' \\ \mathbf{x}' &= [1\bar{1}0] \\ \mathbf{y}' &= [00\bar{2}] \Rightarrow [00\bar{1}] \\ \varphi &= \arccos(1/\sqrt{2}) = \pi/4 \\ L_z &= \sqrt{2} \qquad L_x = \sqrt{2} \qquad L_y = 1 \\ V &= \sqrt{2} \cdot \sqrt{2} \cdot 1 = 2 \end{aligned}$$

(2 unit cubes per orthorhombic supercell)

[111]: Body diagonal of a cube

$$\begin{aligned} [hk\ell] &= [111] = \mathbf{z}' \\ \mathbf{x}' &= [1\bar{1}0] \\ \mathbf{y}' &= [\bar{1}1\bar{2}] \\ \varphi &= \arccos(1/\sqrt{2}) = \pi/4 \\ L_z &= \sqrt{3} \qquad L_x = \sqrt{2} \qquad L_y = \sqrt{1+1+4} \\ V &= \sqrt{3} \cdot \sqrt{2} \cdot \sqrt{6} = 6 \end{aligned}$$

(6 unit cubes per orthorhombic supercell)

The normal view of the [111]-inclined orthorhombic supercell for a cubic structure is depicted in the inset of fig. 3.9 on page 46.

Hexagonal lattice: Orthohexagonal cells The use of structures described by hexagonal (or its superset trigonal) lattices demands a way to circumvent the orthogonality precondition for the primitive crystal lattice. This is done by the orthohexagonal basis choice: Be [100] and [010] the primitive lateral unit vectors of a trigonal unit cell, then [100] and [120] span a rectangular lattice as an appropriate basis of a C-centred orthorhombic lattice [Int04], which can directly be used as a conventional unit cell in the above sense.

4.2.4. Expectations and influences to [FDTD] reflectance spectra

Finite thickness: Fabry-Pérot pattern The reflectance off a PhC slab (consisting of a medium sufficiently homogeneous for light phases accumulate uniformly to enable interference) has been discussed in sec. 2.1.4. The conditions for FABRY-PÉROT interference are inherent to slab geometries, and as a such naturally form an integral part of finite-geometry reflectance data, though in a more subtle way due to

1. the inhomogeneous material within the slab, *i. e.* the assumption of plane waves within the slab is invalid. For regular crystalline structures, at least BLOCH waves are an available reasonable basis with a well-defined spatial periodicity, although the equalisation of the free-space wavevector $\mathbf{k}$ of plane waves and the BLOCH index "crystal impulse" $\mathbf{k}$ is spurious.

2. In case of a disordered structure, the unambiguous length scale reflecting in the number of FABRY-PÉROT humps is missing, having to be replaced by the slab thickness itself (to reduce Ω dimensionless, *e. g.*). So, in comparison with multiple-unitcell crystalline slabs, the scales differ and are no longer directly comparable.

There are two approaches to deal with this oscillatory signal. You can either average over slabs of different thicknesses to "smear out" the oscillations. By doing so (it has been done in data treatment for [Sab+14]), the prominence of the "macroscopic" [slab] geometry will be reduced in favour of the influences of the "microscopic" [in this case Gyroid] geometry.

On the other hand, the resulting flat, finite reflectance over those frequency ranges where the microstructure is essentially transparent, can no longer be distinguished from increasing reflectance caused by the microstructure itself. So, knowing about FABRY-PÉROT (and not averaging over multiple thicknesses) in distorted systems, the recognition of "well-behaved" reflectance spectra with clear minima allow to distinguish slab features from those arising from distortion itself.

Termination The position of cutting through a PhC in order to produce the surface exposed to incident radiation determines the cut face geometry, hence the local fields at the surface, and the coupling behaviour of modes into the material.

Thus its impact on reflectance behaviour shall be examined. Figure 4.6 depicts a slab of only $a$thickness, assumed thus to exhibit very pronounced termination influences. Indeed, different terminations show distinct reflectance, but the differences are in fair agreement with each other, relativising the need for termination averaging.

Two notes on sensible termination choice

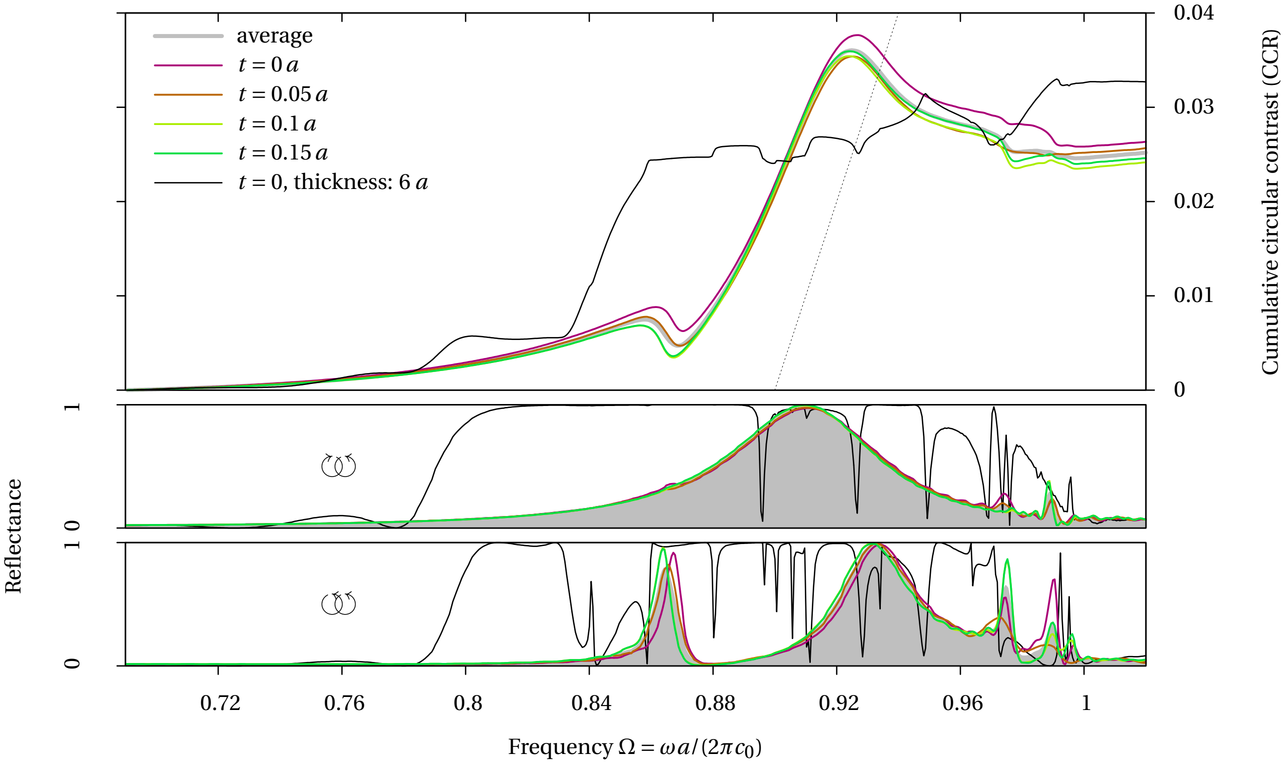

Figure 4.6.: (MEEP reflectance) Influence of structure termination t (position of real-space cut-off plane at the upper side of the slab) on the reflectance spectrum of a Gyroid (nodal approximation, $\phi = 20.4\,\%$) with a slab thickness of 1 a, *i. e.* one conventional unit cell height, and a single repetition unit in normal (Cartesian) direction. Data is compared with the same Gyroid structure, six times repeated. The ↻↺-major dichroic reflectance (positive slope in CCR) is already pronounced at thickness one, the overall reflectance exhibiting much less and broader resonance peaks, and being far lower (though reaching unity—Note that for a massive $\varepsilon = 2.4$ material, the maximum reflectance expected from thin-film interference would be 17 % after eq. (2.17)).

- Especially for circularly polarised light in crystals with screw axes: Only a maximum interval of size a/n has to be considered, where n is the folded-ness of the screw axis along viewing direction (for [001] and its 4_1 axes, $n = 4$, thus $0 < t < a/4$).
- In low-frequency-disorder systems, terminations don't make a particularly good run in creating additional randomness, thus it is best mixed it with seed statistics.

Seed statistics The importance of seed statistics arise from the desire to smear out the artificial reduction of continuously many distortion parameters into a few discrete numbers. In fairly random systems (fig. 4.7: around 6.5×10^4 amplitudes contributing, but many of them very low), the influence between seeds becomes some kind of noise, giving rise to smearing, once averaged over the seeds.[51] When the random-walk assumption breaks down due to the low number of contributing distortion modes (*cf.* also chirp: an extreme case of "seed dependence", see sec. 5.5), it may be appropriate no

---

[51] Note that seed (and, to a lesser extent, termination) statistics are, contrary to thickness averaging, a "non-invasive" intervention in the system geometry, hence perfectly valid in all situations with finite distortion originating in random number input.

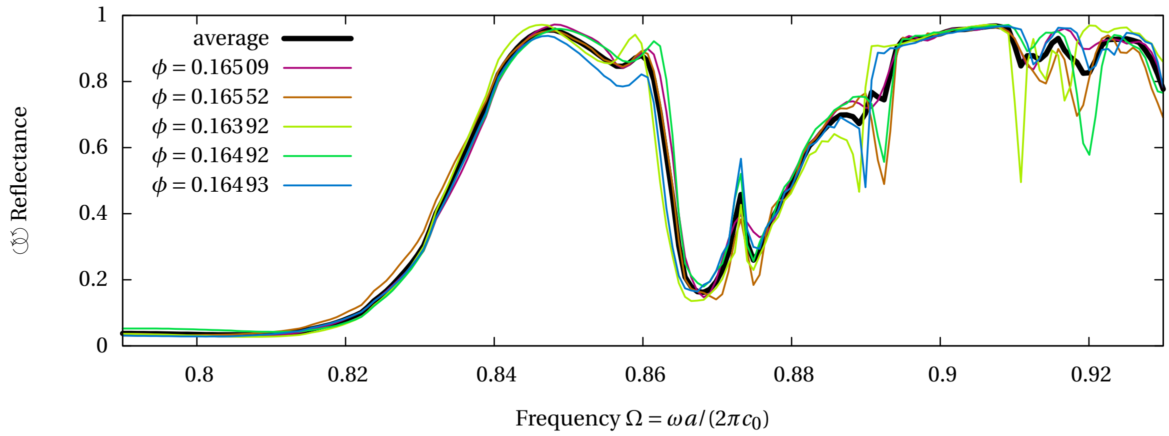

Figure 4.7.: (MEEP reflectance) Variations of reflectance details caused by the random seeds of the Fourier synthesis lattice: ↻ reflectance of a slightly ($\sigma_r/a = 0.05$) distorted network Gyroid (one subdivision, wire radius $r = 0.113\,a$, rather high-frequency Gaussian distortion with $\sigma_q a/(2\pi) = 2.1$) within a $2 \times 2 \times 6$ supercell.

longer to average over seeds, but to regard them separately—*i. e.*, seeing the distortion no longer as *random* noise, but a genuine modification of system properties.

Slab thickness and number of repetition units Figures 4.8 and 4.9 (same data basis) show up how the narrow resonance peaks standing out in PhC reflectance spectra move and deform when varying the slab thickness, *i. e.* the number of unit cells in normal direction of the slab. Analogue to smearing out Fabry-Pérot patterns, these sharp signals get smeared out by multiple-thickness averaging.

It should be noted that it is the natural way to allow variable thickness, thus averaging has its justifications. Averaging hides the most thickness-sensitive features, which is both good (for comparison with nature/experiments) and has its downsides (for distinguishing slab geometry effects from internal structure, and computational cost). For the most part of this thesis (unless otherwise noted), no thickness averaging is conducted.

4.2.5. Simulation, averaging, and data treatment

"Embarrassing" (or "idiot", *i. e.* concurrence on the application level) parallelisation is used to supervise the parameter sampling (frequency window, CP rotatory sense, random seed, distortion scale, thickness, and others) by the MEEP simulations. Data is returned in plain-text, and semi-automatically reduced (normalised against reference flux (see sec. 4.2.1), averaged over seed, termination and thickness if desired, and concatenated with respect to frequency, CP sense, distortion scale, and $k_\parallel$) by the self-written script `redumean` (written in an infamous write-only language, but documented to the best of our knowledge).

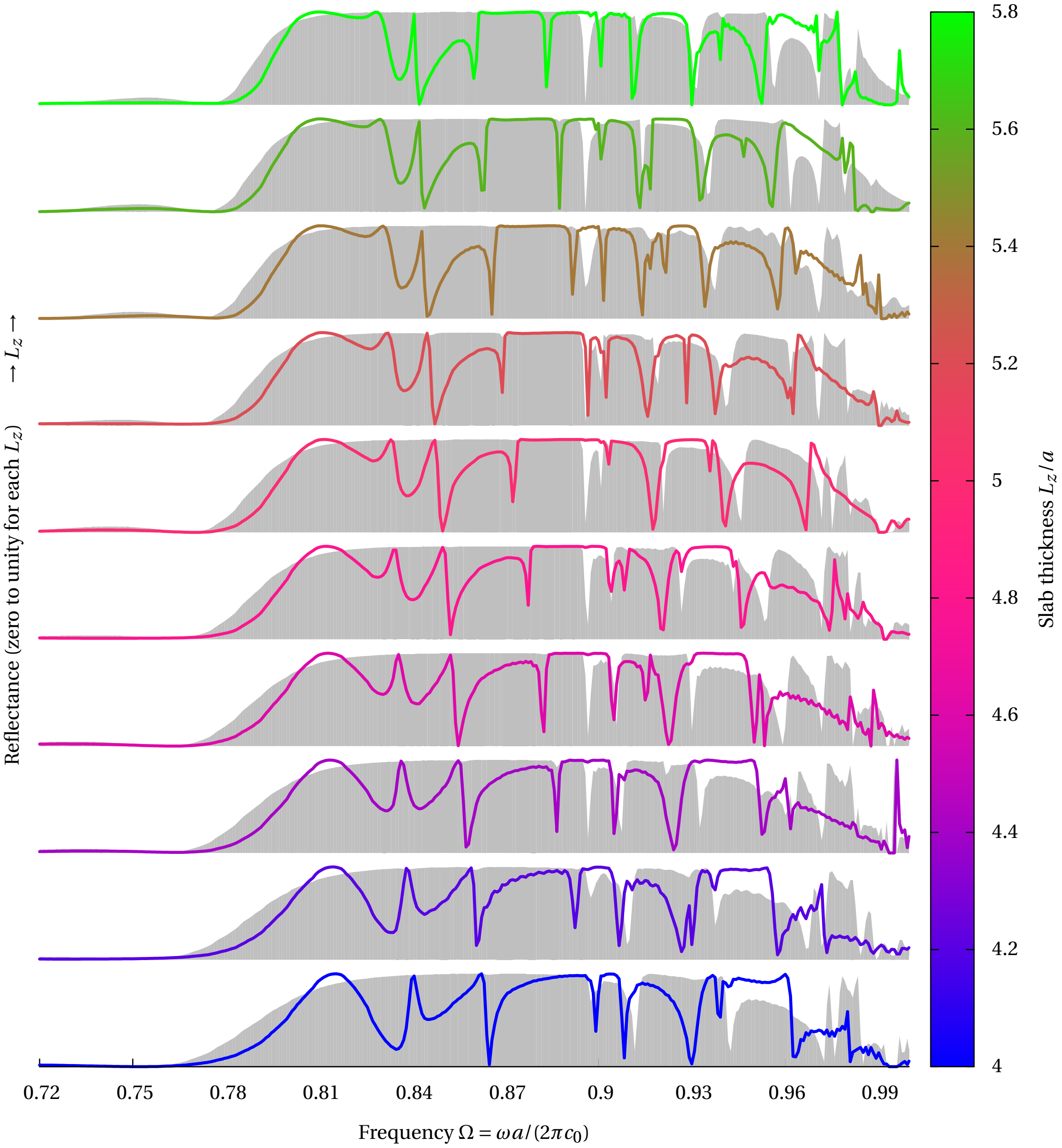

Figure 4.8.: (MEEP reflectance) Variations in [001] reflectance (coloured lines: ➰, grey areas: ➰) features with slab thickness, observed for the BCC-helical Gyroid (see sec. 3.3.3). For the frequency position of first sharp reflectance minimum, the empirical formula $\Omega = 0.966 - 0.013 \cdot L_z/a$ can be found. Also note how the lower band edge sharpens. See fig. 4.9 for CCR computed from this data.

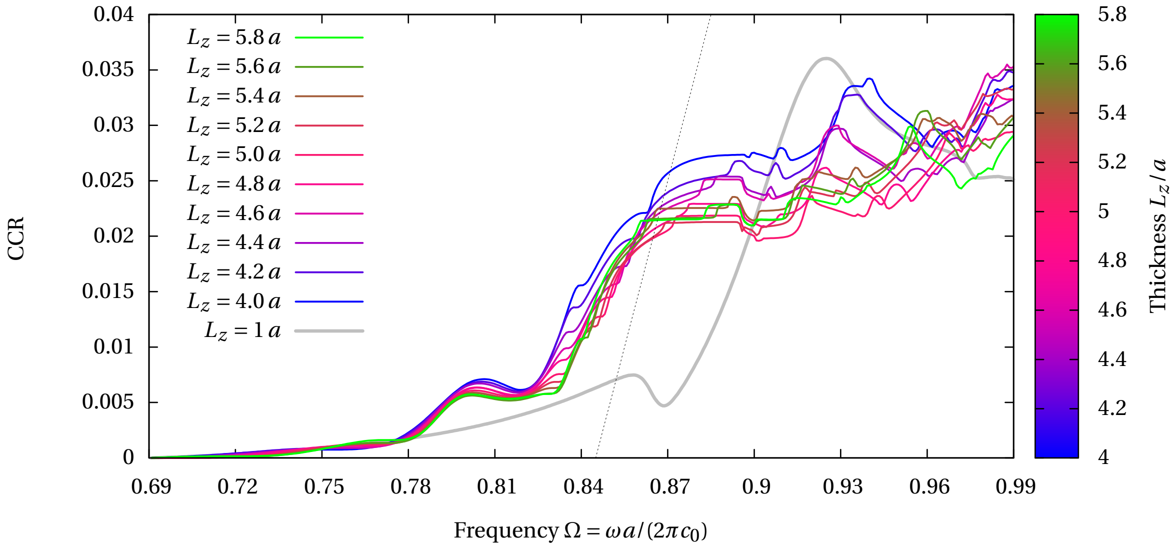

Figure 4.9.: (MEEP reflectance) Cumulative circular contrast of a [001] inclined BCC-helix Gyroid ($\phi = 20.0\,\%$) in dependence on slab thickness (*cf.* fig. 4.8 for ↺↺/↻↻ reflectance data). Also shown is the CCR signal of a single unitcube-thickness sample (from fig. 4.6).

4.3. Fourier synthesis of translational noise

Idea and Motivation

Suppose, in general, a system of which you want to identify and/or understand its structure given by its geometry $\varepsilon(\mathbf{r})$ (any physical parameter ε as a function of the space coordinate $\mathbf{r}$). A standard approach is Fourier analysis (either by the apparatus (scattering/diffraction in the far-field limit, *e. g.*) or explicitly from imaging techniques (think of spectographs, or scanning microscopy)). It delivers length scale statistics of the structure $\varepsilon(\mathbf{r})$ within the "reciprocal" or "wavevector" (the conjugate variable to the real-space coordinate) space, with inherent statistical averaging over the whole sample.

In particular, a small distortion superimposed on an otherwise regular[52] geometry, may well be characterised in its effect on its matrix by its Fourier components.

An inversion of this approach provides a means of distortion *synthesis* which is convenient in several aspects, subject to discussion in the following section: Step-wise carrying out the Fourier sum at some given over random wavevectors resembles a *random walk* in real space. The deviation of this displacement for another point of finite distance is, however, constricted by a limitation of considered wavevectors, giving rise to controllable *correlations* between the points subject to displacement.

4.3.1. Unit cell, supercell, and multiple BZ "wavevector" space

Real-space lattice We are starting from a 3D real-space periodic structure $\varepsilon(\mathbf{r})$ with discrete translation symmetry ([photonic] crystal): Its *unit cell* (UC) is the span of three non-collinear vectors $\mathbf{d}_i, i = 1, 2, 3$ which may be chosen

- either by the shortest possible set of defining vectors, to avoid redundancy within the repetition unit ("primitive" lattice/unit cell),
- or in a way which eases the way of easing the perception of the underlying symmetries or derivation from lower-symmetry primitive lattices ("conventional" lattice/unit cell).

Space is filled by copies of this UC on the places given by any sum of integer multiples $\nu_j \mathbf{d}_j,\ \nu_j \in \mathbb{Z}$ of the $\{\mathbf{d}_j\}$ real-space lattice vectors, so that translation by any vector $\sum_j \nu_i \mathbf{d}_i$ (from the lattice) is not detectable from just evaluating the structure.

The unit cell volume is given by the triple product $V_{\mathrm{UC}} = \mathbf{d}_1 \cdot (\mathbf{d}_2 \times \mathbf{d}_3)$.

Supercell This infinite definition is non-physical (as any crystal, obviously, exhibits finite spatial extent), and one has to "cut" the valid range of y_i at some finite value, *i. e.* to build a *supercell* (SC[53]). Nevertheless, the typical assumption on talking about crystals is the limit of "big" crystals, *i. e.* by taking this cut-off border arbitrarily large (or hide behind BORN–VON KÁRMÁN periodic boundary conditions), so that surface effects can be neglected [AM76]. Consequently, when talking (and thinking) about quasi-infinite structures and their *bulk* properties, it is reasonable to think of the SC as infinite as well.

---

[52] "Regular" in the sense of "crystalline", *i. e.* its Fourier components are distinctly identifiable as the wavevectors of the reciprocal lattice—see sec. 4.3.1. "Small" distortion in the sense not to destroy topology/connectedness, in general (For an exceptional "abuse", see the excessive distortion scale to produce a "gas", *cf.* sec. 5.3.2).

[53] This abbreviation is also being used to denote a *simple cubic* symmetry within other sections. Here, its meaning is distinct for supercell, which becomes clear from context.

On explicit real-space computing on crystals, the actual system size has to be traded off against the computational cost of the method in use, *i. e.* a compromise SC size has to be chosen. It will consist of $\nu_x \times \nu_y \times \nu_z$ ($\nu_j \in \mathbb{N}$) unit cells in each direction, and will be distinct from unit cell quantities by the index $^{\mathrm{S}}$ rather than $^{\mathrm{U}}$. The SC dimensions are consecutively $L_j \cdot d_j$ in either direction, giving for total a volume of $V_{\mathrm{SC}} = \prod_{j=x}^{z} \nu_j d_j = \nu_x \nu_y \nu_z \cdot V_{\mathrm{UC}}$.

Description of distortion via normal modes For the construction programme for distortions, we suppose them to be decomposable into *normal modes*, *i. e.* as a superposition of sinusoidal distortions each with a defined

- amplitude (vector) or polarisation,
- phase, relative to some origin, and
- (directed, spatial) frequency, or wavevector.

This description is an adaption of the classical description of lattice vibrations (*phonons*) in solid-state physics [AM76], differing from it in not introducing dynamics (no time-evolution, no frequency, no energy), and—as a consequence of the structure being continuous in real space (in contrast to the point-like nucleus masses of atomic crystals)—not constraining possible wavevectors to the first BRILLOUIN zone.

Reciprocal lattice The space of possible wavevectors $\mathbf{k}$ assigned to a real space is commonly referred to as the *reciprocal space*. When describing a crystal, it itself is organised into unit cells by the reciprocal lattice $\{\mathbf{G}^{\mathrm{U}}_{(hk\ell)}\}$, the set of all possible linear combinations of the primitive reciprocal basis vectors $\{\mathbf{b}^{\mathrm{U}}_j : \exp(\imath \mathbf{d}_i \cdot \mathbf{b}_j) = 1\}$ (as obtained by the standard textbook methods from the real-space lattice vectors [AM76]). The numbers h, k, ℓ (MILLER indices: characterising a distinct reciprocal lattice vector—corresponding to a set of parallel lattice planes in real space) run in principle through complete $\mathbb{Z}$.

Reciprocal lattice of the supercell For the distortion to be a property of the particular preparation (rather than part of the underlying structure itself), its real-space length scales must not match the unit cell dimensions, *i. e.* finite amplitudes at $\{\mathbf{G}^{\mathrm{U}}_{(hk\ell)}\}$ must be forbidden, as they describe the in-phase collective deformation of all unit cells.

For meshing of the reciprocal space, *i. e.* restriction on discrete values of wavevectors), the *reciprocal lattice of the SC* is chosen. By doing this, every unit-cell reciprocal vector $\mathbf{G}^{\mathrm{U}}_j$ is subdivided into ν_j of the new $\mathbf{G}^{\mathrm{S}}_j$ vectors of the supercell reciprocal lattice.

Periodic boundary conditions Any function being a *harmonic* of the SC is defined by having its Fourier components at the SC reciprocal lattice points alone, hence cannot produce discontinuities at the simulation box faces, once they are connected with their respective opposite face (periodic boundaries).[54] Thus the construction of distortion from supercell harmonics alone avoids being incommensurable with the real-space simulation box in the *lateral* directions.

---

[54] Strictly, the simulation boundary conditions are BLOCH-periodic, *cf.* sec. 4.1.1, but the arising phase factor on crossing the boundaries can only apply to the electromagnetic fields, of course. The structure $\varepsilon(\mathbf{r})$ itself is strictly periodic, *i. e.* $\varepsilon(\mathbf{r}+\mathbf{R}) \equiv \varepsilon(\mathbf{r}) \forall \mathbf{R} \in \{\mathbf{d}^{\mathrm{S}}_j\}$.

The same restriction is also chosen to apply in the direction *normal* to the constructed material slab (*cf.* sec. 4.2.1). Though not mandatory,[55] it ensures some (non-mandatory) degree of symmetry in reciprocal space between normal and lateral directions (both types of direction are discretised). In case of the normal-direction extent of the simulation box (thickness) being not an integer multiple of the respective unit cell dimension, the number of unit cells will be rounded up, and the remains will be truncated.

4.3.2. Distortion field

We use the set of basis functions defined by the supercell reciprocal lattice to construct the field of real-space displacements[56] $\mathbf{u}(\mathbf{r})$ subject to which points will be displaced, by a Fourier series over the whole set $\{\mathbf{G}^{\mathrm{S}}\}$ of supercell reciprocal lattice vectors[57]:

$$\mathbf{u}(\mathbf{r}) = \sqrt{2\Upsilon} \sum_{\mathbf{q}\in\{\mathbf{G}^{\mathrm{S}}\}} \mathbf{u}_{\mathbf{q}} \cos\left(\mathbf{q}\cdot\mathbf{r} + \varphi_{\mathbf{q}}\right) \tag{4.7}$$

with the normalisation constant $\Upsilon = (\sum_{\mathbf{q}})^{-1} = |\{\mathbf{G}^{\mathrm{S}}\}|^{-1}$. As, in general, a Fourier series exhibits complex coefficients, but displacements shall be real, all degrees of freedom related to the wave phase will be absorbed into $\varphi_{\mathbf{q}}$.

So, any wavevector $\mathbf{q}$ within the regarded range $|\{\mathbf{G}^{\mathrm{S}}\}|$ of supercell reciprocal lattice vectors carries, alongside its position $\mathbf{q}$ implicitly storing the wavelength $2\pi/q$ and phase front normal $\mathbf{e}_q$, a polarisation vector $\mathbf{u}_{\mathbf{q}}$ (defining both the strength and direction of the distortion), and the phase $\varphi_{\mathbf{q}}$ at the coordinate origin.

In practice, the distortion field comes to an application while constructing a structure made from discrete objects. Every time a coordinate $\mathbf{r}$ is queried, the value of $\mathbf{u}(\mathbf{r})$ is requested, and added prior to further application.[58]

For technical details see sec. 4.4.

4.3.3. Synthesis, specification, illustration

Autocorrelation function

For sufficiently many Fourier components (initialised with random polarisation and phase), displacement at some given point is random, but locally deterministic in a sense that on moving away from this point, the change of displacement is at most as fast as given by the most distant Fourier component.

This "knowledge" of a point over the behaviour of others, esp. its neighbours, is expressed by the *(auto)correlation function* $G(x)$. It depicts the degree of dependence of the field $\mathbf{u}$ at $\mathbf{x}$ on the value at some $\mathbf{x}+\mathbf{r}$ in a distance[59] $x = |\mathbf{x}|$ (via the scalar product of the two vectors), corresponding to the self-convolution of $\mathbf{u}(\mathbf{r})$.

---

[55] Rather than the periodic duplicate of itself, the structure is terminated by vacuum, sources/detectors and finally absorber layers in normal direction.

[56] This terminus must not be confused with MAXWELL's name for $\mathbf{D}$, the *electromagnetic displacement* field! It rather describes geometric distortions continuously as a function of space.

[57] The choice of what model of distortion is applied impacts the range of non-zero components, thus restricting the number $|\{\mathbf{G}^{\mathrm{S}}\}|$ of wavevectors to be considered. See sec. 4.4

[58] Note that this is equivalent to a Fourier transformation of $\mathbf{u}_{\mathbf{q}}$ into real space $\mathbf{u}(\mathbf{r})$. Hence it might be made far more efficient using stock FFT routines, rather than explicit "by-hand" evaluation of eq. (4.7).

[59] The fact that x is a scalar distance will express (rather: imply) averaging over the solid angle.

$$
\begin{aligned}
G(\mathbf{x}) =& (\mathbf{u} * \mathbf{u})(\mathbf{x}) = \\
=& \Upsilon \sum_{\mathbf{q}} \mathbf{u}_{\mathbf{q}} \cdot \Big(\cos(\mathbf{q}\cdot\mathbf{x}) \left(\mathbf{u}_{\mathbf{q}} + \mathbf{u}_{-\mathbf{q}} \left(\cos^2(\varphi_{\mathbf{q}}) - \sin^2(\varphi_{-\mathbf{q}})\right)\right) + \\
& + \sin(\mathbf{q}\cdot\mathbf{x}) \cdot \mathbf{u}_{-\mathbf{q}} \left(\sin(\varphi_{\mathbf{q}}) \cos(\varphi_{\mathbf{q}}) + \sin(\varphi_{\mathbf{q}}) \cos(\varphi_{-\mathbf{q}})\right) \Big)
\end{aligned}
\tag{4.8}
$$

The calculation route from the definition (4.7) in terms of a (real-valued) Fourier sum, to (4.8), the final correlation function in the most general case, is given in the appendix at B.1 on page 113 for the curious reader.

For scalar $x = |\mathbf{x}|$, *i. e.* by averaging over the full solid angle (by applying $\int \mathrm{d}^2\Omega \cos(\mathbf{q}\cdot\mathbf{r}) = 4\pi\, j_0(|\mathbf{q}|r)$ with Bessel's $j_0(x) = \sin(x)/x$, and exploiting the fact $\sin(\mathbf{q}\cdot\mathbf{r})$ being an odd function of $\mathbf{r}$), one gets

$$
G(x) = \int \frac{\mathrm{d}^2\Omega}{4\pi} G(\mathbf{x}) = \Upsilon \sum_{\mathbf{q}} \mathbf{u}_{\mathbf{q}} \cdot \left(\mathbf{u}_{\mathbf{q}} + \mathbf{u}_{-\mathbf{q}} \left(1 + \cos^2(\varphi_{\mathbf{q}}) - \cos^2(\varphi_{-\mathbf{q}})\right)\right) \cdot j_0(|\mathbf{q}|x) \tag{4.9}
$$

Supplying sufficient statistics, *i. e.* both $\left\langle \cos^2(\varphi_{\mathbf{q}}) \right\rangle \cong \frac{1}{2}$ and $\left\langle \mathbf{u}_{\mathbf{q}} \cdot \mathbf{u}_{-\mathbf{q}} \right\rangle \cong 0$ ($\langle\cdot\rangle$ denoting averaging over all wavevectors contributing to distortion), this reduces further to

$$
G(x) \cong \Upsilon \sum_{\mathbf{q}} \mathbf{u}_{\mathbf{q}}^2 \cdot j_0(|\mathbf{q}|x) \tag{4.10}
$$

A particularly important implication of eq. (4.10) is the interpretation of distortion scale, arising from the value at $x = 0$: Compare $G(0) \cong \Upsilon \sum_{\mathbf{q}} \mathbf{u}_{\mathbf{q}}^2 = \langle \mathbf{u}_{\mathbf{q}}^2 \rangle$ with the standard expression of the mean square displacement $\left\langle \mathbf{u}(\mathbf{r})^2 \right\rangle = \int_V \mathbf{u}(\mathbf{r})^2 \, \mathrm{d}^3 r / V = G(0)$.

In comparison with the well-known value of a Gaussian distribution $\left\langle \mathbf{u}_{\text{Gauss}}^2 \right\rangle = \sigma^2$, we approximate $\sigma = \sqrt{G(0)}$ as the second-moment measure of the mean RMS displacement (disregarding correlation) being generated by application of any distortion expressed by a Fourier series (complying with the constraint of being “sufficiently random”, *i. e.* having many modes with independent polarisations and phases). In effect, the subsequent evaluation of the summands in the Fourier sum eq. (4.7) equals a *random walk* in real-space, the lengths given by the respective $|\mathbf{u}_{\mathbf{q}}|$ (times the spatial cosine phase factor), and with directions of the amount of randomness you feed your model with. The notable difference (and the reason for this work) is the correlation between adjacent “random” trajectories, enabling the construction of collective (long-range) distortions.

Note that in the case these conditions are not met, the simple scalar $G(x)$ is no longer a valid parameter for describing correlations within distortion.

A simpl(e|istic) example

We want to illustrate the distortion field formalism by a choice of the free parameters in eq. (4.7) with crude simplifications compared to more appropriate and sophisticated models:

Zero phase $\varphi_{\mathbf{q}} \equiv 0$ at all components, and the displacement $\mathbf{u}_{\mathbf{q}}$ with Gaussian amplitude[60] in $|\mathbf{q}|$, centred around some mean wavenumber q_0 with a narrow distribution width $\sigma_q \ll q_0$:

$$
\begin{aligned}
\mathbf{u}_{\mathbf{q}} =& \frac{\mathbf{n}}{|\mathbf{n}|} \exp\left(- \frac{(|\mathbf{q}| - q_0)^2}{2\sigma_q^2} \right) = \mathbf{u}_{-\mathbf{q}} \\
\varphi_{\mathbf{q}} =& 0 \quad \forall \mathbf{q}
\end{aligned}
\tag{4.11}
$$

---

[60] The displacement polarisation is chosen parallel to some arbitrary, but fixed direction **n** without further relevance.

so that for the correlation function, eq. (4.9), we get

$$\begin{aligned} G(x) &= \sum_{\mathbf{q}} \mathbf{u}_{\mathbf{q}}^2 \cdot j_0(|\mathbf{q}|x) \\ &= \sum_{\mathbf{q}:\,|\mathbf{q}|=q} \exp\left(-\frac{(q-q_0)^2}{\sigma_q^2}\right) j_0(qx) \end{aligned} \tag{4.12}$$

which can, in the case of a narrow $\sigma_q \ll q_0$, *i. e.* few (down to a single) **q** dominating the sum, be interpreted as

1. an approximative (discrete) sine Fourier transform of a Gaussian: $qx \approx \text{const}\ \forall |\mathbf{u}_q| \not\ll 1$ and thus $j_0(qx) \mathrel{\tilde{\propto}} \sin(qx)$. This is therefore approximately Gaussian-like, and centred around $\mathbf{x} = \mathbf{0}$
2. a sum of few Gaussians modulated by Bessel's j_0 (sinc) function whose frequency is characterised by the requested test length **x**.

An analytically solvable (over)simplification is to permit only a single distortion wavevector length to contribute by letting $\sigma_q \to 0$:

$$\begin{aligned} \lim_{\sigma_q \to 0} \mathbf{u}_{\mathbf{q}} &= \frac{\mathbf{n}}{|\mathbf{n}|} \lim_{\sigma_q \to 0} \exp\left(-\frac{(|\mathbf{q}|-q_0)^2}{2\sigma_q^2}\right) \propto \delta(|\mathbf{q}|-q_0) \\ G(x) &\propto \sum_{\mathbf{q}} \delta(|\mathbf{q}|-q_0) \cdot j_0(|\mathbf{q}|x) \propto \\ &\propto \sum_{\mathbf{q}:\,|\mathbf{q}|=q_0} j_0(qx) \propto \\ &\propto j_0(q_0 x) = \frac{\sin(q_0 x)}{q_0 x} \\ \left| j_0(q_0 x) \right| &\leq \frac{1}{|q_0 x|} \quad \forall x \neq 0 \end{aligned} \tag{4.13}$$

So the correlation function of this extreme case will disclose the Bessel function as the elementary three-dimensional correlation of plane waves with respect to solid-angle averaging, showing the slowest possible correlation decay proportional to $1/x$. Any Fourier component distribution with finite σ_q will introduce several incommensurate sinuses into eq. (4.13), so that the correlation decay will be faster than $1/x$. See figure 4.10 for a depiction.

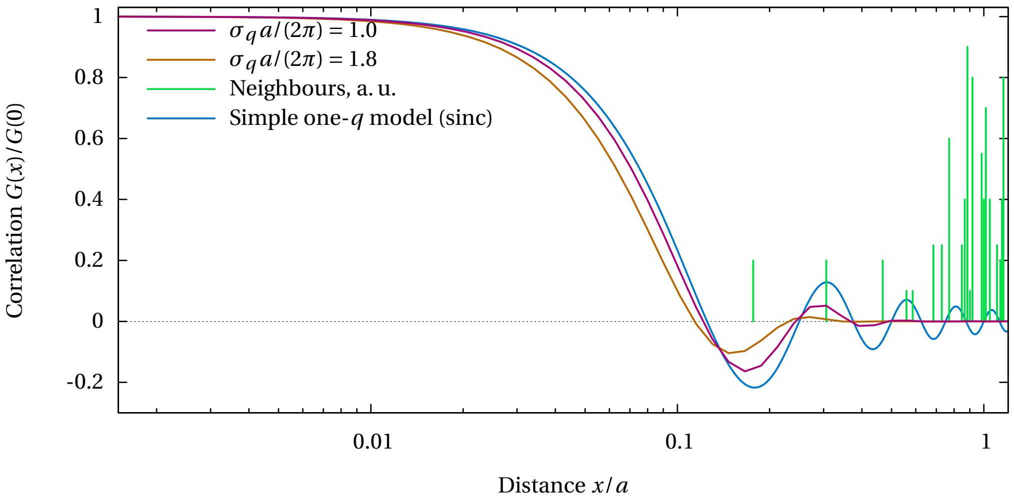

Figure 4.10.: Comparison of the single-component correlation functions resulting from distinct distortion models: the analytical result of the simple model described in section 4.3.3, and data from numerical evaluation (with random phase) for two distinct distribution widths σ_q with a common wavevector distribution centre $q_0 = 4 \times 2\pi/a$. The "neighbours" depict the inter-vertex distances of a **1srs** network (sec. 3.3.2) with one subdivison per edge. They are drawn aside, to illustrate common distances at which the correlation will be relevant, actually.

4.4. Description of distortion generation

4.4.1. The process of modelling distortion

Now follows a short description of how the distortion field works in conjunction with the structure construction code developed for this thesis.

The distortion field is constructed as a three-dimensional array with an interface to be addressed by the $(hk\ell) \in \mathbb{Z}^3$ indices of the supercell reciprocal lattice of a size to comfortably hold the major distortion contributions, e. g. $2\pi|h|/L \gtrsim q_0 + 2\sigma_q$ for amplitudes Gaussian in q.

The effect of the distortion field at any point $\mathbf{r}$ can be evaluated according to eq. (4.7). On constructing any geometry defined by discrete (vertex, centre, etc.) coordinates, this displacement is applied any time on requesting a coordinate, prior to the actions performed by the respective method. This way continuity of distorted discrete structures (network graphs blown up to wires of finite thickness, *e. g.*) is guaranteed both within the volume, and across the periodic boundaries of the supercell box.

Amplitudes Arbitrary distortions are constructed from the array of Fourier modes $\mathbf{q}$ by setting their amplitude vectors $\mathbf{u_q}$ to finite amplitudes, according to the desired model of distortion. Typical simple models are given in the following section 4.4.2.

For the creation of quasi-random noise, this study largely restricts on an amplitude envelope of Gaussian shape $|\mathbf{u}_q| \propto \exp(-q^2/2\sigma_q^2)$ (with random orientation, and phase), largely due to its conceptual simplicity (one single dimensional parameter: its standard deviation σ_q gets easily connected to the real-space correlation length, *cf.* 4.3.3).

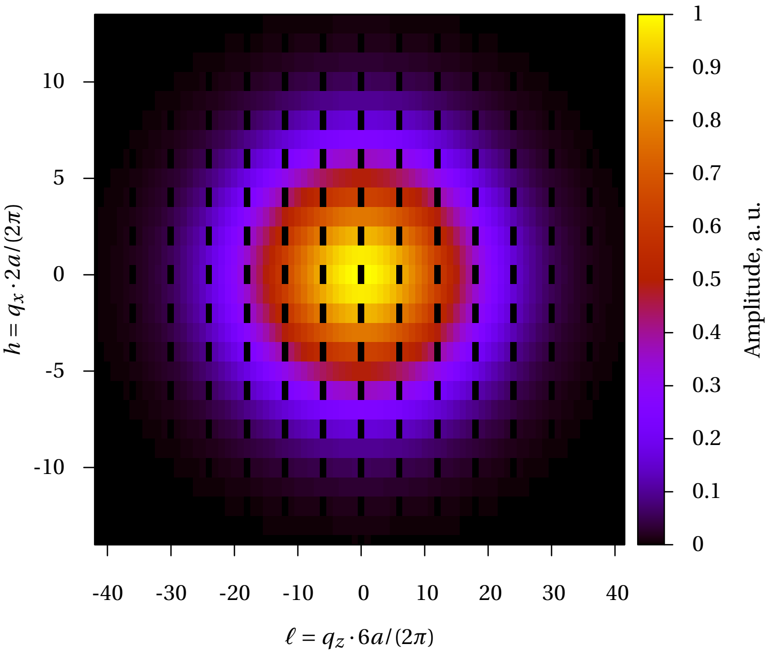

Figure 4.11.: Amplitudes of the Fourier grid (used to distort the cubic example structure of sec. 4.5.2): the central 2D slide at $k = 0$ of all $(h0\ell)$ supercell reciprocal lattice vectors, with the amplitudes at the simple-cubic unitcell reciprocal lattice zeroed out. Distortion amplitudes are Gaussian distributed, with a width $\sigma_q a/(2\pi) = 2.1$, centred around $q_0 = 0$. Simulation box size: $v_x \times v_y \times v_z = 2 \times 2 \times 6$ unit cubes, reflecting in the unitcell reciprocal lattice points at $(2h^\mathrm{S}, 2h^\mathrm{S}, 6\ell^\mathrm{S})^\mathrm{T} \forall h, k, \ell \in \mathbb{Z}$ (hence cuboid “voxel” shapes).

Avoid unit cube harmonics After filling the reciprocal grid with the randomness of choice, it is appropriate to set the amplitude at any point coinciding with a reciprocal lattice vector (harmonic) of the unit cell $\{\mathbf{G}^\mathrm{U}\}$ to zero:

$$\mathbf{u}_\mathbf{q} = 0 \quad \forall\, \mathbf{q} \in \{\mathbf{G}^\mathrm{U}\} \tag{4.14}$$

Those would describe a sinusoidal distortion which is commensurate with the unit cell lattice, thus uniformly rearranging vertices of all unit cells in the same way.[61] Of special importance is a zero at the origin of reciprocal space, which would otherwise describe a mere *translation* of the crystal as a whole.

Exclusion of those UC harmonics will thus preserve “ensemble-mean” unit cell geometry (same distortion starting point structures for every unit cell within a structure, and across different initialisation states, *i. e.* random seeds), but then the Fourier lattice (= distortion model) will be “perforated” by a regular zero grid overlay—see fig. 4.11.

---

[61] In the words of “phonons” populating the extended zone schema of the reciprocal space, these are the Γ points of the unit-cell reciprocal lattice, *i. e.* DC components, describing those distortion having no phase difference between real-space unit cells.

Scalar sampling In addition to the distortion field itself, describing displacements smoothly with maximal spatial frequencies according to the highest-wavevector modes of finite amplitude, it may be appropriate to sample some *scalar* quantity from the field, exhibiting the same smoothness properties, but being linearly independent from the distortion field itself (and other scalars, if required). To accomplish this, the distortion field at the sampling position (shifted by a "large"[62] vector to avoid coherence with the distortion vector at this point) is projected along an arbitrary, but fixed axis, to yield a scalar with the same correlation properties as the distortion vector components (which are, in essence, such scalars with the Cartesian unit vectors as projection axes).

4.4.2. Description of the software interface

The distortion field construction starts with defining the range of a finite subset $\{\mathbf{G}^\mathrm{S}\}$ of the supercell-reciprocal lattice. On this array, each point stores the Fourier amplitude vector and phase contributing to the distortion vector field. This section presents the methods implemented to construct a desired distribution of Fourier amplitudes within this reciprocal lattice.

Single Modes `c_grid::distortion_single`

The conceptual and technical basis of distortion creation is to set the polarisation and phase of a single mode (point in the considered part lattice of reciprocal space). It is used internally by all other procedures, and thought only for that, with the prominent exception of creating highly deterministic distortions:

Most notably (longitudinal[63]) "chirp": The distortion mode at $(hk\ell) = (001)$ (first supercell harmonic in normal direction) is set to dominate the reciprocal lattice with a distortion polarisation vector $\mathbf{u}_{(001)}$ along z direction. Such a mode can coexist with other distortion models, just by being explicitly superimposed.

Gaussian distortion profile `c_grid::distortion_gaussian`

The absolute values of amplitudes form a Gaussian profile in their radial wavevector dependence:

$$|\mathbf{u_q}| = \exp\left(-\frac{(|\mathbf{q}| - q_0)^2}{2\sigma_q^2}\right) \tag{4.15}$$

representing a Gaussian distribution if centred around $q_0 = 0$, and a ring profile when $q_0 \neq 0$. Phases are uniformly sampled from a random number generator.[64]

It offers a "cumulative" option: to just add the vectors (and, proper weighted, the phases) to the existing ones, forming a superposition of distortion models (*e. g.*, to create bi-modal distortions).

Multimodal Gaussian `c_grid::distortion_gaussian` with vector q_0/σ_q

This Gaussian method is overloaded to accept "vectorial" input quantities q_0 and σ_q: Initialisation of Gaussian width (σ_q) or the wavevector length centre (q_0) allow anisotropic envelopes oriented with respect to the Cartesian directions of the reciprocal lattice.

---

[62] Large in comparison with the maximum possible coherence length (simulation box body diagonal times an irrational number larger than unity).

[63] The same way, transversal (polarisation vector in the lateral plane) or even circular (Single modes at $\pm hk\ell$ with same `fv_vec` and `f_phases` different by $\pi/2$) chirp-like distortions are imaginable.

[64] In all cases throughout this thesis when "true" randomness is desired, it is obtained from the GNU GSL *combined Tausworthe* generator `gsl_rng_taus` [Gal09].

Distortion modifier: Anisotropic polarisation vectors `c_grid::diagscale_all`

Additionally to the amplitude vector lengths $|\mathbf{u_q}|$ exhibiting direction dependence (determining correlation lengths in real space), their *direction* $\mathbf{u_q}$ (hence the direction-dependent *amount* of distortion) can be made anisotropic, primitively, by multiplying with a linear, diagonal transformation matrix $\mathbf{u_q} \to \mathrm{diag}(\mathbf{s})\mathbf{u_q}$ with any scaling vector $\mathbf{s}$ giving the factors for Cartesian components.

Wavevector exclusion `c_grid::exclude_lattice_harmonics`

The zeroing of unitcube harmonics, as described on page 70, is automated by pre-defined lattices for FCC, BCC and simple cubic lattice harmonics.

Choosing the primitive lattice (*i. e.* BCC for the Gyroid) is preferred over blanking out a conventional lattice, as unit cell harmonics of a non-primitive lattice do not necessarily describe uniform distortions of *all* primitive cells in the same way, re-qualifying as appropriate distortion vectors.[65] This way, the number of blanked-out Fourier components is limited to a minimum.

Normalisation `c_grid::scale_distortion_to_rms_expectationvalue`

After the desired model of distortion has been assembled, it will be *normalised* to the desired degree of real-space vertex displacement σ_r. Therefore, the result of section 4.3.3 will be used to rescale all distortion amplitudes: Numerical evaluation of $G(0)$ results in the (dialled) *scale of real-space displacement* σ_r, in its variation over the sampling of the distortion field at different real-space points. In the case of a $q = 0$ Gaussian model, σ_r can be identified as the *standard deviation* of the distortion function. Conveniently, the distortion scale is expressed in dimensionless units as σ_r/a.

4.5. Checks and examples

4.5.1. Distortion: distribution shape and correlation scales

For a first proof-of-concept check, the distortion field is sampled at random places. This is not a realistic case for real structure initialisation, as the sampling is conducted on a regular lattice (which is, in addition, commensurable with the distortion field periodicity constraints). Figure 4.12 depicts sampling results, and suggests a reasonable “global” randomness of distortion (disregarding the intentional correlation effects on small distances).

Next, sampling points are taken from the realistic BCC helix Gyroid model (fig. 4.13). The Helix Gyroid is chosen as an example due to its comparatively large distances between vertices.

At a fixed distortion scale σ_r/a, the distribution width σ_q in the reciprocal lattice is manipulated. In the limit of relatively-long-range distance statistics, distortions approach the same behaviour irrespective of σ_q, but on short distances, the smearing caused by is pronouncedly lower for systems with long spatial correlation (low σ_q), where adjacent points “know” more about their neighbourhood.

4.5.2. 1srs network graph

The structure As a first real-life example, we apply the described distortion field technique to a **1srs** Gyroid network, as described at 3.3.2. To increase the number of distorted points, every edge is subdivided into two parts by an additional intermediate vertex.

---

[65] This is synonymous with the primitive lattice’s BZ being the largest possible reciprocal space Wigner–Seitz cell without introducing additional “unnecessary” points.

Distortion Again, distortion is created with a Gaussian envelope in $\mathbf{q}$ space, similar to eq. (4.11). In difference to the model case of sec. 4.3.3, the polarisation direction $\mathbf{n}$ is randomly distributed, as well as the phase φ_q, and the centre q_0 is chosen to zero, leading to distortion components:

$$\mathbf{u_q} = \begin{cases} 0 & \mathbf{q} \in \{\mathbf{G}^{\mathrm{U}}\} \\ \dfrac{\mathbf{n_q}}{|\mathbf{n_q}|} \exp\left(-\dfrac{|\mathbf{q}|^2}{2\sigma_q^2}\right) & \text{else} \end{cases} \tag{4.16}$$

The supercell is chosen to hold $v_x \times v_y \times v_z = 2 \times 2 \times 6$ unit cubes, see, *e.g.*, in fig. A.4 on page 112. Wire thickness is chosen to $0.113a$, which yields a room-filling fraction ϕ of approximately 14 % in the unperturbed case; growing with distortion due to increasing edge lengths. Dielectric contrast is determined by the material dielectric constant $\varepsilon = 2.4$.

A rough analysis of the (pseudo-)randomness induced by the distortion field is done in two steps:

Single-sample test (see fig. 4.14) Comparison of distribution of the distortion vectors $\mathbf{u}(\mathbf{r})$ (as they are requested by the construction routines) with the distribution function $1/2\left(\operatorname{erf}\left(x/(\sigma_r\sqrt{2})\right)+1\right)$ of the Gaussian distribution of the components, and the cumulative Maxwell-Boltzmann distribution $\operatorname{erf}(x/(\sigma_r\sqrt{2})) - \sqrt{2/\pi}\cdot x/\sigma_r \cdot \exp(-x^2/(2\sigma_r^2))$ for the vector lengths. Agreement between coordinate samples and the Gaussian distribution correlates with a in-general normal distribution of distortion vector components, while disregarding spatial localisation or non-locality, resp., of the distortion.

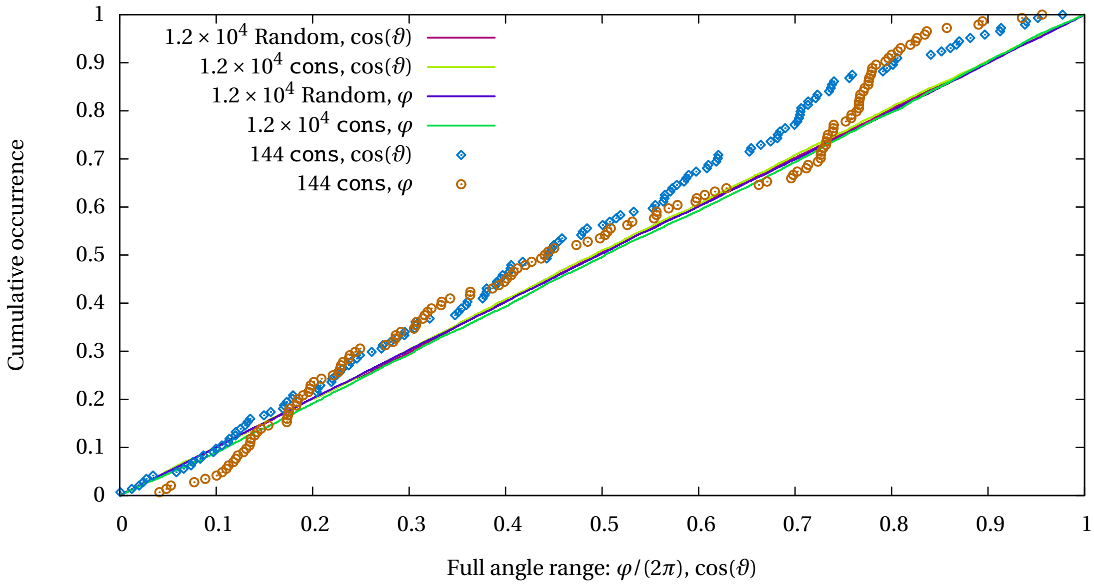

Figure 4.12.: Comparing random-location sampling of the distortion field (`cons`) with vectors uniformly random directed into the whole solid angle (`gsl_ran_dir_3d` from the GNU GSL library [Gal09]). Distortion field values of the $z = \cos(\vartheta)$ component and the azimuthal angle φ are, for appreciable statistics, in well agreement with uniform distribution, and naturally exhibit fluctuations in the limit of few samples (144 test point: data from realistic helix Gyroid initialisation).

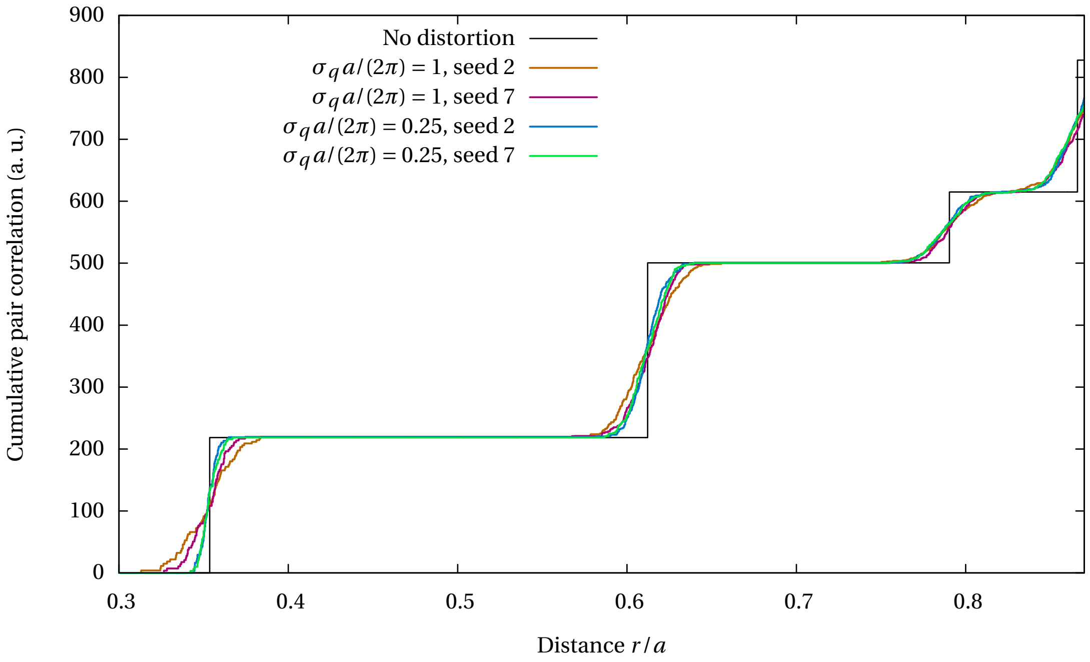

Figure 4.13.: Cumulative pair correlation function of the helix centres as they are sampled in defining the BCC-basis Gyroid. On applying distortion (all data from a single distortion scale $\sigma_r/a = 0.01$), the distribution of distances widens from discrete “neighbourhood” steps to a finite-variance sigmoid, broadening with increasing distance r. Distorted data differs by the respective width of the Gaussian distribution of distortion amplitudes within the Fourier grid, *i. e.* the real-space correlation lengths. By increasing range (lowering σ_q), distributions sharpen for small spacings. At larger distances, the differences vanish. Several curves are shown to compare for the influence of random seed statistics.

Correlation length (see fig. 4.15) Evaluation of the autocorrelation function $G(x)$, see eq. (4.10), as a function of the distance $x = |\mathbf{x}| = |\mathbf{r}_1 - \mathbf{r}_2|$ between two points 1 and 2. On the scale of the pair correlation of the structure vertices (as depicted within the figure for the undisturbed **1srs**), this tells how much—in average—the distortion at a single point depends on the distortion at a distance x. In this case, only the very next neighbours (original vertices ↔ edge subdivisions) exhibit significant correlations.

Figure 4.11 (p. 70) has served as an illustration how the Fourier grid actually looks like. The exclusion of cubic unit cell harmonics is visible as (black) zeros at the UC reciprocal lattice vectors; Fourier grid slides with fractional μ_j never contain any $\mathbf{q} \in \{\mathbf{G}^{\mathrm{U}}\}$ and thus show no such “holes”.

The anisotropy in reciprocal spacing (“non-square pixels” of fig. 4.11) is due to prolate supercell dimensions, which lets the lateral resolution be coarser than the resolution in normal direction.

FDTD: Reflectance Once the super cell is initialised and properly distorted, it can be used as a simulation box within FDTD simulations. The process and observations may be illustrated by the example data set in fig. 4.16.

In parallel with the reflectance simulations, the volume-filling fraction ϕ is determined (inset), as it plays a vital role for discussion of spectrum changes (most notably, red-shifts on increasing ϕ and mean refractive index, respectively [Joa+08]). Note that extracting the volume fraction from MEEP's ε output (HDF5 format) has proven unreliable, seemingly due to MEEP's anisotropic sub-pixel averaging [Far+06]. Therefore, the direct evaluation of the plain-text interchange format (between the structure creation program and the MEEP set-up) is better suited to obtaion ϕ data (at double resolution, in effect, as MEEP oversamples its material function with the double desired resolution, again, to compute sub-pixel ε).

Departing from the undisturbed structure (grey shaded) until $\sigma_r / a \approx 0.1$, CD decreases in the area of the dichroic ↺-major reflectance stop band ($\Omega \approx 0.84$), both in strength and bandwidth. In parallel, the reflectance within the fundamental region $\Omega \lesssim 0.81$ increases for both ↻ and ↺ by roughly the same value, increasing absolute reflectance, but not CD.

On approaching $\sigma_r / a \approx 0.2$, the shape of the reflectance changes dramatically, with stop-band CD spreading to a broad and diffuse ↻-major "plateau", and significant ↺-major reflectance emerges at low frequencies $\Omega \lesssim 0.8$.

An overall red-shift for the visible features is observed. This behaviour must be seen against the background of the volume filling fraction (which increases by a factor of 2 within the depicted distortion interval, due to the network edges elongating on the distortion of the vertices): An overall increased space fraction occupied by high-dielectric (an increased "mean dielectric constant") will, in general, lower the frequencies of corresponding modes.

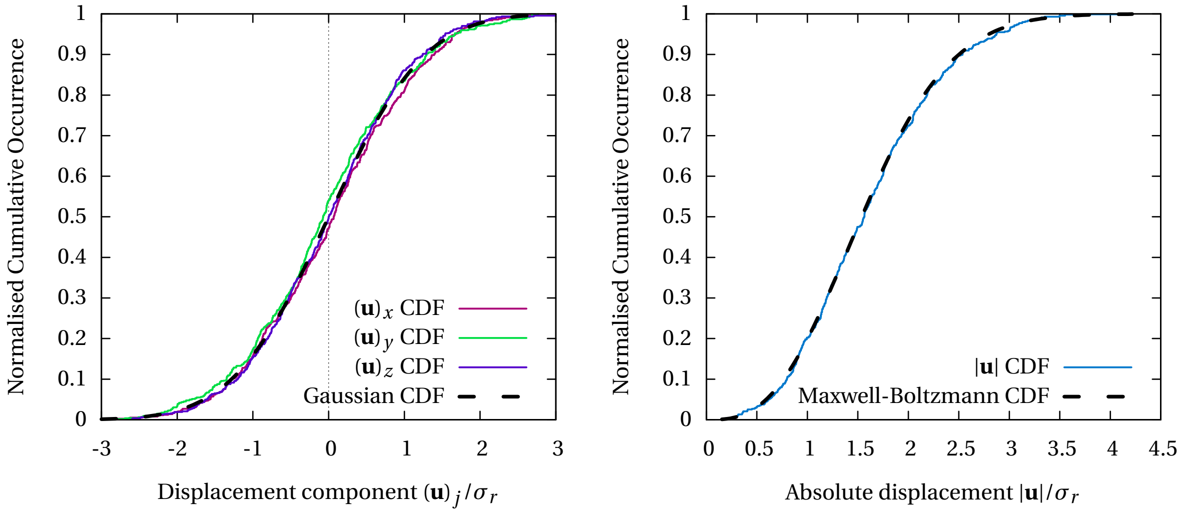

Figure 4.14.: Approximate random noise by distortion on a Fourier grid, part 1: Gaussian-ness CDF (cumulative distribution function) of displacement components $(\mathbf{u})_j$ (left) and the absolute value $|\mathbf{u}|$ (right). Simulation results in comparison with the anticipated CDFs of a Gaussian-distributed random variable (components: Gauss's error function, absolute value: Maxwell-Boltzmann CDF).

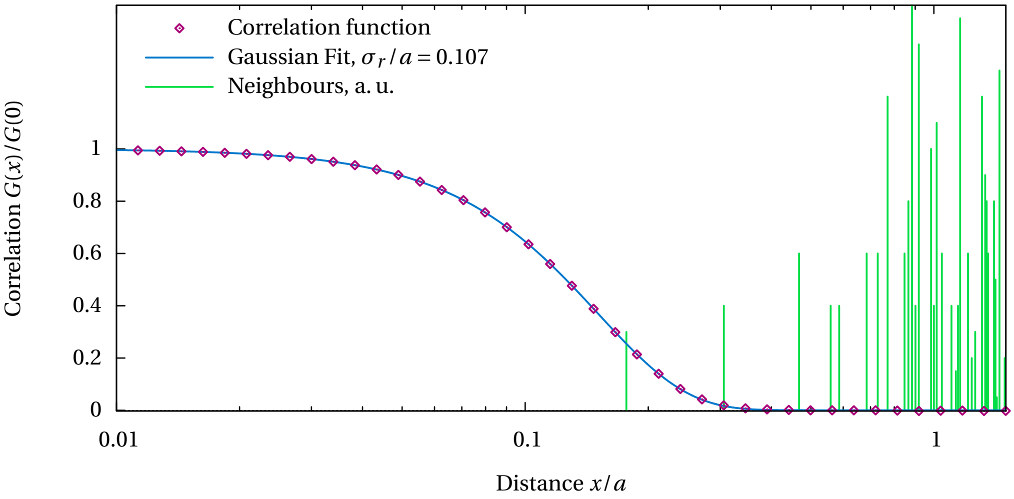

Figure 4.15.: Approximate random noise by distortion on a Fourier grid, part 2: correlation between nearby points. $\sigma_q = 2.1$, $q_0 = 0$ (thus no high-frequency oscillations at high distances). The (undistorted) "neighbour" distances (to the vertices of a **1srs** network with one subdivison per edge) are drawn aside, to illustrate common distances at which the correlation will be relevant, actually. A Gaussian fit to the correlation function shows up a correlation length σ_r slightly larger than 0.1 due to exclusion of unit cell harmonics.

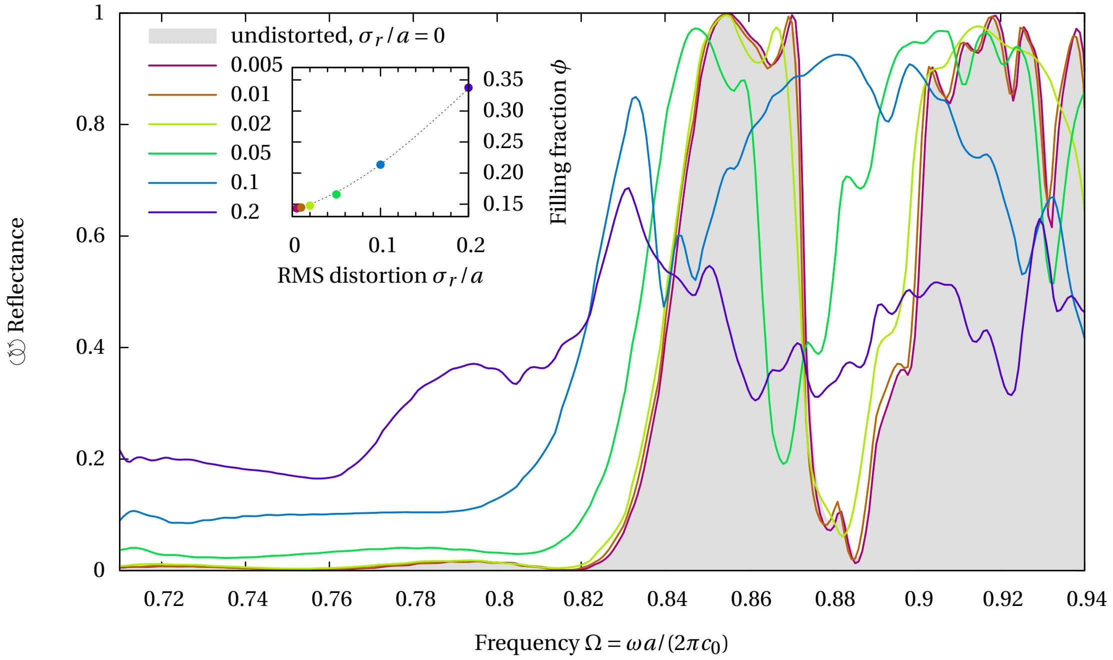

Figure 4.16.: (MEEP reflectance) Change in ↺ reflectance of the **1srs** network Gyroid (1 subdivision) when increasing σ_r, the amount of distortion (reciprocal space distribution width $\sigma_q a/(2\pi) = 2.1$). Inset: Change of the volume filling fraction ϕ on increasing the displacement; the dashed line is a guide to the eye. Slab thickness: 6 a, single random seed.

5

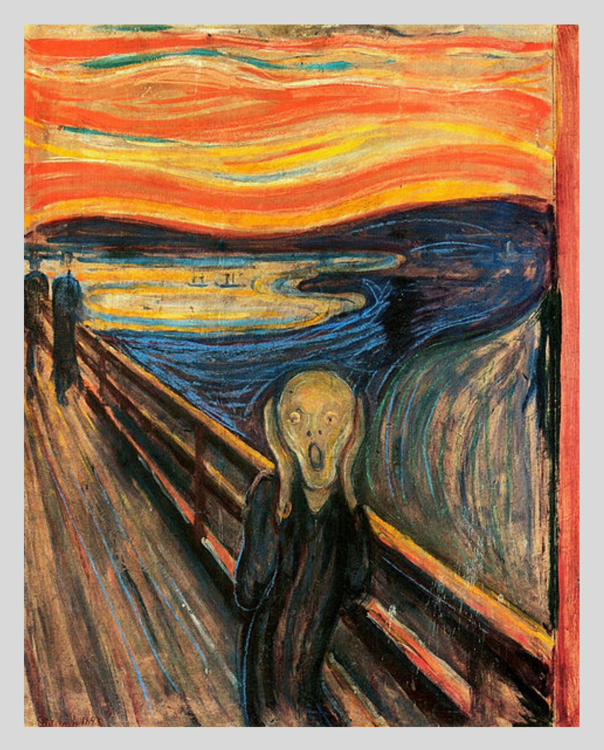

Distortion and Disorder on the Single Gyroid

Edvard Munch: «Skrik» (1893)

Overview

This chapter contains the *experimental part* (in the sense of evaluating a setup-simulation-analysis cycle) of this thesis: By presenting and interpreting reflectance data of the Gyroid PhC, several aspects of its chiral response, and the relation to distortion will be illuminated:

- A helix array (uniaxial crystal) shows substantially distinct (major CD) reflectance, but is not immediately comparable.
- Disassembly of the Helix Gyroid into its sub-families allows reflectance features to be related to distinct spatial orientation of helical elements of the Gyroid geometry.
- Finite absorption, esp. the respective view on CCR and CCT, will contribute to argumentation ways of penetration depth and effective CP-resolved attenuation.
- The effect of distortion correlation lengths on CCR variation shows in general a smearing and decline of CD strength, except for very-long-range modes:
- (Sinusoidal) “Chirp”: giving rise to distinct variation in reflectance CD behaviour, including (dependent on its pitch) doubling, or inverting its averaged CP reflectance difference.
- [001] reflectance and its distortion-induced variations will prove an appreciably robust against angular divergence of illumination (dependence on incident angle).

5.1. Uniaxial helix array crystals

As a preliminary work for the study of cubic systems, we studied systems of lower topological complexity, namely uniaxial helix arrays as those introduced earlier (sec. 2.3.4) by Lee and Chan [LC05] and Toader and John [TJ01].

Hexagonal and tetragonal lattices Starting point for the chiral structure of hexagonal (tetragonal) symmetry is the particular unit cell, and the choice of its uniaxial (c, by convention) axis as subject to transformation from proper 6 (4) rotation axis to a 6_1 (4_1) screw axis. This axis will be traced by helix made from a dielectric material. The resulting regular lattice is of space group $P6_1$ (No. 169: RCP helices, or $P6_5$, No. 170 in the case of LCP [Int04]) or tetragonal $P4_1$ (No. 76: RCP helices, or $P4_3$, No. 78: LCP [Int04]).

Note that for both hexagonal and tetragonal lattices, a “void” helix is found interleaved with dielectric, to form a helical vacuum channel of the same handedness as the helices themselves. (Be reminded of, within the Gyroid and its individual directions (namely, [111] and [001]), helices of multiple radii and opposite handedness exist, made of material, as well as void channels)

For the simple hexagonal (SH) helix array, a HCP-like two-atom basis (a “body centring”, distant 1/2[111]) can be introduced, reducing symmetry to the trigonal space group $P3_112$ (No. 153).

Herein, the rotatory sense of the helices is always chosen RCP, in order to match with those of the Gyroid handedness convention.

Hexagonal structures, large band gap (for a band structure, see references [LC05] and [Sab10]) Firstly, producing fig. 5.1 serves as a sanity check for the simulations (comparison with reference data). Additionally, the behaviour on lowering the dielectric contrast from 9 to the typical biological value

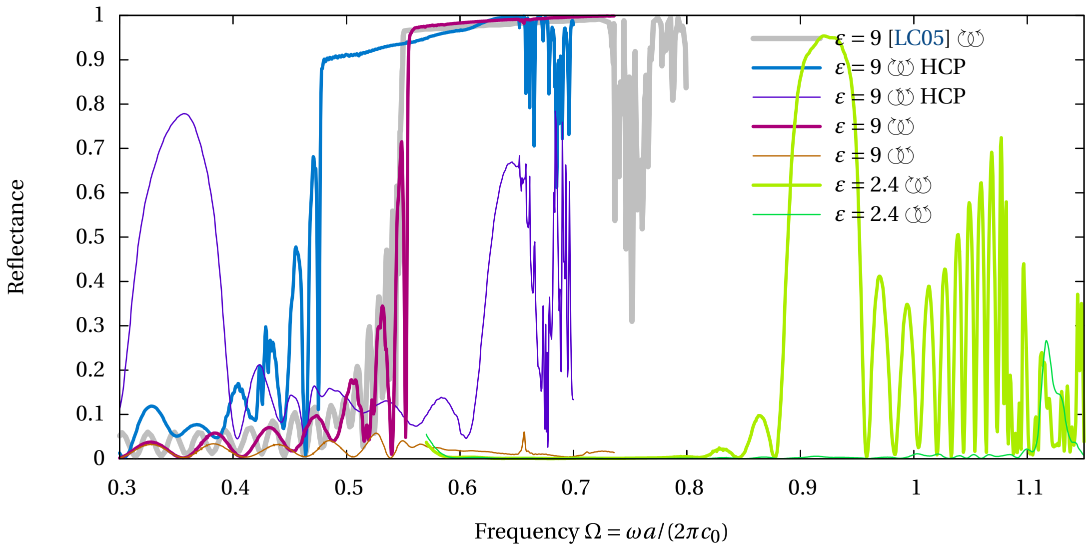

Figure 5.1.: (MEEP reflectance) Hexagonal helix array ($\phi = 15.2\,\%$ $c/a = 1$), reflectance, comparing different dielectric contrasts, and literature data. Note that here, the thickness here is 6.7 a for $\varepsilon = 9$, whereas in [LC05] and $\varepsilon = 2.4$ data it is 12 a, producing higher-frequency FABRY-PÉROT oscillations. Note that, for the primitive hexagonal lattices, the ↺ reflectance stays very low for all frequencies, whereas for the "body centred" HCP structure, ↺ reflectance exhibits its own distinct spectrum, even exhibiting a pronounced ↺-major reflectance at low $\Omega = 0.35$ frequencies.

of 2.4: the anticipated decrease of distinctness and blue-shift is clearly visible. The thickness had to be increased to 12 repetition units, still not reaching full reflectivity. CCR has not been computed, as reflectance is near-zero for ↺ light (CCR would merely display the width of the prevailing high-reflectance bands).

Compare this data (especially the near-complete absence of ↺ reflectance) to the data obtained for the normal Gyroid helices of sec. 5.3.1 (representing a body-centred tetragonal helix lattice, in essence): The disjunct simple hexagonal helices exhibit essentially ↺ reflectance only. For the Gyroid, the presence of perpendicular helix-resembling elements (enforced from cubic symmetry, or arising from reproduction by normal helices, esp. from body-centred basis duplication) is inevitable, and it shares with the HCP distinct ↻ reflectance.

The "good CD performance" has to be seen in relation to material/volume "investment": To obtain clear "band gap"-like reflectance in a disconnected-helix array PhC, the latter has to be substantially thicker than a Gyroid at same ε. Additionally, it comes at the cost to be *uniaxial*, *i. e.* not with the inherent freedom of viewing direction choice given by the Gyroid (Note that this *freedom of labelling coordinate axes* is *not* a kind of "isotropy" in the sense of an essentially angle-independent response, as the reflectance is, in fact, a non-trivial function of the whole solid angle).

Sinusoidal Chirp In anticipation of (and reference to) section 5.5, we will depict (sinusoidally) *chirped* helix array reflectance here (fig. 5.2). Somewhat different behaviour as in the more comprehensive treatment for the chirped Gyroid structures is found: The periodic grouping of chirps by initialisation phase is identifiable, but the overall behaviour is somewhat more uniform (especially for large chirp amplitudes), and more coherently differing from the undistorted structure. Gradually, the FABRY-PÉROT-like beats above $\Omega \gtrsim 0.96$ widen and grow together to form a wide-band gap like plateau, in resemblance to the single Gyroid's characteristic ↻↺ reflectance (fig. 3.8).

Irrespective of chirp amplitude, the phase has limited influence on the (frequency-averaged) ↻↺ reflectance. In conjunction with the reflectance (most clearly visible for $\sigma_r/a \lesssim 0.2$) not reaching unity, this hints at a substantial penetration of both CP polarisations into the PhC. This insensitivity of hexagonal helix arrangements is in stark contrast to the observations for the chirped (cubic) Gyroid, *cf.* sec. 5.5.

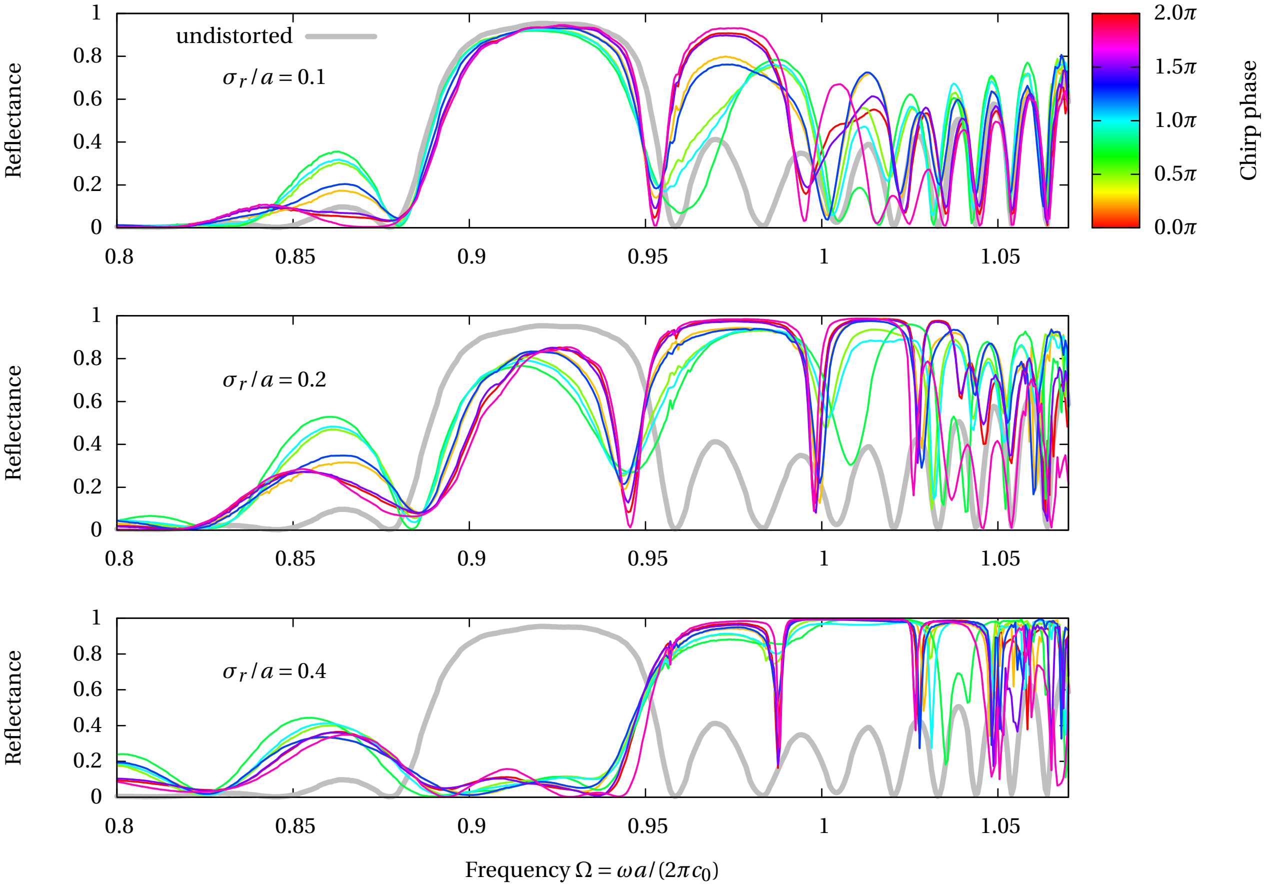

Figure 5.2.: (MEEP reflectance) Several chirp amplitudes σ_r imposed on the hexagonal helix array with dielectric contrast $\varepsilon = 2.4$, each in comparison with the undistorted signal (↻↺ reflectance spectra), thickness 12 a. In all cases, ↺↺ reflectance stays well below 10 %, thus not shown for clarity (see fig 5.1 for comparison ↺↺/↻↺). The length scale a equals both the lateral and normal hexagonal lattice constants (aspect ratio $c/a = 1$).

5.2. Distorting the single Gyroid

In structured media of full disorder (*i. e.* no spatial correlation between the scattering centres), one expects individual contributions of unorganised scatterers to dominate any inter-particle interference signatures, which require material arrangement in an ordered, collective manner. Crystal response is readily covered by PhC theory, and has been treated in sec. 3.4 Within this section, the gap between these extremal cases is investigated, departing from the single Gyroid as the limit of the perfect crystal.

5.2.1. The spatial frequency of distortion

The main rationale of the construction of "educated disorder" (as reported in chapter 4) is to control vertex displacements better than stochastic randomness. With the work done in sec. 4.3 (especially in subsec. 4.3.3), we hold tools for sophisticated tuning of the correlation length scales of a system. The different regimes divide, corresponding to the amplitude distribution within their respective reciprocal spaces, into

- Surface roughness (narrow spatial correlation/many very-high-frequency wavevectors)
- "Noise", high-frequency random distortion on the edge length/unitcell size scale,
- "Deformation/Distortion": collective distortion
- longest-wavelength modes: in effect modulated lattice constant, "chirp"

Two[66] reasons motivate distortions to be accessible with, in principle, arbitrary length scales:

At first, excess amplitude of long-range correlations impede nearest-neighbour distances less than short-range noise, leading to either a lower mismatch excess ϕ (for the helices, *e. g.*), or a more shallow increase of net wire length (within the unitcells of the network). In effect, low-frequency distortion make the volume fraction vary slower with increasing σ_r This is visualised in the inset of fig. 5.3.

Secondly, the distortion, being by construction wave-like, can be seen as a structure itself (with spatial periodicities on any length scale from the limit given by the model, up to the whole simulation box size), *i. e.* introduction of a new length scale, giving rise to interaction with the light. A haunting example is the (sinusoidal) chirp presented at full length in section 5.5.

With the main CCR graph in figure 5.3, the extent of amplitude distribution in reciprocal space is visualised, while keeping the distortion scale σ_r fixed. Note that, for $\sigma_r/a = 0.3$, the vast majority of amplitude is concentrated in only two modes, making the assumption of Gaussian-distributed distortion vectors more than questionable.[67]

---

[66] Actually, a *third* reason is the nodal approximation (*cf.* sec. 3.3.1) being a *continuous* function of space, necessitating a continuous way of representing distortion and noise, after all.

[67] Similar considerations, for the dubious results of random-seed averaging on a similar system, have in fact led to the discovery of the impact of chirp on reflectance.

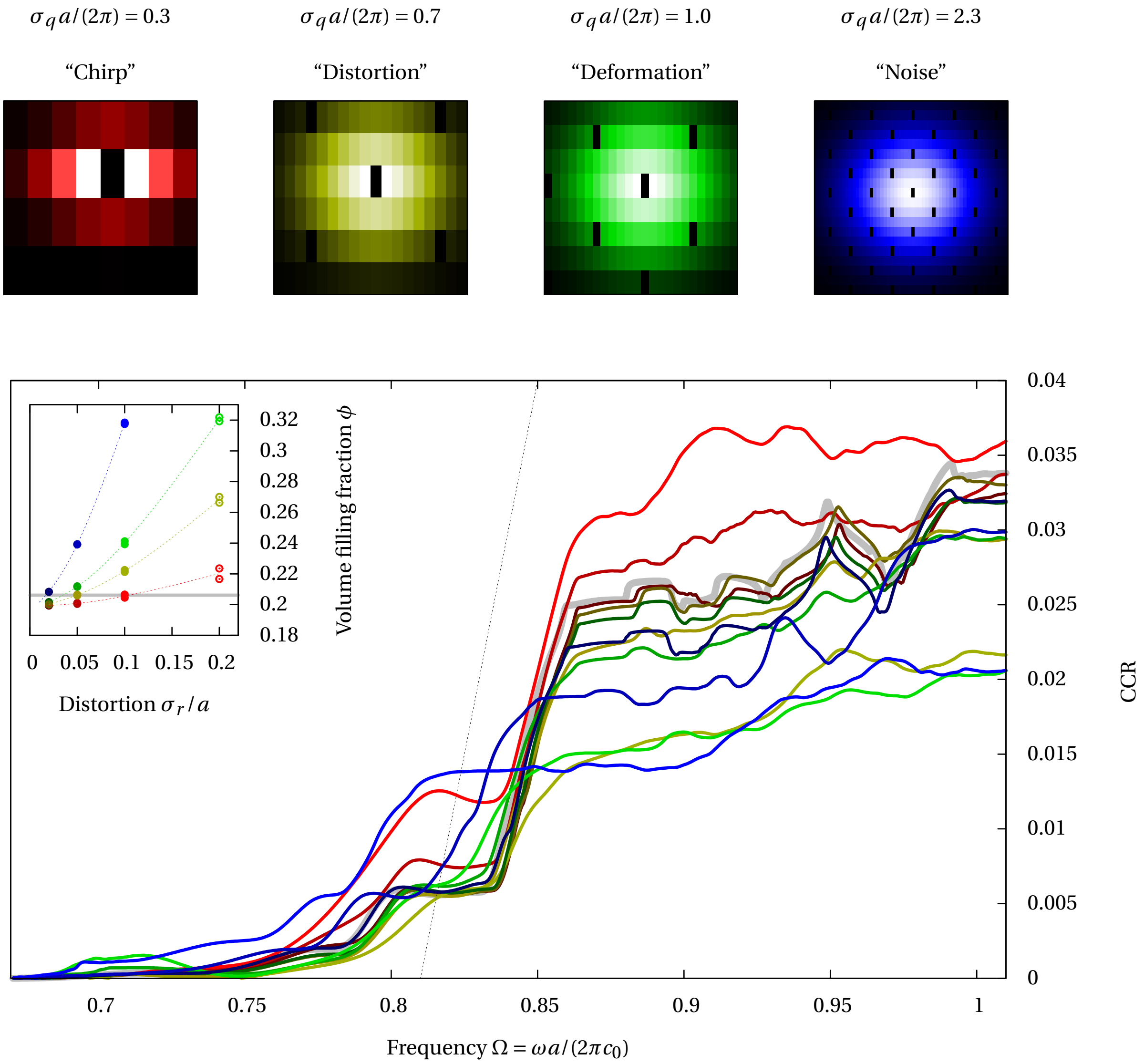

Figure 5.3.: (MEEP reflectance) **Main graph:** How the CCR response is qualitatively connected to the distribution width of wavevectors contributing to the distortion of real space: For different Gaussian distribution widths of distortion wavevector amplitudes (**upper pictures:** amplitude distribution over the supercell-reciprocal lattice sites, with zeroed-out BCC unit cell harmonics), reflectances are compared for distinct overall distortion scaling σ_r/a between 0 and 0.1 (CCR colour intensities proportional to σ_r, as in the inset). Data from single Gyroid **srs** network with four subdivision per edge, simulation box $2 \times 2 \times 6$ unit cells. For the underlying real-space structures, see fig. A.1 on page 110.

Graph inset: With increasing distortion scale σ_r, the volume fraction increases, as depicted in the inset (dashed lines guide the eyes in how the different correlation scales σ_q impact the volume fraction increase).

Imposing distortion causes circular dichroism of reflectance to out-level and decrease, except for the lowest-frequency distortions (red), in which the assumption of random phases is no longer valid (Note the few Fourier components with major contributions in the upper left image). This is further discussed in section 5.5.

5.2.2. Atoms-only Ball-and-stick network Gyroid

The network Gyroid has the additional degree of freedom of the relative size of *atoms* compared to the edges, tunable without losing symmetry. In the extreme ball-and-stick case of *totally disconnected spheres*, fig. 5.4, with a wire radius of $r = 0$, the undistorted structure exhibits reflectance close resemblance of the behaviour of its connected "relatives" (fig. 3.8).

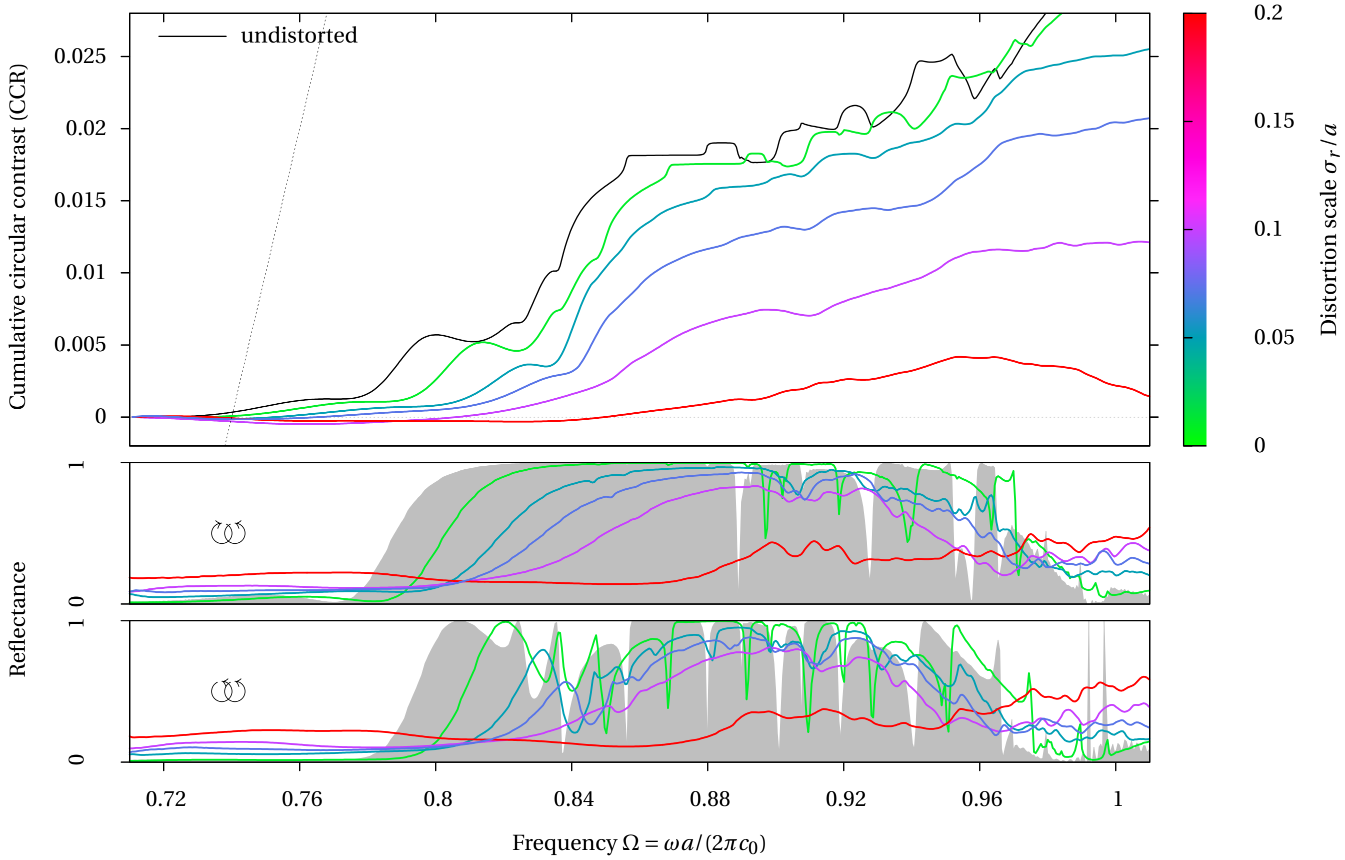

Figure 5.4.: (MEEP reflectance) **1srs** network Gyroid "balls-only" (zero wire thickness), inclined in [001] direction, $\sigma_q a/(2\pi) = 1.2$. Reflectance and CCR data in the undistorted case (grey) and some finite distortions (colours). This system exhibits a substantially higher sensitivity to distortion than connected Gyroid geometries.

But chiral response (alongside overall reflectivity) fades very rapidly at switching on even small real-space distortions $\sigma_r/a \gtrsim 0.1$. Compare this behaviour to comparable distortion scales in fig. 5.3.

5.3. Variations on the Helical Gyroid

5.3.1. Partial uniaxial Gyroid helix subsets with translational noise

Based on the idea that distinct 4_1 helices (and not all) might represent the relevant carriers of the Gyroid's chirality, we construct mono- and di-helical Gyroids (consisting only of the perpendicular, normal, and skew families of helices, where necessary, see the following text).

In section 3.3.3, the protocol to synthesise a Gyroid, coming from a helix aligned with a Cartesian axis, up to a structure with proper BCC symmetry, has been described in two conceptual steps:

1. Imposing the cubic symmetry constraint of the 3 axis in a $\langle 111 \rangle$ direction (page 39)
2. Explicit body-centred basis copy (page 40).

By varying the first step,[68] one can achieve a geometry, which preserves some aspects of the body-centred-ness (helix radius matching, tight connection, smooth surface) of the originating Gyroid,[69] while not necessarily keeping the cubic symmetry with its conceptual isotropy. This variation offers the introduction of distinctions between the three $\langle 100 \rangle$ directions, on the level of the geometry construction routine, and may consist of:

- Distortion scales different per axis, *i. e.* the real-space displacement of a helix is dependent on its orientation. Note that this is distinct from the possibility to create displacement vectors which are anisotropically distributed themselves (which are direction-discriminating on the general distortion request level).

  As a special case, by choosing a distortion scaling large with respect to lattice constants, selected orientations can be realised as a (Boolean, overlapping) "gas" without (perceivable) positional correlation: See sec. 5.3.2.

- Complementary, the wavelength distributions of distortion may be independently tuned, *i. e.* different helix displacement correlations per direction.

- Dimensional variations (wire thickness, helix radii, etc.).

- Omitting some of the orientation families completely, thus selective view on subsets of the Gyroid's screw axes.

  In principle, with dropping the cubic threefold rotation constraint (by omitting one or two of its copies) even in a case with zero distortion, one gains the uniaxial degree of freedom of the pitch-to-lattice constant ratio—enabling tetragonal lattice distortion. (This will not be covered in this work; let me refer to Pouya [Pou12; PV12] doing this for the single Gyroid).

This section 5.3.1 follows the last approach: Isolated view on helix orientation families of the Gyroid helix approximation. For all systems, helix wire radii were fixed at $r = 0.111\,a$, and the helix radius (for BCC matching) at $R = a/\sqrt{8}$. The distortion correlation length is chosen to an intermediate value of $\sigma_q a/(2\pi) = 1$, which reduces overlap mismatch between the helices (without introducing high-intensity multiple-unitcell density waves, as those implied by long-range distortion or chirp, see in section 5.5).

In comparison to the full three-family Gyroid (as of fig. 3.7), the initial overlap within a mono-helical "Gyroid" is much lower: the possible overlap count on a single undistorted helix family cannot exceed 2 for BCC basis, and is exactly one for SC helices, (*i. e.* a simple tetragonal helix array, *cf.* sec. 5.1). So the volume fraction will be far less dependent on the distortion.

Also note that, due to the lowered filling fraction, special care must be taken for proper comparison to the full Gyroid data (A change in ϕ is, of course, more than just a mere frequency shift). The evolution of volume fractions with increasing distortion amplitude σ_r is depicted in figure 5.6.

---

[68] The implications of BCC basis duplication have already been discussed on page 40 in section 3.3.3.

[69] Of course, in general, the resulting structure will share with the Gyroid only the (local) helix building blocks

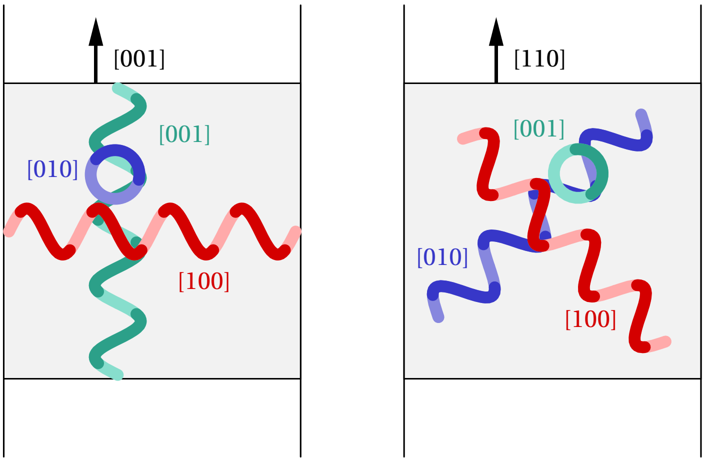

Figure 5.5.: Slab geometries for [001] and [110] inclination of the Helix Gyroid: Orientations of the three helix subsets (represented by single helices in different colours according to their position within the unit cube) relative to the surface/inclination normal, *i. e.* the direction of light incidence. In the [001] case, two thirds of the helices are perpendicular, and the remaining normal (parallel) to the inclination direction. For [110] inclination, one helix subset is perpendicular, while the angle between the skew helix families and light incidence is 45°.

Figure 5.6.: (Voxel counting) Volume fraction of Gyroid one-helix subsets, initialised with BCC (2 helices per unit cube) and SC (one helix per unit cube) basis, as a function of the amount of distortion σ_r. Data taken from all system situations whose reflectance data is shown in sec. 5.3.1. Deviations arise from random sampling statistics (explicit by seed, and different distortion vector sampling due to altering inclinations and supercell dimensions). Solid lines: guide to the eye. Right axis: Values for the “nematic gas” state at $\sigma_r/a = 5$, *cf.* sec. 5.3.2.

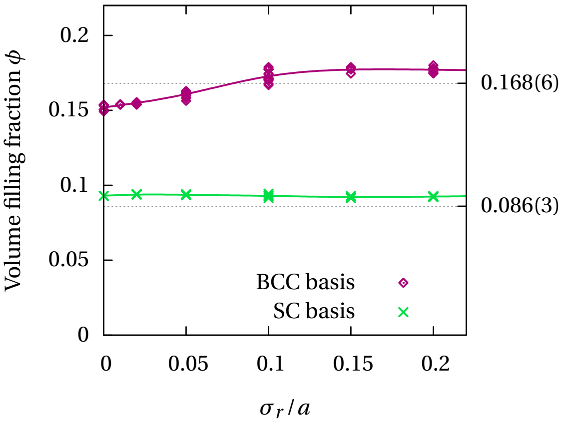

[110] direction: Distortion causing decline in reflectance, no CD

The helix subsets divide into two classes by their relative orientation with respect to the [110] direction chosen for the crystal inclination direction:

perpendicular [001] helices, forming a right angle with the surface normal,

skew [100] and [010], with an angle of 45° to the surface normal.

Figure 5.7 compares the reflectances caused respectively by both types of sub-helices, viewed isolatd, to the one of the BCC-helical Gyroid. The perpendicular helices show very low, but systematic ↻↺-major reflectance. The skew helix system remains essentially CD-free.

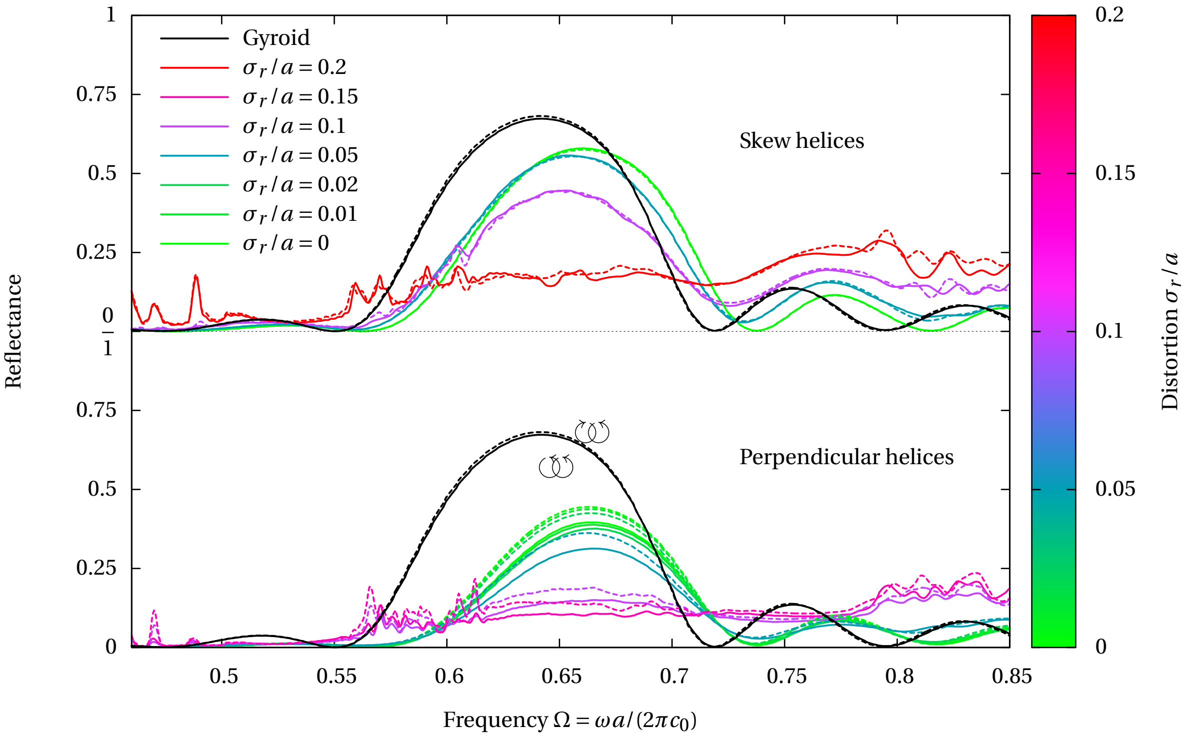

Figure 5.7.: (MEEP reflectance. Solid lines: ↻↺, dashed lines: ↺↺) The reflectance off an [110] inclined BCC-helical Gyroid is nearly CD free (black data, *cf.* sec. 3.4). Its helix subsets viewed isolated (coloured data; upper graph: skew lower graph: perpendicular with respect to inclination direction) remain essentially CD-free, while modest distortions $\sigma_r/a \gtrsim 0.1$ destroy the pronounced high-reflectance (Gyroid: partial band gap in the (primitive) Γ–N direction) signal initially present for both helix orientations. Note the blue-shift of reflectance due to lower filling fraction (ϕ depicted in fig. 5.6). Data from averaging over three random seeds at a slab thicknesses of 6 a.

At intermediate[70] distortions $\sigma_r/a \gtrsim 0.1$ destroy the high-reflectance (Gyroid: partial band gap in the (primitive) Γ–N direction) signal present in both helix orientations (while proving more robust for skew helices).

[001] direction: Separate band-edge mismatch and dichroic band

When [001] is chosen as the inclination direction, the Gyroid helix subsets can be classified into those distinct ways (see the sketch in fig. 5.5 for visualisation):

Normal helix axes aligned with surface normal,

Perpendicular either subset of [100] or [010] helices, or

Lateral (as a special case of the latter) with *both* directions occupied, thus overlapping to form proto-helical channels in [001] direction already, see sec. 3.3.3.

---

[70] See for example fig. 5.3 for the influence of a similar-amplitude distortion in [001] direction: Depending on σ_q, the CCR end-value declines to at most the half of its originial value.

Fig. 5.8 depicts the reflectances of those three situations in comparison to the full Gyroid, and subject to distortion; fig. 5.9 shows the according CCR. For small ($0 < \sigma_r / a \lesssim 0.15$) distortions, well-known features of the $\langle 100 \rangle$ Gyroid reflectance signal seem to become separable along the helix orientations, as depicted (besides the response to distortion) in figures 5.8 (reflectance) and 5.9 (circular contrast):

- The *lateral* helix family reflectance shares remarkable qualitative similarity with the full Gyroid, especially the dichroic band width. The lower band edges, however, exhibit an offset *reverse* to the Gyroid, *i. e.* the reflectance for ↺ light meets the order of unity at lower frequencies than for ↻ (more rapid red-shift), leading to a *negative* contribution to CCR cumulation—but *only* when distortion is non-zero! The red-shift compared to the single-helix families is most probably due to the higher volume filling fraction.
- A similar CCR/"effective handedness" inversion, though at higher frequencies, is visible for the *single perpendicular* oriented helices. Alongside, the ↻-major dichroic band exhibits remarkably broadness ($\Delta\Omega \approx 0.06$, *cf.* full Gyroid: $\Delta\Omega \approx 0.026$), but is limited in CCR impact due to its comparatively low contrast—Note that perpendicular helices don't even reach unity reflectance!
- While the *normal* helices show no sign of a distinct dichroic band gap (compare this to the situation of hexagonal helix arrays of sec. 5.1, where each high-reflectance seems decisively exclusive to a single CP-sense), the ↺/↻ band edges deviate from each other significantly, giving a second contribution to CCR, which is moreover both remarkably robust against distortion and develops the same effective band width as the perpendicular helix families[71]!

With increasing distortion, the general trend of a step-wise CCR decline develops (perpendicular orientations: up to total loss of chiral response, overlaid with some of the aforementioned CCR inversion; normal helices: comparatively stable up to $\sigma_r / a \gtrsim 0.1$ and then gradual diminishing), accompanying the smoothing of reflectance features. There is no hint of increasing broad-banded-ness of chiral response, apart from the softening of band gaps.

Simple-cubic basis

Another modification step for the helical model is, to omit the BCC-inherited basis duplication, leaving a simple quadratic lattice of touching helices to cut the slab from. The situation seen here (fig. 5.10) is remarkably similar to the one for BCC basis, though the following differences and similarities come up:

- Overall lowered reflectance, narrower bands, and smoother band edge regions, presumably due to reduced effective normal repetition count
- Blue-shift, due to lower volume fraction,
- perpendicular: Less pronounced ↻-major in dichroic band; no band-edge mismatch
- normal: even more substantial lower band-edge mismatch (partially due to ↺ not even showing a sharp band gap reflectance signal at all)
- normal, gas (fig. 5.11) ↻-major CD signal nearly equal for SC helices as for BCC ones, meaning a "higher material efficiency" (same CD response with few material).

---

[71] The accurateness of any of the three situations nearly exactly hitting the full Gyroid's final CCR is a striking, yet unexplained feature of its subsets. It seems that the cubic symmetry of the Gyroid is *not necessary at all* to let helical model subsets exhibit "isotropic" (*i. e.* the same in all spatial directions) CD response.

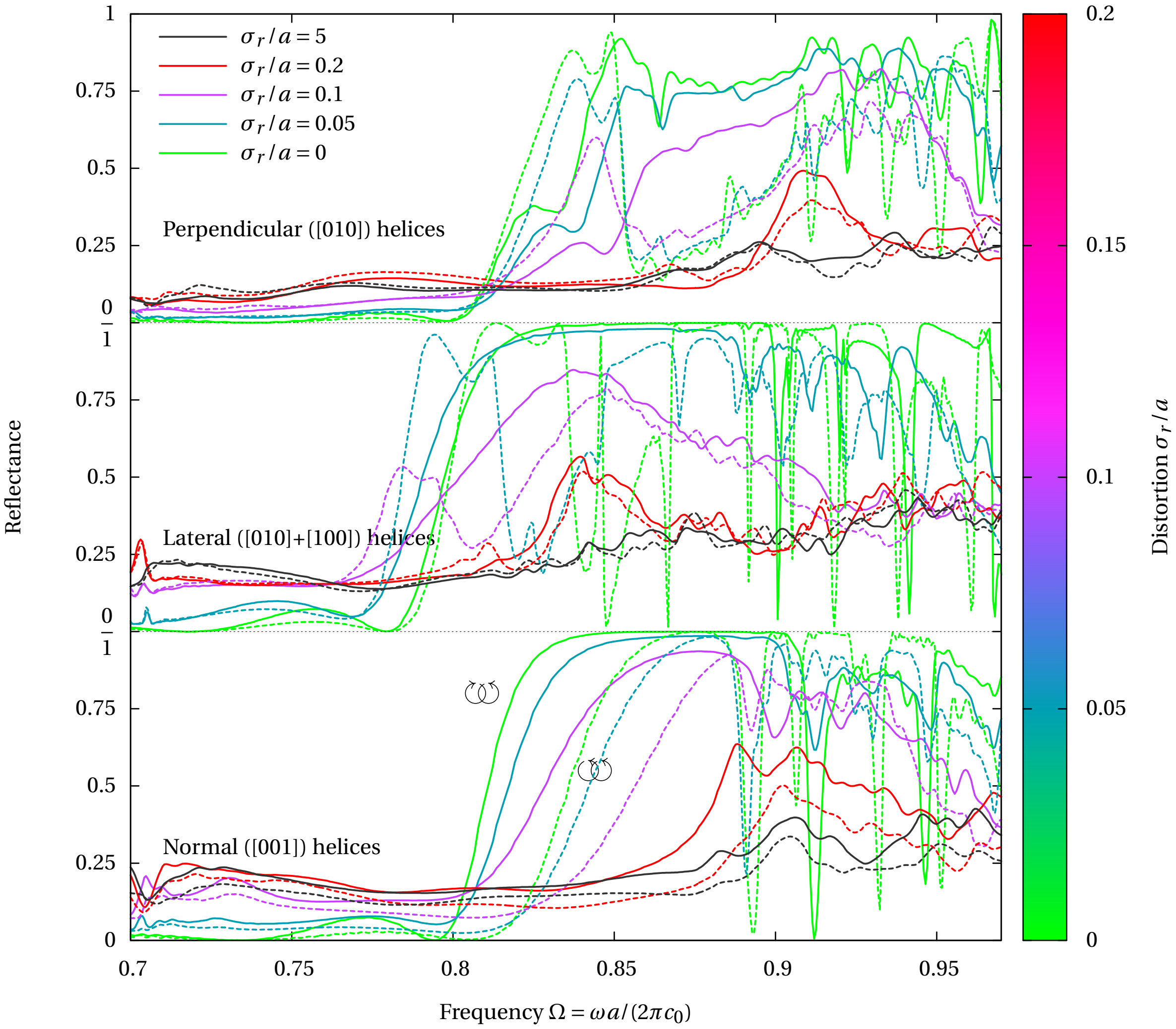

Figure 5.8.: (MEEP reflectance. Solid lines: ↺↻, dashed lines: ↻↺)) [001]-inclined BCC-helical Gyroid subsets oriented normal (lower graph) and perpendicular (upper graph; middle graph: both perpendicular orientations) towards the inclination direction, for different distortion scales, including total disorder ($\sigma_r/a = 5$, “nematic gas”, see sec. 5.3.2). For circular contrasts computed from this data, see fig. 5.9.

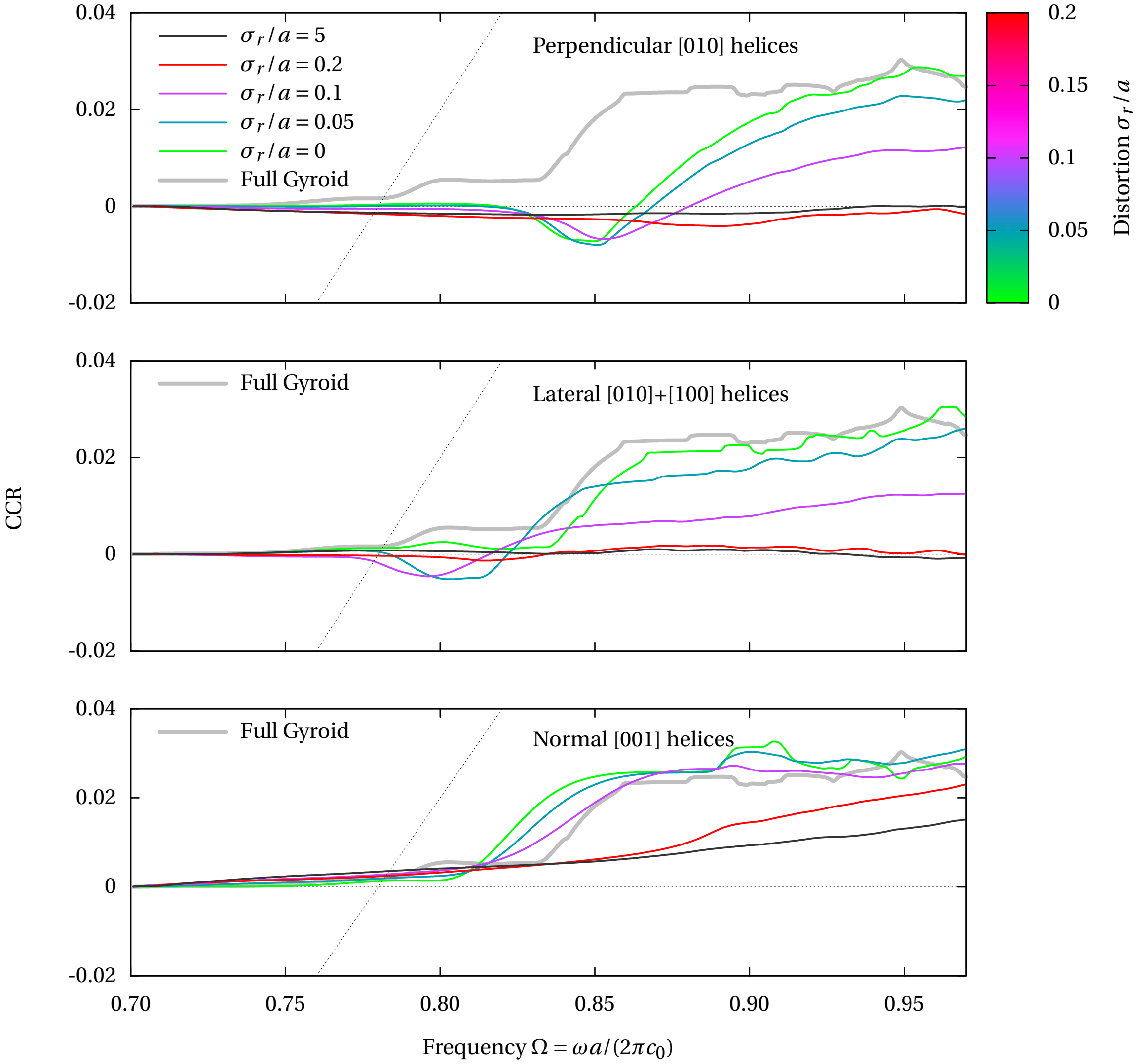

Figure 5.9.: (MEEP reflectance) Cumulative circular contrasts from reflectance off [001]-inclined BCC-helical Gyroid subsets with different orientations relative to the inclination direction, the same as in fig. 5.8. Variation of CCR with an increasing degree of disorder gradually destroys the circular dichroism of the medium, despite being built from helices. For reference, data from the full 6-helix-per-unitcube BCC Gyroid is drawn alongside.

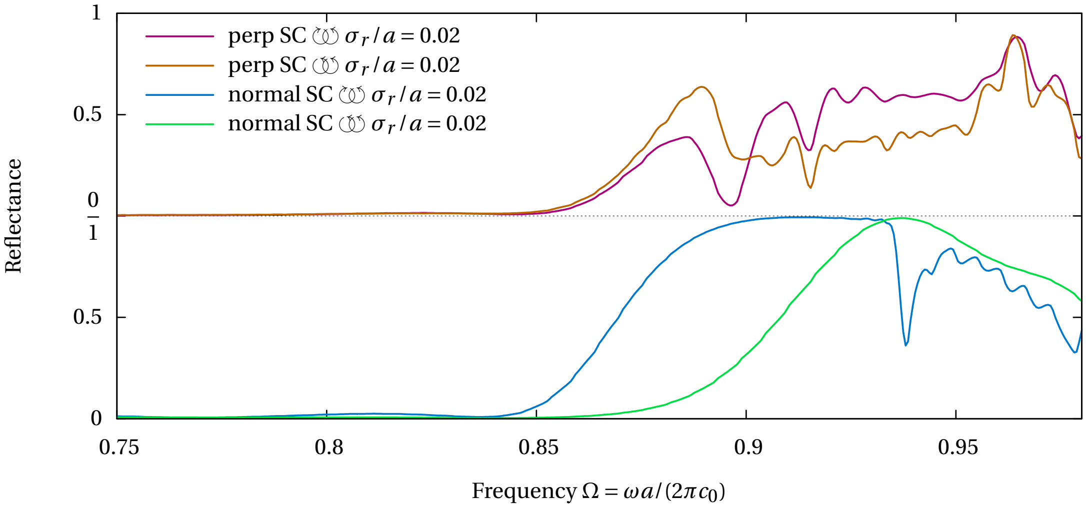

Figure 5.10.: (MEEP reflectance) [001] inclined SC helix families normal (helices along [001] direction) and perpendicular (helices along [010] with an angle of 90° to incident direction), at an exemplary weak distortion $\sigma_r/a = 0.02$.

5.3.2. Helix gases: "nematic" and perfectly disordered

This section compares different kinds of helix "gases" with each other (Gaseous in the sense that they exhibit no visible spatial correlation between their centres, constructed as the limit of high translational disorder distorted helix subsets[72]). Gases derived from the Gyroid sub-families are called *nematic*, as the translational disruption does preserve their relative orientation (which classifies the gases in the same groups as in sec. 5.3.1).

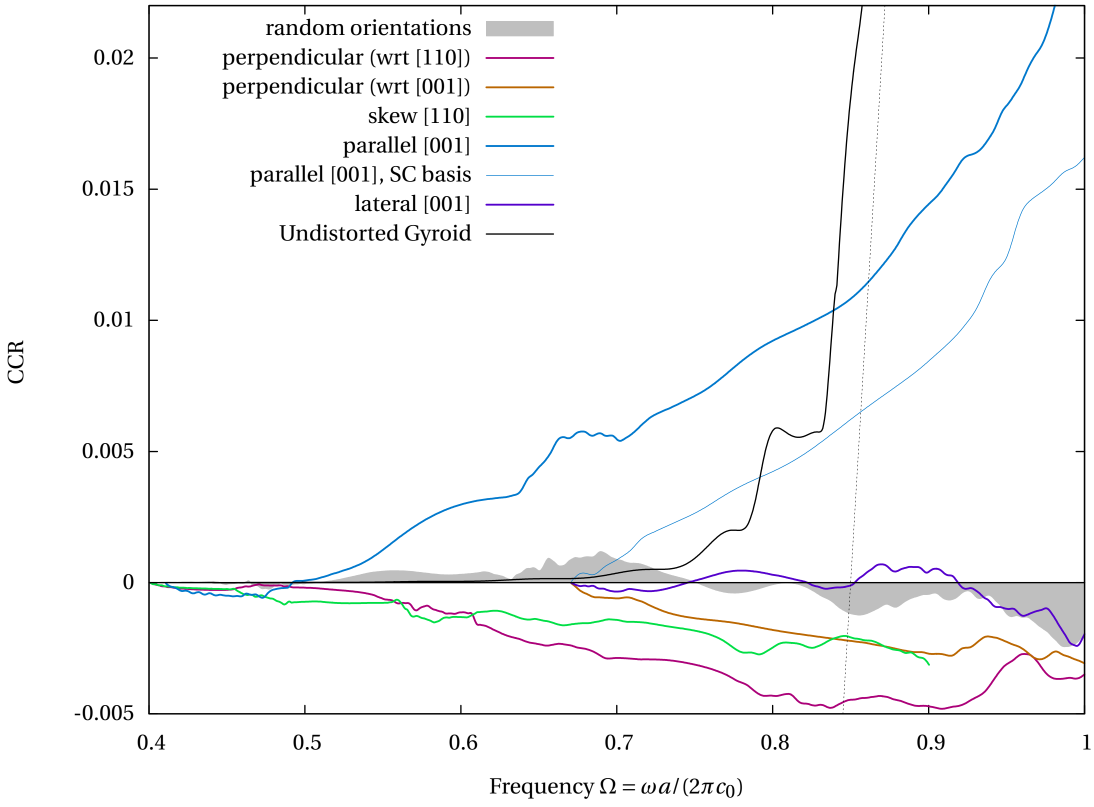

Figure 5.11.: (MEEP reflectance) CCR of nematic helix gases with different axis orientations, in comparison to a randomly-oriented gas, and an undistorted BCC-helical Gyroid. Note that, due to frequency window coverage, some CCR data begins at $\Omega = 0.67$, ignoring chiral response at lower frequencies.

Fig. 5.11 compares gases ($\sigma_r \gg a$) with a number density identical to [un]distorted Gyroids (volume filling has increased to $\phi = 0.167(6)$).

Despite of consisting from (highly chiral) helices, circular dichroism is—at least within the frequency interval (chosen by its feature-richness within the "proper" Gyroid)—not particularly pronounced (for normal orientation) down to negligible within noise (perpendicular).

As a reference, also a fully disordered gas (including full orientational randomness) has been tested

---

[72] Note this is a toy model, not feasible with bottom-up techniques like "shaking a box of fusilli noodles" (think of the substantial overlaps between most helices)

as a “dense-limit” dielectric “sugar solution model”. Despite consisting of helices, the native “building blocks” of handedness, the fully random gas shows up minimal CD response.

5.3.3. “Cross-over” to the Quadruple Gyroid

The **4srs** is a structure built from four **srs** networks of same handedness, interwoven in a way so that they do not intersect. The four networks are translational copies from a face-centred set of basis vectors, filling the half-integer lattice positions left free from the BCC symmetry of the network itself. The resulting structure exhibits *simple cubic* symmetry $P4_232$ (with a repetition unit length half the original lattice constant a of the single networks). Hence, its $\langle 100 \rangle$ directions are *primitive* directions of both real space and its associated reciprocal space, giving rise to a low-complexity band structure, and, in the case of chiral geometry, prominent CD properties (band gap forbidden for one circular polarisation sense, full LCP/RCP character of the Bloch modes). Thus, it has been subject to chrio-optical studies arising from its symmetry [Sab+11] (though at dielectric contrast as high as $\varepsilon = 12$, rather than the $\varepsilon = 2.4$ used here).

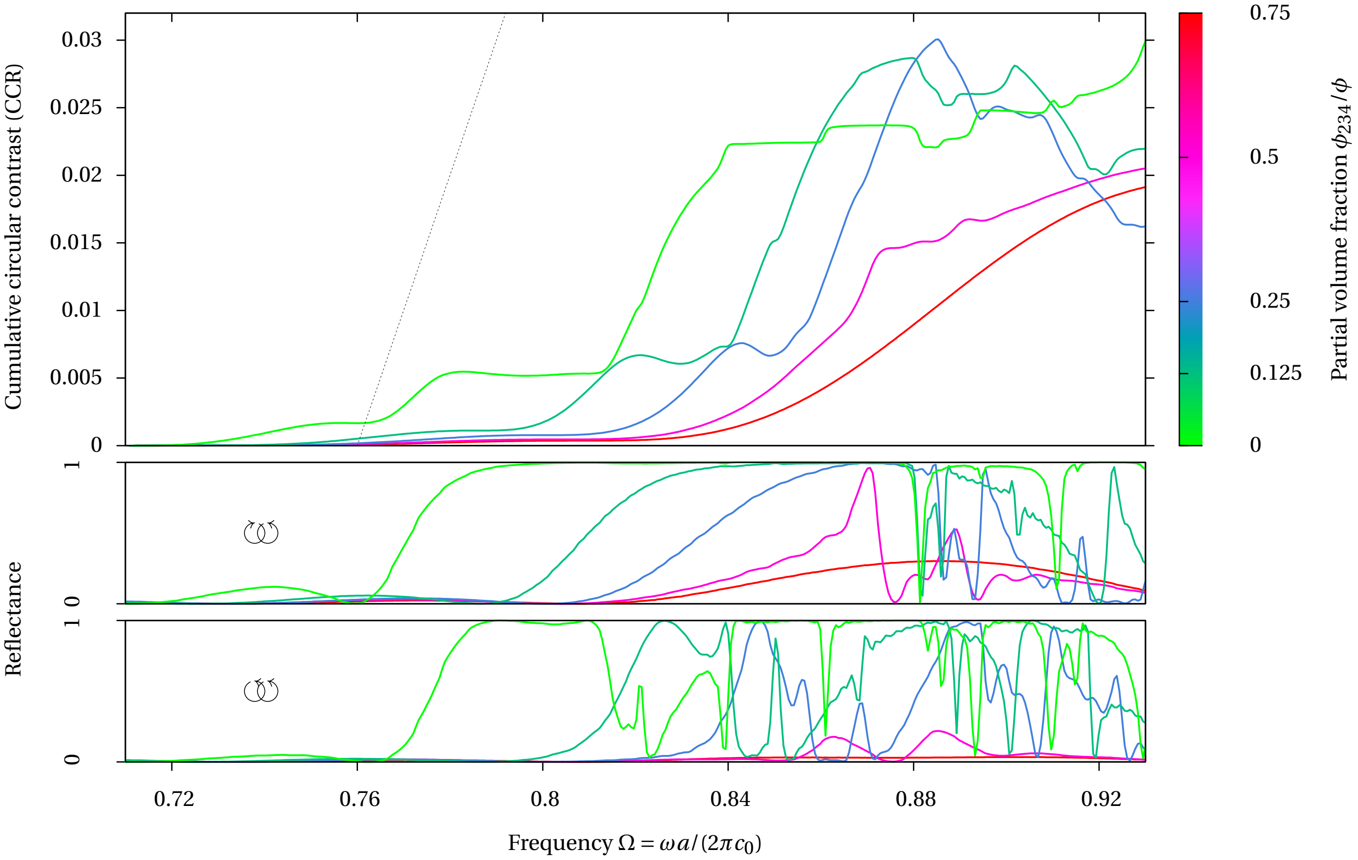

Figure 5.12.: (MEEP reflectance) Inflating three **srs** networks (summed partial volume filling ϕ_{234}) within the void channel of a **1srs** network Gyroid, to finally form a balanced **4srs** with $1/4 \cdot \phi_{234} = 3/4 \cdot \phi_1 = \phi$.

Slightly varying the wire radii of the distinct networks of the **4srs** will (besides destroying strict simple-cubic symmetry) not fundamentally change the photonic behaviour. But somewhere in between the **1srs** with three additional **srs** networks penetrating its void phase, and the **4srs** with distorted wire thickness, the behaviour must *cross-over*. Due to the mapping $\phi \mapsto r$ from sec. 3.3.2, this can be achieved at a constant-volume constraint, ensuring optimum comparability between the various realisations.

Figure 5.12 depicts this process. It is parametrised by the partial volume fraction ϕ_{234} of the three "new" networks (getting inflated to the disadvantage of the "old" network). Note that it is directly visible that the relative handedness of response is conserved (*i. e.* no CCR sign switch). While CCR amount and absolute reflectance decreases in both bandwidth and height[73], the dichroic band gap suffers a distinct blue-shift, while the associated shoulder actually increases in height, up to a maximum at $\phi_{234} \approx 0.2$.

5.4. Absorbance and Distortion

> This section is based on the work (and, partly, the data) incorporated into the publication [Sab+14], in collaboration with Matthias Saba, Bodo Wilts, and Gerd Schröder-Turk. It is appended to this thesis; see there for experimental and simulational index-matching procedure details, and a more comprehensive discussion on band structure, reduced CD measure, and biological implications.

One strength of FDTD (for crystals) compared to frequency-domain methods relying on plane wave expansion, is the seamless integration of absorptive losses (or gain, for a negative "loss") in material response, see section 2.1.5. In reality, the existence of material without loss is an idealisation, and at most valid for a confined frequency range.[74]

5.4.1. Absorption and frequency-dependent permittivity

For a medium containing a homogeneous density of absorbers exhibiting a Lorentzian line profile, the complex permittivity (introduced in sec. 2.1.5) $\varepsilon(\Omega)$ is described by the resonance term

$$\varepsilon_{\mathrm{L}}(\eta,\Omega) = \varepsilon + \eta\,\sigma_{\mathrm{L}} \frac{\Omega_{\mathrm{L}}^2}{\Omega_{\mathrm{L}}^2 - \Omega^2 - \imath\,\Omega\,\gamma_{\mathrm{L}}} \tag{5.1}$$

with the resonance frequency $\Omega_{\mathrm{L}} = 0.695$, the damping constant $\gamma_{\mathrm{L}} = 0.26$ and the resonance strength $\sigma_{\mathrm{L}} = 0.1117$ (with an absorption scaling factor η). The numeric values have been adopted from [Sab+14] to fit experimental data of *C. rubi* wing scales, by imitating the index-matching transmission measurements of butterfly wing scales by FDTD simulation of the idealised Gyroid structure at $\eta = 1$ with void (= immersion medium) ε set equal to the frequency-independent ε of the Gyroid material.

By introducing a frequency-dependent system contribution, one gains another set of parameters: resonant frequency, width, and coupling strength—at the cost of loosing the universal scaling behaviour (by introducing an explicit energy scale).

---

[73] Note that in the **4srs** study [Sab+11], the performance has been measured at the much higher dielectric contrast of $\varepsilon = 12$.

[74] That any material must have finite absorption somewhere in the electromagnetic spectrum is obvious both from the Kramers–Kronig relation [AM76], and the remark that all materials exhibit finite light absorption at least when the light frequency matches the electronic binding energies (photo effect).

5.4.2. Reflectance of the absorbing, undistorted single Gyroid

FDTD reflectance simulations were carried out on the undistorted, fixed $\phi = 20.5\,\%$ Gyroid created by its nodal approximation material function. The three high-symmetry directions of the BCC lattice were investigated. The [110] direction exhibits no CD response, so it is not regarded in this section.

Figures 5.13 and 5.14 depict the CP-resolved reflectance change with switching on absorbance, for [001] and [111] directions, respectively. As absorption relaxes the strict $R + T = 1$ flux conservation, circular contrasts of reflectance and transmission do no longer necessarily coincide. In fact, a gradual de-coupling of CCR and CCT is observed. The CD band-edge mismatch is suppressed by absorption as of $\eta \gtrsim 0.5$ for CCR, but enhanced (!) ↻ transmission, as seen in CCT of fig. 5.13.

What do CCR, CCT, and their difference, mean in the finite-absorption case, respectively? CCT compares how ↻/↺ (RCP/LCP) modes *couple into* the material, whereas CCR is sensitive to how easily waves are *reflected*.

[100] The increase in CCR can be traced back to the smearing-out of the dichroic band gap around $\Omega = 0.85$, which happens faster than the overall decrease in reflectance. The low (to be exact: zero) coupling of ↺ modes within the dichroic band gap causes them to be less susceptible to absorption than the ↻ modes penetrating the material. In contrast, at frequencies below the fundamental band edge, CCT exhibits an increase, depicting the opposite image: ↻ effectively penetrate the structure *less deeply* than ↺. Note that this effect persists far into the high-absorption regime.

[111] This totally different situation is shown in fig. 5.14: At a first, remark (contrary to [001]), the reflectance features of [111] inclination exhibit a *red-shift* on increasing η. CCR proves to a much higher extent sensitive to absorbance than in [001] direction, halving in effect at a mere $\eta = 0.2$. This mirrors a much longer effective penetration depth. Contrary, the CCT transmission signal witnesses an *inversion* of circular contrast, so the presence of absorption reveals (disturbs) a subtle equilibrium in high ↻/↺ transmission. We may refer to the finite-angle data of sec. 3.5 (esp. fig. 3.9) for another view on the [111] direction, showing up additional features on switching on $k_\parallel$.

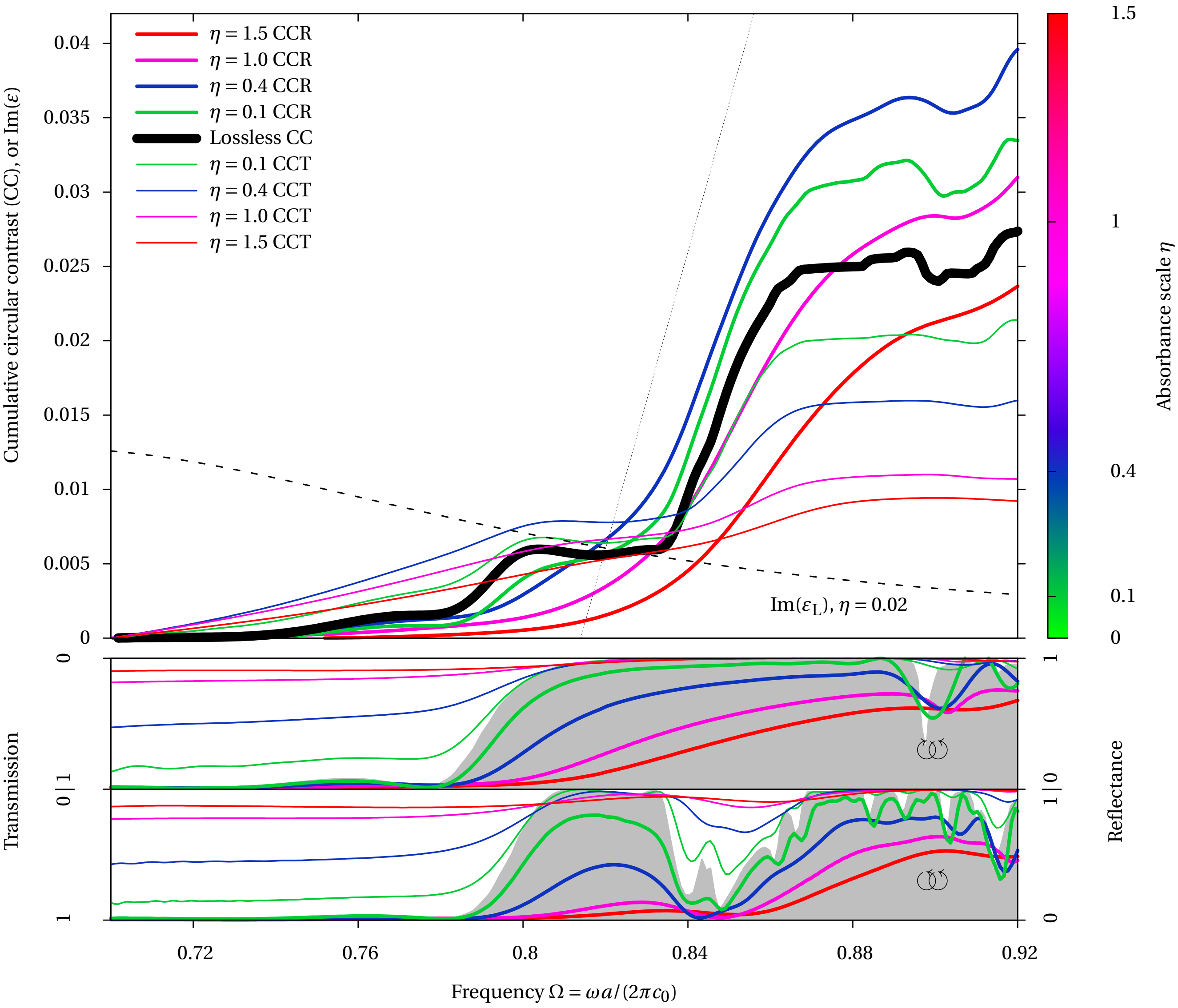

Figure 5.13.: (MEEP reflectance) Both CC measures of reflectance (CCR) and transmission (CCT) for an undistorted single Gyroid (from nodal approximation, $\phi = 20.5\,\%$, $\varepsilon = 2.4$), with finite LORENTZian absorption (strength parameter η, resonance frequency $\Omega_L = 0.695$ outside the plot range). Reflectance data with thick lines, transmission with thin lines. Note that, opposed to overall intensity loss (absolute reflectances/transmissions: see fig. 7 of [Sab+14]), CCR increases at modest absorbance scalings $\eta \approx 0.4$, indicating an effective broadening of circular-dichroic response. The dashed line indicates the imaginary part of the LORENTZ profile, eq. (5.1), which is directly connected to the absorbance by eq. (2.20).

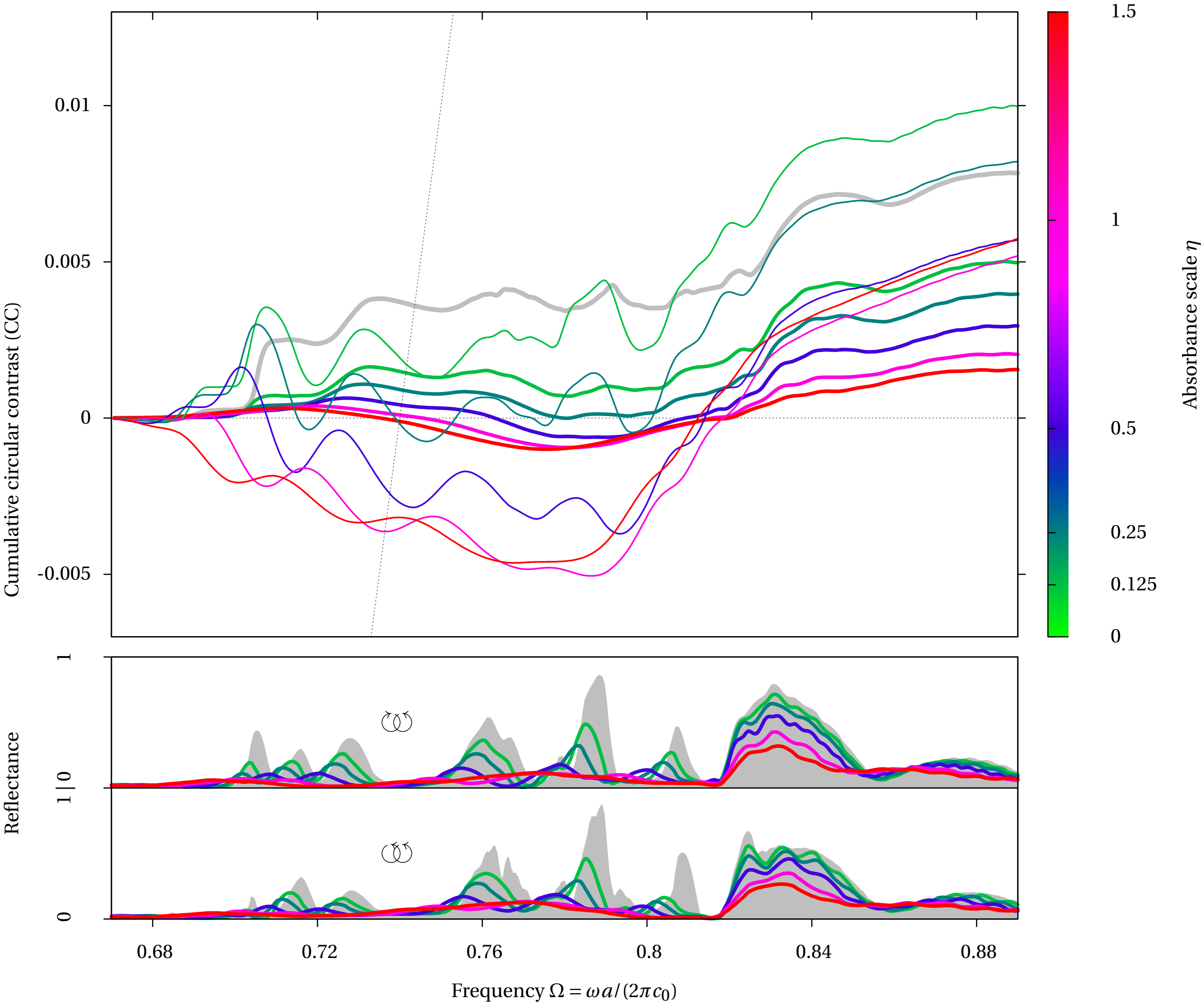

Figure 5.14.: (MEEP reflectance) Switching on LORENTZian absorption ($\eta > 0$ from eq. (5.1)) within the solid phase of the **1srs** network Gyroid, inclined in [111] direction. Reflectance data, cumulative contrasts of reflectance (CCR, thick lines) and transmission (CCT, thin lines), compared with lossless material (grey).

5.5. (Sinusoidal) Chirp

Once, with increasing real-space correlation length, the number of wavevectors of major contribution to total distortion becomes small, averaging over realisations by seed statistics gets difficult, or rather questionable: The approximation of any space point being displaced by the distortion field by vector of random length and orientation, and, more importantly, with a spatially isotropic correlation length scale (unless otherwise constructed), breaks down.

For the extreme case of a “monochromatic”, normal-longitudinal (distortion wavevector and polarisation vector within inclination direction), low-frequency limit, distortion resembles (on a length scale of a fractional part of the distortion wavelength) a *chirp*, *i. e.* a continuous variation in the (normal) lattice constant, or, in terms of the helical constituents of the Gyroid, a *pitch gradient*.

Due to its construction by the smallest possible wavevector commensurable with the simulation box, it will be, in effect, a harmonic of the slab thickness, hence *sinusoidal* in profile.

This case can either be witnessed accidentally[75], or explicitly constructed. The distortion of any requested point is proportional to $\cos(2\pi z/L_z + \varphi)$ (z: depth coordinate of the point relative to the slab surface), introducing as a new system parameter the *chirp phase* φ. Depending on φ, chirp influences *local* point density[76] in different ways (Note that the nomenclature refers to the density *at the surface*, rendering the distinction appropriate only with the assumption of *high reflectance*, *i. e.* typical penetration depths less than quarter of the distortion wavelength):

Loosening chirp ($\varphi/(2\pi) \approx 0.25$) Density is highest at the surface, and gradually loosening with descending into the material (*cf.* fig. A.2)

Compacting chirp ($\varphi/(2\pi) \approx 0.75$) The density increases from the lowest point at the surface into the PhC

Indifferent surface, towards density maximum/minimum below the surface ($\varphi/(2\pi) \approx 0$ and 0.5, resp.), and mixed with any intermediate combination of the two latter.

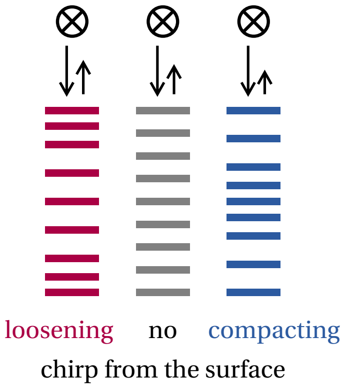

Fig. 5.15 and 5.16 show the chirp dependence of reflectance and CCR for the network and the nodal Gyroid, respectively, and for different chirp amplitudes. Though the response of the nodal Gyroid shows up more distinct and feature-rich than that the network data, in the overall behaviour, they equal each other.

Visible effects For ↺↻ reflectance, mainly the lower band edge is affected (in a rather smooth, monotonous way by either “inserting” or “removing” half a Fabry-Pérot maximum) by altering the chirp phase, resulting in markedly different CD behaviour at frequencies around the band-edge mismatch

---

[75] This way, the impressive impact of these kind of distortion has been discovered during the work on this thesis

[76] The effective coordinate stretching is not necessarily synonymous with an increased volume filling fraction. For the nodal approximation, *e. g.*, the density of sampling points applied to the void channel is increased in the same way as for the solid channel, holding ϕ essentially constant, irrespective of applied distortions.

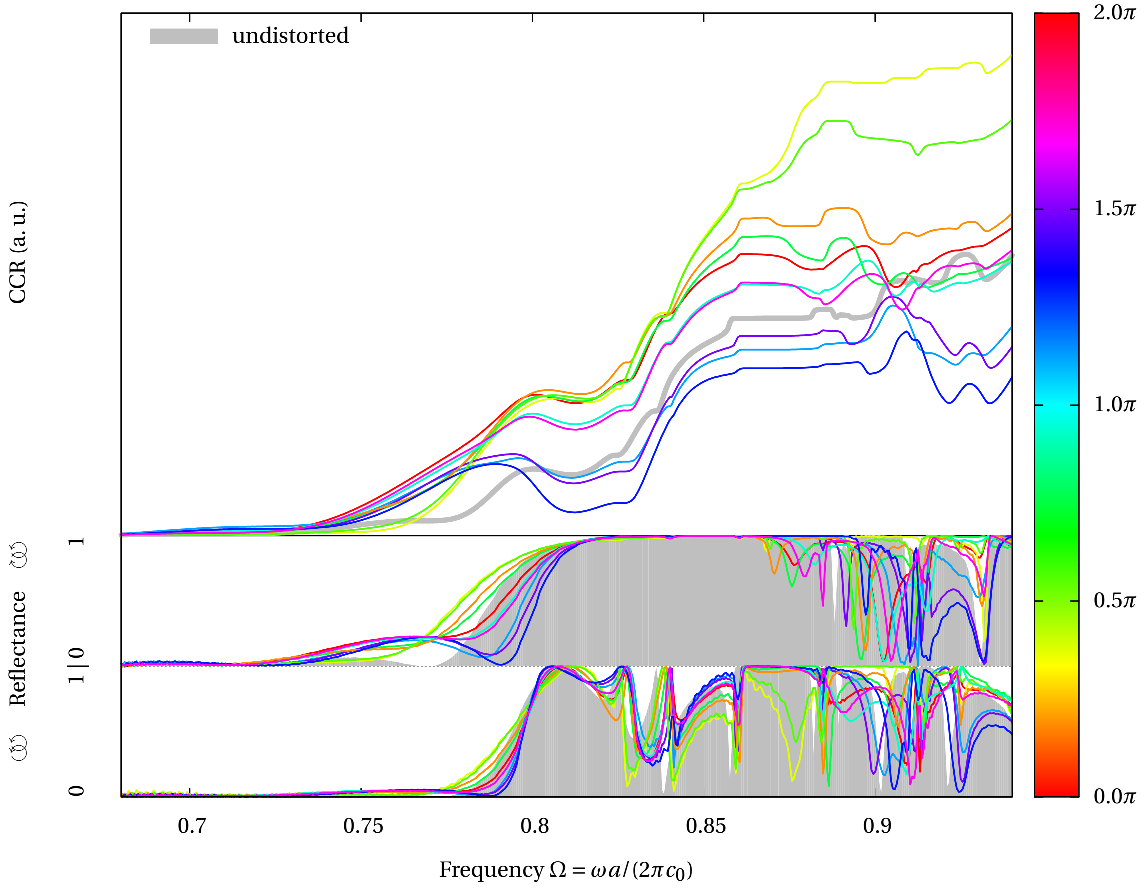

Figure 5.15.: (MEEP reflectance) (Sinusoidal) Chirp: Single-mode distortion by the lowest supercell harmonic, superimposed on the network Gyroid. Lower graphs: [001] reflectance, upper graph: cumulative circular contrast, each indicating its phase difference from a cosine function (0 refers to the lowest density/most extremely stretched lattice constant at the surface; $\pi/4$ "loosening": surface undistorted, starting with moving points away from the surface; π: starting with the highest density, etc.). Reference data in grey shows the signal from the undistorted Gyroid.

($\Omega \approx 0.78$). For some chirp phases, even a *optical handedness inversion* appears (similar to what has been witnessed before at the lateral helix subsets).

➿ reflectance reacts very sensitive to the phase, qualitatively altering behaviour: in the loosening case, CCR reaches nearly double as high as the one of the undistorted case, caused by a markedly higher ➿ transmission in the region $\Omega = 0.83 \cdots 0.88$.

For compacting chirp, a narrow dichroic band (with a handedness "opposite" to the dichroic band known from the undistorted Gyroid) causes ➿ to *dominate* overall reflectance (steep downward slopes of the blue curves in fig. 5.16).

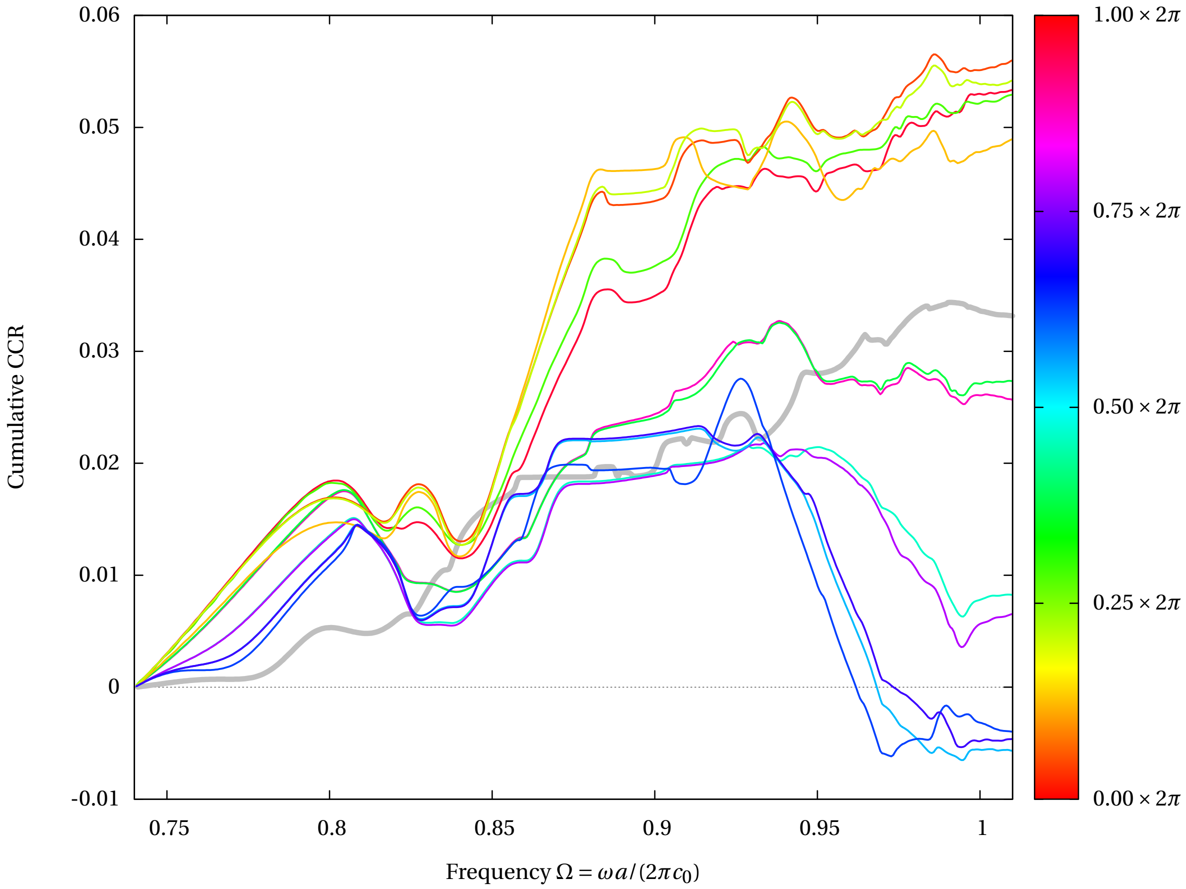

Figure 5.16.: (MEEP reflectance) Full phase-sweep scan over a single chirp amplitude $\sigma_r/a = 0.24$ of the nodal Gyroid in [001] direction: cumulative CCR data showing strong dependence of chirping slope on circular character of reflectance. For a small range of selected phases in the compacting-chirp regime around $0.65 \times 2\pi$, the CCR even runs to negative values (frequency region with pronounced ↺ transmission and ↻ reflectance).

On the causes As the Nodal gyroid is—in contrast to the network or helix Gyroids—preserving local volume density under distortions, the distinct data for the nodal Gyroid reliably exclude the explanation that the observed chirp dependence might be a mere effect of varying volume fraction.

From the known properties of the undistorted Gyroid PhC response and the given "experimental" reflectance data, reliable conclusions of chirp dependence may state that

- Chirp is a distortion of sufficiently low-frequency not to give rise to out-levelling observed on random distortions (as seen in the previous sections).
- Chirp improves coupling of CP light into the known low-coupling bands[77], namely dependent of phase: compacting chirp will improve ↻ transmission while impairing ↺ coupling (↺-major

---

[77] In the awkward approximation that band structure stays essentially intact on imposing the chirp.

character of CCR will be lessened up to inverted), whereas loosening chirp greatly enhances ⟲⟲ transmission, hence overall CCR rise.

Reflectance at finite incident angles Eventually (for the [001] direction), chirp effects will be investigated with respect to tilting the incident light to a finite incident angle against the surface normal/inclination direction. Figure 5.17 collects the (non-cumulative) colour-coded circular contrast maps, of two azimuthal angles and the two extreme chirp cases, respectively.

The high-CC impact of loosening chirp parallels the softening of the band-gap itself (together with the red-shift due to the enlarging real-space periodicity), proving similarly robust against tilting. Rather differently, the "wrong-handedness" reflectance domains (red areas, largely based on band-edge mismatch) prove sensitive to finite incident angles, totally disappearing at $k_\parallel a/(2\pi) \gtrsim 0.1$.

In conclusion, the CCR *benefits* of chirp (loosening) are pronouncedly more angle-robust than its *detriments* for compacting gradients. So, no control over the chirp phase (see, *e. g.*, fig. 5.3) will lead to, at least under incident angle averaging, an *increase* in CCR.

5.5.1. Chirp along [111] direction

At a first, note that chirp wavevector is defined as the (001) amplitude within the *orthorhombic supercell lattice*, *i. e.* directing in cubic [111] when inclined in this direction; consequently, the "same" chirp for different directions does not describe the same system; in other words: this subsection is not directly comparable to the effects seen in the former.

The qualitative appearance of reflectance—a series of narrow-band peaks up to $\Omega = 0.82$, followed by a near-achiral low-coupling band—undergoes only minor changes (such as an increased reflectance in this low-coupling regime), *cf.* 5.18. The overall chiral response stays negligible when compared to the [001] direction, with all chirp phases but a narrow interval around $\varphi/(2\pi) = 0.5$, exhibiting systematically more pronounced ⟳⟲-major reflectance peaks, leading to a significant (but in absolute terms still small) CCR end-value.

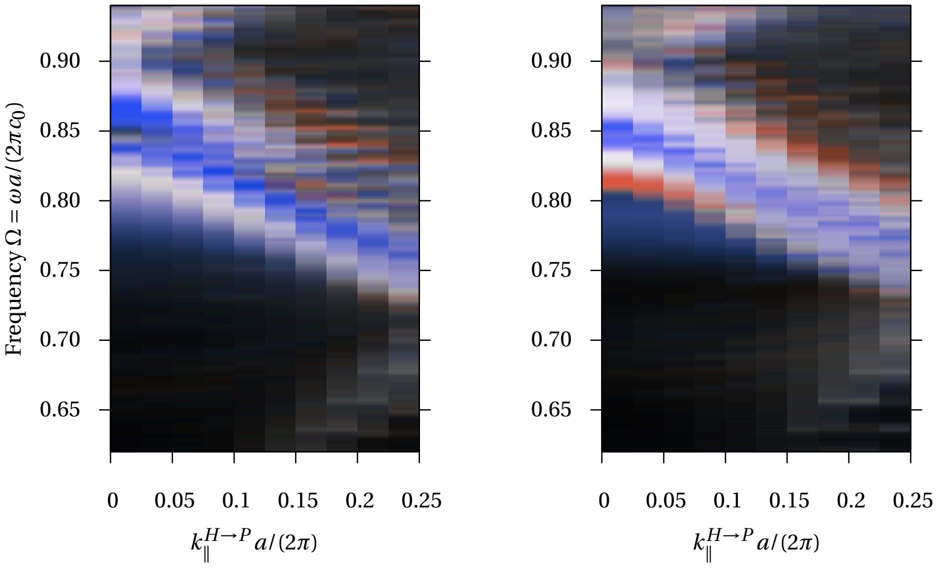

Loosening chirp $\varphi = 0.25$

Compacting chirp $\varphi = 0.75$

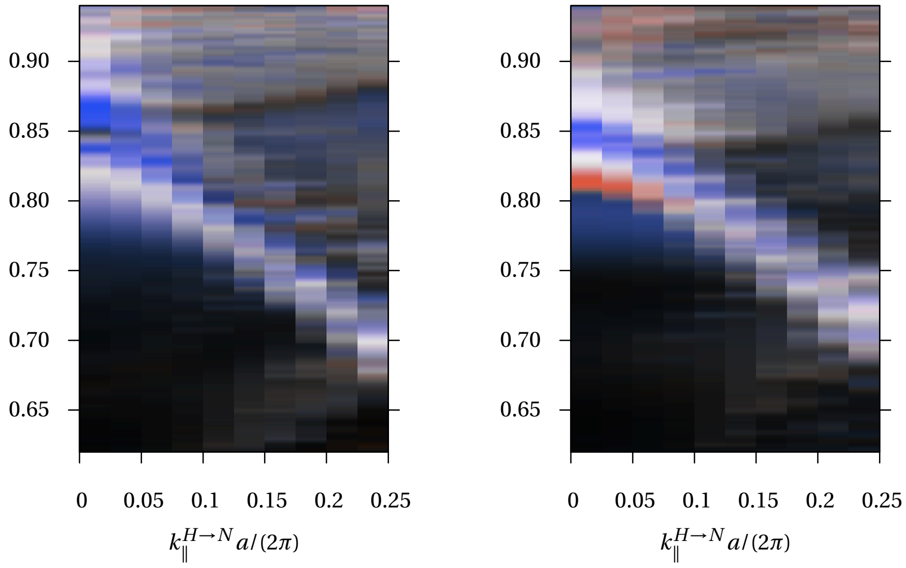

Figure 5.17.: (MEEP reflectance) Angle dependence of CP-resolved reflectance (red: ↺↺-major, blue: ↻↻-major reflectance) for a chirped (amplitude 0.2 a) network Gyroid with additional noise distortion ($\sigma_r / a = 0.05$, $\sigma_q a/(2\pi) = 0.7$). Rows: azimuthal viewing angles, each at a chirp phase of loosening (left column) or compacting (right column) distortion density beneath the irradiated surface. Compare with fig. 3.9 on page 46 (also, for details to $k_\parallel$ directions).

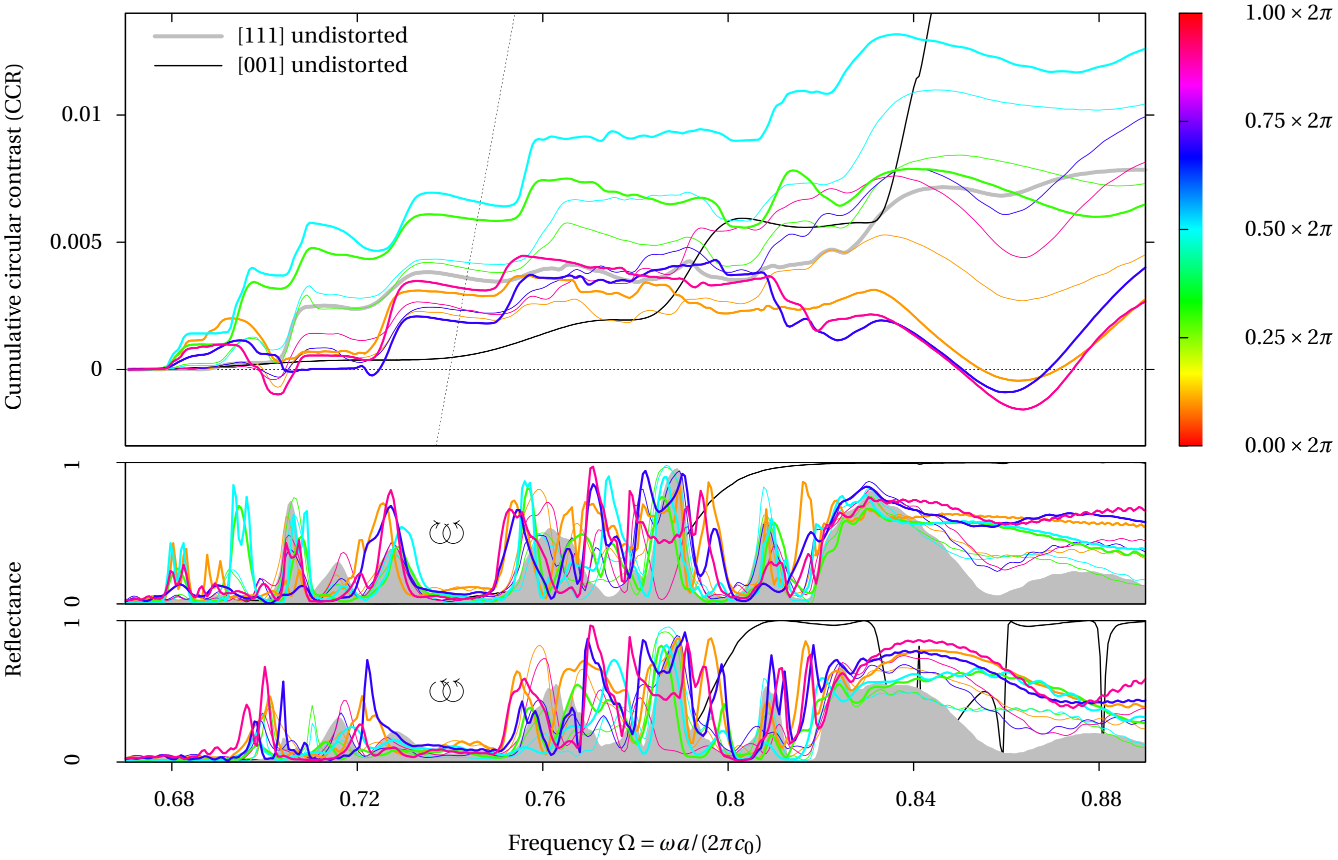

Figure 5.18.: (MEEP reflectance) Chirp imposed on a **1srs** network Gyroid, inclined in [111] direction. Reflectance and CCR data from the undistorted geometry (grey), with $\sigma_r/a = 0.1$ (thin lines) and $\sigma_r/a = 0.2$ (thick lines), colouring encodes the sinusoidal chirp offset phase. In addition, data from the undistorted [001] shown, to depict the relatively weak CD in both the perfect and the chirped [111]-inclined situations.

5.6. Discussion: CP reflectance of distorted chiral structures

For the discussion of polarisation-dependent CP light response of a medium determined solely by its *geometry*, the detail-concealing approaches of (effective-)medium descriptions (as the intrinsic chirality of continuous media, see sec. 2.2.2) do not suffice. Neither can, in this case of all-dielectric systems (opposed to, *e. g.*, plasmonic metamaterials), the *currents* on the "structure-photonic" or smaller length scales, be used to describe and interpret response. Hence they restrict the analysis vocabulary to (self-contained) *true "field-only"* treatment.

Note that the single Gyroid exhibits, in [001] direction, a ⟳-major *reflectance* and a ⟲-major *transmission*: light of the same handedness of the Gyroid is transmitted *preferred*, in contrast to the behaviour of cholesteric structures (see sec. 2.3.3), but in agreement with helix arrays.

Length scales of distortion

Least correlated randomness For a totally random structure, one expects finite reflectance with weak frequency dependence (ensemble averaging over "Mie-like" scatterers). This "short-range correlation" case has been approached with the multiple-subdivision network Gyroid, with the distortion scale as the parameter to switch between small noise-like distortions and "scrub", solely having topology in common with a Gyroid crystal (see real-space fig. A.1). In essence, the local disorder between single subdivision vertices conceals potential chiral response of the Gyroid arising from medium- and long-range regularity.

Another special case of neglecting correlation is for helices—whose "distortion length" does only scale down to their extent limiting from rigidity—given by the "nematic gas", where (in the case of the normal gas, *cf.* fig. 5.11) their local handedness accounts only to a minor extent reason for the chirality of the ordered structure.

Long-range correlations: Chirp Long-wavelength distortions with wavevector and polarisation along inclination direction substantially alter the *amount* of reflectance over the spectrum, without changing the *frequency* positions of the respective signals (*i. e.* band edges, resonances, etc. stay essentially fixed).

Subsequently they impose no fundamental *qualitative* changes on real-space field–structure interaction (possibly making them a promising subject of semi-analytic perturbation theory), rather they mainly *change the coupling* of CP vacuum modes into the nearly-crystal (increase/hinder transmission into/out of the structure). It be subject to further research to trace this behaviour, *e. g.* by comparing (at frequencies identified by this work, $\Omega = 0.88$ or 0.97 as examples) PhC Bloch eigenmodes to FDTD field patterns, to identify and isolate its underlying mechanisms.

About the origins of single Gyroid's PhC features

The helix Gyroid model allowed to separately study the contributions of the Gyroid's respective helical geometry elements, resolved by their orientation to the normal/inclination direction (sec. 5.3.1). Indeed, we identified for the [001] inclination a separation of band gap mismatch CD (most prominent for the helices in normal direction), and the CD arising from a pronounced dichroic band (for laterally oriented helices). For undistorted structures, all three cases reach essentially the same CCR final value as the Gyroid (fig. 5.9).

Both effects are combined in the cubic Gyroid spectrum. Their construction by uniaxial structures help to identify the underlying geometric principle giving rise to the observed behaviour: The existence of the dichroic band gap, backed by the band structure, is on account of lateral helical elements, whereas the existence of normal-oriented helices cause a broader ↻↺ reflectance band gap (even more clearly seen for the SC basis), in agreement with the optical handedness of the hexagonal helix arrays.

Absorbance and effective penetration depth Finite absorbance allows indirect probe-assisted penetration depth heuristics: revealed by difference between CCR and CCT. The smearing–broadening of the [001] Gyroid dichroic band gap by absorbance has already been described in [Sab+14], and gets backed by the observations for CCR and CCT. The Gyroid shows "real", non-trivial circular-dichroic dispersion: The CP modes, exposed to the chiral structure with finite real-dielectric contrast, are subject to an increase (↻↺) or decrease (↺↻) of effective absorbance around $0.78 < \Omega < 0.83$, stronger than predicted from the solid-medium absorbance from $\mathrm{Im}(\varepsilon)$ (See immersion simulations in [Sab+14] for an example where the handedness of the structure does not cause CD signal when $\mathrm{Re}(\varepsilon)$ is the same for both channels).

A structure-photonic "bottom-up" view of chirality?

Studying systems of both "nematic" and a orientationally random helix gases (sec. 5.3.2) showed hardly optical chirality—in spite of consisting from "maximally chiral elements" (helices). This shows up two major implications on perfect dielectrics as carriers of chirality:

- The notion of "chiral building blocks" does not (or only to little extent, in case of helix axes aligned with inclination) translate on superstructures, *i. e.* locally handed dielectrics cannot straightforwardly explain global chirality. This puts great demand on geometric yet optics-compatible chirality measures.

  Moreover, these observations underline the conceptual difference of the chiral response of "photonic length-scale" media compared to those with intrinsic chirality (*e. g.* sugar solutions), the latter being badly described by an all-dielectric geometry model.

- "CD Helicity" (*i. e.*, visibility of handedness by light) gets greatly augmented by *periodicity*. Although a genuine property of the dielectric building blocks themselves, the (discrete and uniform) organisation of a structure-photonic medium plays as well an essential role in the emergence of optical chirality—though conceptually incompatible lateral continuity of plane waves! To dissect that process, tunable distortion is the appropriate "probe", as it allows continuous intermediate steps in between.

CCR: A measure for chiro-optical response of structure-photonic media

The cumulative circular contrast CCR (and CCT, when, in the case of lossy media, they do not coincide) proves as a versatile measure to quickly and robustly judge a given scattering geometry for its chiral properties: by answering both "How much CD?" (effective dichroic bandwidth) and "At which colour?" (preserved frequency dependence/spectrum character). Implications, limitations and interpretation have been discussed in sections 3.1.2 and 5.4.

However, besides discussing a link to complementary (*e. g.*, experimental) techniques, surveying reflectances and/or transmissions will at least have to include a way to visualise the absolute reflectance besides.

5.7. Outlook

5.7.1. Further approaches and variations of the PhC system

- Linear chirp: prove sinusoidal observations with a non-periodic "true" chirp by either spatially constant gradient pitch, or discrete, *i. e.* Assemble chirp by stacking uniformly distorted crystals with constant distortion in normal direction (of which we can calculate the band structure separately)
- Other types of deterministic low-wavevector distortions throughout the structure
- Helical model(s): ⟨111⟩[78], or ⟨100⟩ with complementary smaller/bigger helices
- Polarisation analysis: This thesis does not study the ellipticity of reflected/transmitted light. Study partial CCRs ("elliptic contrasts", including discrimination between handedness-conserving and handedness-inverting fractions).
- CD is, in its traditional definition, caused by CP-sensitive *attenuation*. Study partial CCR and CCT elliptic contrasts
- Polycrystalline/"Amorphous" types of disorder (grain boundaries, topological defects)—require a lot more computational power
- Helix array azimuthal (phase) noise
- **4srs** with higher ε, and testing robustness against incident angle, distortion
- Investigate the feasibility of an "Amorphous Gyroid" (inspired by "amorphous Diamond" [Bur+14], or disordered self-assembly of Laves phases): the behaviour of its geometric/optical chirality while disturbing its global topology (while preserving the local order).

5.7.2. Circular polarisation, the photon's chirality, and Lipkin's Zilch

Lipkin [Lip64] discovered and described the quantity

$$Z^{00} = \mathbf{E} \cdot (\nabla \times \mathbf{E}) + \mathbf{H} \cdot (\nabla \times \mathbf{H}) \tag{5.2}$$

In free space, it • is a conserved quantity of the EM field/Maxwell equations • is related to the photon spin, *i. e.* its circular polarisation, and thus • could serve as a "natural" measure of the light's CP (at least in free space, possibly generalisable towards $\varepsilon \neq 1$ media).

Bliokh and Nori [BN11] underlined a remarkable symmetry between Energy density–Poynting vector ↔ "Chiral Density"–"Chirality Flow" (analogue to the Zilch). The introduction of a "natural" measure of the chirality of electromagnetic waves, being generalisable over plane-wave, may help to more comprehensively describe the "degree of chirality" of field patterns in the interior of non-uniform media, and eventually help identify the "chiro-optically active geometry features" of dielectric structures (perhaps, resembling the way the **H** field patterns unveil the active geometric features of the plasmonic Gyroid within [Oh+12]).

---

[78] These are the rods forming the Gyroid solid phase in [ER14].

Appendix

Cornelis Gijsbrechts: "Quodlibet" (1675)

A. Gallery of real-space structures

Note that, due to an HDF5 import bug within the used data visualisation program VisIt (`https://visit.llnl.gov/`), the x and z coordinates get swapped on export. Thus, within the structure depictions, the *handedness is inverted* with respect to the absolute spatial configuration.

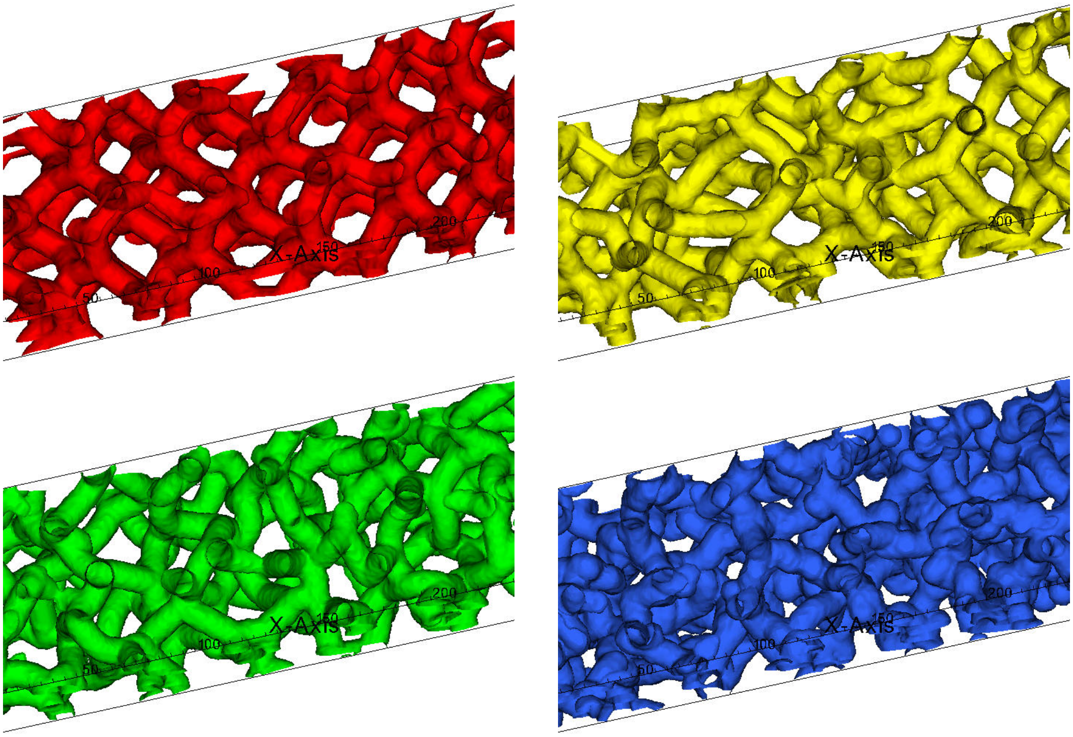

Figure A.1.: Different network Gyroid initialisations (for fig. 5.3), all with the same $\sigma_r/a = 0.2$, but differing in correlation length scale: $\sigma_q a/(2\pi) = 0.3$ (red, upper left), $\sigma_q a/(2\pi) = 0.7$ (yellow, upper right), $\sigma_q a/(2\pi) = 1.0$ (green, lower left), and $\sigma_q a/(2\pi) = 2.3$ (blue, lower right).

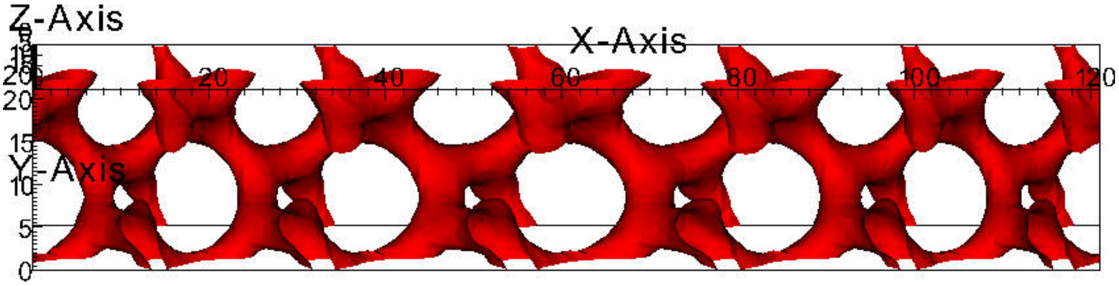

Figure A.2.: Nodal Gyroid subject to loosening chirp: the structure is compressed in the vicinity of the surfaces and stretched in the middle of the simulation box (chirp phase $0.25 \times 2\pi$). Chirp amplitude $\sigma_r / a = 0.2$.

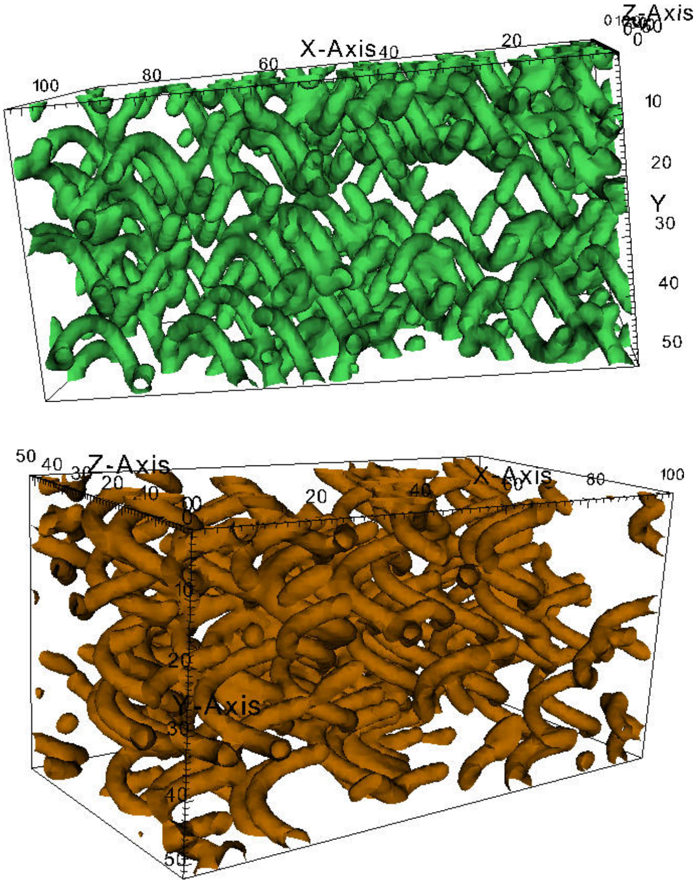

Figure A.3.: Simulation box: “Nematic gas” consisting of effectively uncorrelated helices oriented in normal direction (green, upper image) or perpendicular to normal/“inclination” direction (brown, lower image).

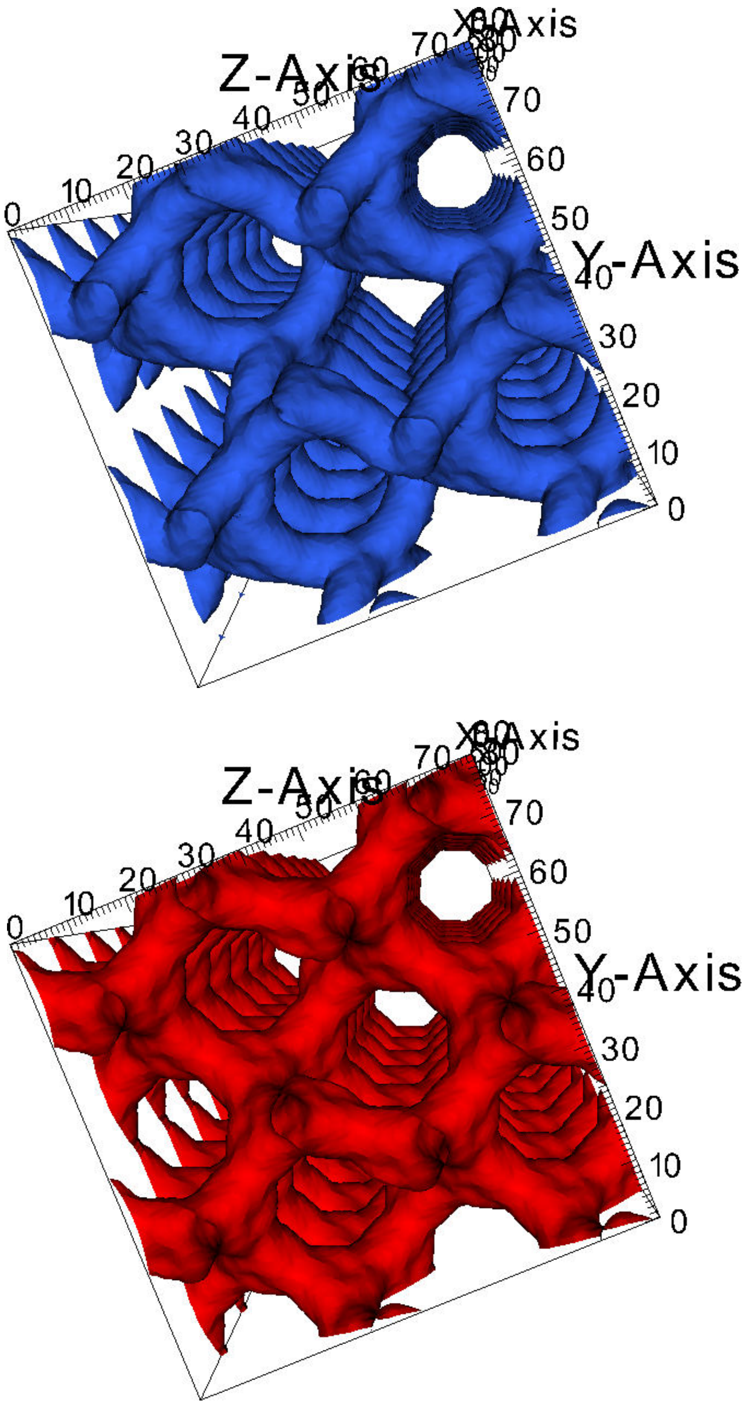

Figure A.4.: Top view of the simulation box of the SC- (upper image, blue, three helices per unitcube) and BCC-helical Gyroid (lower image, red, six helices per unitcube).

B. Auxiliary calculations

B.1. Self-correlation of Fourier-decomposed vector field

This computation has been carried out in section 4.3.3 to deliver an exact expression for the autocorrelation of an arbitrary field $\mathbf{u}(\mathbf{r})$, solely expressed in terms of real-valued amplitudes and scalar phases. It determines normalisation, and is an intermediate step for further interpretation, once a realistic model for $\mathbf{u}$ is inserted.

$$
\begin{aligned}
G(\mathbf{x}) =& (\mathbf{u} * \mathbf{u})(\mathbf{x}) = \\
&= \int_{\mathrm{SC}} \frac{\mathrm{d}^3 r}{V_{\mathrm{SC}}} \mathbf{u}(\mathbf{r}) \cdot \mathbf{u}(\mathbf{r}+\mathbf{x}) = \\
&= 2\Upsilon \sum_{\mathbf{q},\mathbf{q}'} \mathbf{u}_{\mathbf{q}} \mathbf{u}_{\mathbf{q}'} \int_{\mathrm{SC}} \frac{\mathrm{d}^3 r}{V_{\mathrm{SC}}} \cos(\mathbf{q}\cdot\mathbf{r} + \varphi_{\mathbf{q}}) \cos(\mathbf{q}'\cdot(\mathbf{r}+\mathbf{x}) + \varphi_{\mathbf{q}'}) = \\
&= 2\Upsilon \sum_{\mathbf{q},\mathbf{q}'} \mathbf{u}_{\mathbf{q}} \cdot \mathbf{u}_{\mathbf{q}'} \int_{\mathrm{SC}} \frac{\mathrm{d}^3 r}{V_{\mathrm{SC}}} \times \\
&\quad \times \big(\cos(\mathbf{q}\cdot\mathbf{r}) \cos(\varphi_{\mathbf{q}}) - \sin(\mathbf{q}\cdot\mathbf{r}) \sin(\varphi_{\mathbf{q}})\big) \times \\
&\quad \times \big(\cos(\mathbf{q}'\cdot\mathbf{r}) \cos(\mathbf{q}'\cdot\mathbf{x} + \varphi_{\mathbf{q}'}) - \sin(\mathbf{q}'\cdot\mathbf{r}) \sin(\mathbf{q}'\cdot\mathbf{x} + \varphi_{\mathbf{q}'})\big) \\
&= 2\Upsilon \sum_{\mathbf{q},\mathbf{q}'} \mathbf{u}_{\mathbf{q}} \cdot \mathbf{u}_{\mathbf{q}'} \int_{\mathrm{SC}} \frac{\mathrm{d}^3 r}{V_{\mathrm{SC}}} \big(\, 0+ \\
&\quad + \cos(\mathbf{q}\cdot\mathbf{r}) \cos(\varphi_{\mathbf{q}}) \cdot \cos(\mathbf{q}'\cdot\mathbf{r}) \cos(\mathbf{q}'\cdot\mathbf{x} + \varphi_{\mathbf{q}'}) + \\
&\quad + \sin(\mathbf{q}\cdot\mathbf{r}) \sin(\varphi_{\mathbf{q}}) \cdot \sin(\mathbf{q}'\cdot\mathbf{r}) \sin(\mathbf{q}'\cdot\mathbf{x} + \varphi_{\mathbf{q}'}) + \\
&\quad - \cos(\mathbf{q}\cdot\mathbf{r}) \cos(\varphi_{\mathbf{q}}) \cdot \sin(\mathbf{q}'\cdot\mathbf{r}) \sin(\mathbf{q}'\cdot\mathbf{x} + \varphi_{\mathbf{q}'}) + \\
&\quad - \sin(\mathbf{q}\cdot\mathbf{r}) \sin(\varphi_{\mathbf{q}}) \cdot \cos(\mathbf{q}'\cdot\mathbf{r}) \cos(\mathbf{q}'\cdot\mathbf{x} + \varphi_{\mathbf{q}'}) \,\big) = \\
&= \Upsilon \sum_{\mathbf{q},\mathbf{q}'} \mathbf{u}_{\mathbf{q}} \cdot \mathbf{u}_{\mathbf{q}'} \int_{\mathrm{SC}} \frac{\mathrm{d}^3 r}{V_{\mathrm{SC}}} \big(\, 0+ \\
&\quad + \cos(\varphi_{\mathbf{q}}) \cos(\mathbf{q}'\cdot\mathbf{x} + \varphi_{\mathbf{q}'}) \cdot \big(\cos\big((\mathbf{q}-\mathbf{q}')\cdot\mathbf{r}\big) + \cos\big((\mathbf{q}+\mathbf{q}')\cdot\mathbf{r}\big)\big) + \\
&\quad + \sin(\varphi_{\mathbf{q}}) \sin(\mathbf{q}'\cdot\mathbf{x} + \varphi_{\mathbf{q}'}) \cdot \big(\cos\big((\mathbf{q}-\mathbf{q}')\cdot\mathbf{r}\big) - \cos\big((\mathbf{q}+\mathbf{q}')\cdot\mathbf{r}\big)\big) + \\
&\quad - \cos(\varphi_{\mathbf{q}}) \sin(\mathbf{q}'\cdot\mathbf{x} + \varphi_{\mathbf{q}'}) \cdot \big(\sin\big(-(\mathbf{q}-\mathbf{q}')\cdot\mathbf{r}\big) + \sin\big((\mathbf{q}+\mathbf{q}')\cdot\mathbf{r}\big)\big) + \\
&\quad - \sin(\varphi_{\mathbf{q}}) \cos(\mathbf{q}'\cdot\mathbf{x} + \varphi_{\mathbf{q}'}) \cdot \big(\sin\big((\mathbf{q}-\mathbf{q}')\cdot\mathbf{r}\big) + \sin\big((\mathbf{q}+\mathbf{q}')\cdot\mathbf{r}\big)\big) \,\big) =
\end{aligned}
$$

$$
\begin{aligned}
&= \Upsilon \sum_{\mathbf{q},\mathbf{q}'} \mathbf{u}_{\mathbf{q}} \cdot \mathbf{u}_{\mathbf{q}'} \big(0 + \\
&\quad + \cos(\varphi_{\mathbf{q}}) \cos(\mathbf{q}' \cdot \mathbf{x} + \varphi_{\mathbf{q}'}) \cdot \left(\delta_{\mathbf{q}}^{\mathbf{q}'} + \delta_{-\mathbf{q}}^{\mathbf{q}'} \right) + \\
&\quad + \sin(\varphi_{\mathbf{q}}) \sin(\mathbf{q}' \cdot \mathbf{x} + \varphi_{\mathbf{q}'}) \cdot \left(\delta_{\mathbf{q}}^{\mathbf{q}'} - \delta_{-\mathbf{q}}^{\mathbf{q}'} \right) + \\
&\quad - \cos(\varphi_{\mathbf{q}}) \sin(\mathbf{q}' \cdot \mathbf{x} + \varphi_{\mathbf{q}'}) \cdot 0 \\
&\quad - \sin(\varphi_{\mathbf{q}}) \cos(\mathbf{q}' \cdot \mathbf{x} + \varphi_{\mathbf{q}'}) \cdot 0 \big) = \\
&= \Upsilon \sum_{\mathbf{q}} \big(\mathbf{u}_{\mathbf{q}}^2 \cdot \big(\cos(\varphi_{\mathbf{q}}) \cos(\mathbf{q} \cdot \mathbf{x} + \varphi_{\mathbf{q}}) + \sin(\varphi_{\mathbf{q}}) \sin(\mathbf{q} \cdot \mathbf{x} + \varphi_{\mathbf{q}}) \big) + \\
&\quad + \mathbf{u}_{\mathbf{q}} \cdot \mathbf{u}_{-\mathbf{q}} \cdot \big(\cos(\varphi_{\mathbf{q}}) \cos(\mathbf{q} \cdot \mathbf{x} - \varphi_{\mathbf{q}}) + \sin(\varphi_{\mathbf{q}}) \sin(\mathbf{q} \cdot \mathbf{x} - \varphi_{-\mathbf{q}}) \big) \big) = \\
&= \Upsilon \sum_{\mathbf{q}} \Bigg(\cos(\mathbf{q} \cdot \mathbf{x}) \cdot \Big(\mathbf{u}_{\mathbf{q}}^2 \big(\cos^2(\varphi_{\mathbf{q}}) + \sin^2(\varphi_{\mathbf{q}}) \big) + \mathbf{u}_{\mathbf{q}} \cdot \mathbf{u}_{-\mathbf{q}} \big(\cos^2(\varphi_{\mathbf{q}}) - \sin^2(\varphi_{-\mathbf{q}}) \big) \Big) + \\
&\quad + \sin(\mathbf{q} \cdot \mathbf{x}) \cdot \Big(\mathbf{u}_{\mathbf{q}}^2 \cdot \sin(\varphi_{\mathbf{q}}) \cos(\varphi_{\mathbf{q}}) \cdot (1-1) + \mathbf{u}_{\mathbf{q}} \cdot \mathbf{u}_{-\mathbf{q}} \big(\sin(\varphi_{\mathbf{q}}) \cos(\varphi_{\mathbf{q}}) + \sin(\varphi_{\mathbf{q}}) \cos(\varphi_{-\mathbf{q}}) \big) \Big) \Bigg) = \\
&= \Upsilon \sum_{\mathbf{q}} \mathbf{u}_{\mathbf{q}} \cdot \Bigg(\cos(\mathbf{q} \cdot \mathbf{x}) \big(\mathbf{u}_{\mathbf{q}} + \mathbf{u}_{-\mathbf{q}} \big(\cos^2(\varphi_{\mathbf{q}}) - \sin^2(\varphi_{-\mathbf{q}}) \big) \big) + \\
&\quad + \sin(\mathbf{q} \cdot \mathbf{x}) \cdot \mathbf{u}_{-\mathbf{q}} \big(\sin(\varphi_{\mathbf{q}}) \cos(\varphi_{\mathbf{q}}) + \sin(\varphi_{\mathbf{q}}) \cos(\varphi_{-\mathbf{q}}) \big) \Bigg)
\end{aligned}
$$

This all shrinks to a one-liner if carried out in complex notation. Therefore, it is largely to be understood as trigonometric callisthenics, and a “pedestrian” test if the four (instead of six) parameters $\{\mathbf{u}_{\mathbf{q}}, \varphi_{\mathbf{q}}\}$ suffice to fully describe the Fourier coefficients.

B.2. Self-correlation of a finite volume

Assume you want to calculate the radial averaged pair distribution function (RDF)

$$
g(r) = \mathcal{N} \sum_{j=1}^{N} \sum_{i=1}^{N} \delta(r - |\mathbf{r}_i - \mathbf{r}_j|) \tag{B.1}
$$

from a set of N points i in the Euclidean space $\mathbb{R}^d$, each lying at $\mathbf{r}_i$ within a convex volume V. The “box dimensions” impose a length scale L of the order $\sqrt[d]{V}$, d being the number of coordinates per point (the spatial dimension).

A sensible requirement for the normalisation $\mathcal{N}$ is to have the equal probability value to unity at any radius. Let us have a closer look to the pair detection statistics: Obviously, the contributions for the smallest occurring r ($r \ll V$ for large N) come from “neighbours” predominantly deep within the volume, and thus increase their contribution with enlarging radius r by the $(d-1)$th power of r (the surface area of the sphere with radius r, which is for almost every point fully contained within V). So, $\mathcal{N}$ is essentially proportional to $r^{1/(d-1)}$ for small r.

In contrast, the (small) solid angle in which the “last possible” distances $r \gtrsim L$ still fully contained in V are seen, demands a near-constant normalisation scaling. In between, a function dependent on the exact shape of V is expected.

Rather than to reject any length information from your RDF longer than, say, the shortest diameter of V, to “hopefully” avoid “most of” the finite-volume effects (deviations from $r^{1/(d-1)}$ behaviour), you can actively compensate them: The RDF, as shown in eq. (B.1), is essentially the convolution of the point density $\varrho(\mathbf{r}) = \sum_{i=1}^{N} \delta(\mathbf{r} - \mathbf{r}_i)$ with itself (followed by integrating out the angle dependency). In words of reintroducing the integrals:

$$g(r) = \mathcal{N} \int\limits_{\mathbb{R}^{2d}} \mathrm{d}^d x \, \mathrm{d}^d y \cdot \sum_{j=1}^{N} \delta(\mathbf{r}_j - \mathbf{x}) \cdot \sum_{i=1}^{N} \delta(\mathbf{r}_i - \mathbf{y}) \cdot \delta(r - |\mathbf{y} - \mathbf{x}|) \tag{B.2}$$

The outside of the volume V is distinct from its inside in that it must not contain any point. So, for any given vector $\mathbf{y} - \mathbf{x}$ to test for a point, we can decide *a priori* if it may contain a point at all: by testing $\mathbf{x}, \mathbf{y} \overset{?}{\in} V$. If the vector pair is invalid, reject it, and "count" how many acceptances and rejections have occurred per possible distance $r = |\mathbf{y} - \mathbf{x}|$.

This is (trivially) equivalent to the natural restriction of the integration volume to V alone, and leads to a normalisation condition in the following way: It should hold for arbitrary points sets, including ones with a homogeneous[79] density throughout V. In this case, the point density must be replaceable by just unity, or, more precisely the characteristic function

$$\varrho(\mathbf{r}) \propto \chi_V(\mathbf{r}) = \begin{cases} 1 & \mathbf{r} \in V \\ 0 & \text{outside} \end{cases} , \tag{B.3}$$

giving with eq. (B.2) and the intention to get unity correlation for homogeneous densities (within V):

$$\begin{aligned} g(r) =& \mathcal{N} \int\limits_V \mathrm{d}^d x \int\limits_V \mathrm{d}^d y \cdot \delta(r - |\mathbf{y} - \mathbf{x}|) \overset{!}{=} 1 \\ r \mapsto \mathcal{N}^{-1} =& \int\limits_V \mathrm{d}^d x \int\limits_V \mathrm{d}^d y \cdot \delta(r - |\mathbf{y} - \mathbf{x}|) = \int\limits_{\mathbb{R}^d} \mathrm{d}^d x \int\limits_{\mathbb{R}^d} \mathrm{d}^d y \cdot \chi_V(\mathbf{x}) \cdot \chi_V(\mathbf{y}) \cdot \delta(r - |\mathbf{y} - \mathbf{x}|) = \\ =& \int\limits_{\mathbb{R}^d} \mathrm{d}^d a \int\limits_{\mathbb{R}^d} \mathrm{d}^d b \cdot \chi_V\left(\frac{\mathbf{a} - \mathbf{b}}{2}\right) \cdot \chi_V\left(\frac{\mathbf{a} + \mathbf{b}}{2}\right) \cdot \delta(r - |\mathbf{a}|) = \\ =& \int\limits_{\mathbb{R}^d} \mathrm{d}^{d-1}\Omega \int\limits_{\mathbb{R}^d} \mathrm{d}^d b \cdot \chi_V\left(\frac{r\mathbf{e}_\Omega - \mathbf{b}}{2}\right) \cdot \chi_V\left(\frac{r\mathbf{e}_\Omega + \mathbf{b}}{2}\right) \end{aligned} \tag{B.4}$$

This represents the self-correlation of the volume V, averaged over the solid angle Ω, or, in other words, how probable it is for a distance starting withing V, having the length r and random orientation, to end within the volume.

The box

We want to compute the normalisation function of the suggesting shape of a finite volume in Euclidean space: the (hyper)rectangle, or simply "box", defined by intervals on the coordinate axes (In the following, I will stick to the $d = 3$ three-dimensional case). The box may be defined as

$$\chi_{\text{box}}(\mathbf{r}) = \begin{cases} 1 & -L_j < j < L_j \quad \forall j = x, y, z \\ 0 & \text{else} \end{cases} , \tag{B.5}$$

the product of three independent 1-D box functions $\Theta(j + L_j)\Theta(L_j - j)$ along the coordinate axes. By applying the self-convolution of this box function, one comes to the triangle function $|L_j - j| \cdot \Theta(j +$

---

[79] Homogeneous in the sense that no radial structure is perceptible at the smallest distances r subject to investigation.

$L_j)\Theta(L_j - j)$, By expressing the remaining space integration in spherical coordinates, one gets[80]

$$\begin{aligned}\mathcal{N}^{-1} =& 8\int_0^{\pi/2} \mathrm{d}\vartheta \int_0^{\pi/2} \mathrm{d}\varphi \sin(\vartheta)\cdot(L_x - r\cdot\cos(\varphi)\cdot\sin(\vartheta))\cdot(L_y - r\cdot\sin(\varphi)\cdot\sin(\vartheta))\cdot(L_z - r\cdot\cos(\vartheta)) = \\ =& L_x\cdot L_y\cdot L_z - \frac{1}{2}r(L_x\cdot L_y + L_x\cdot L_z + L_y\cdot L_z) + \frac{2}{3\pi}r^2\cdot(L_x+L_y+L_z) - \frac{3}{4\pi}r^3 \quad .\end{aligned} \tag{B.6}$$

As long as the viewed distance does not exceed any L_j, this formula exactly normalises RDF data to unity in the continuous-density limit.

B.3. Convert light frequency to colour

Frequency reference colour bar

In order to draw fancy bars of equivalent light colour aside frequency-resolved data in the optical frequency range, you have to know at first how the respective frequencies stimulate your colour vision receptors, and second, how this data translates to the colour system of your display device.

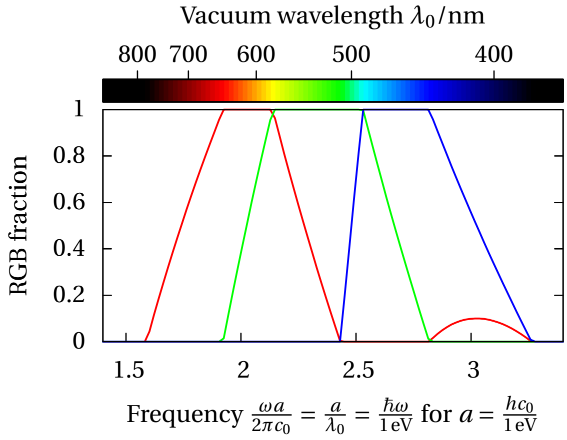

Figure B.1.: Frequency-to-RGB conversion

Here (although this work is intended for print), we will stick to the additive (RGB) colour composition of monitors, due to their natural relation to light (self-illuminating), ease of concept and reproducibility (printing colours (subtractive synthesis via pigment mixing) are subject to much greater deviations than light mixing).

Once an explicit scale for a is introduced (as described in sec. 2.1.6), an interconversion of reduced frequency to RGB values can be applied. The scheme presented here is adapted from [Bru96].[81] Every colour channel is referred to with a trapezium function, linearly interpolating between the corner colours; an additional red hump in the region adjacent to (invisible) UV mimics the eye's red sensitivity for the distinction of deep blue and violet.

---

[80] By exploiting symmetry of the three $x_j = 0$ mirror planes, it suffices to compute within the first octant $x_j \geq 0$ and to multiply the result with 8.

[81] As this data is given in terms of vacuum wavelengths λ_0, this representation is also parametrised that way, and conversion to frequencies via $\omega = 2\pi c_0/\lambda_0$ is done at the output.

C. Computing power and tea statistics

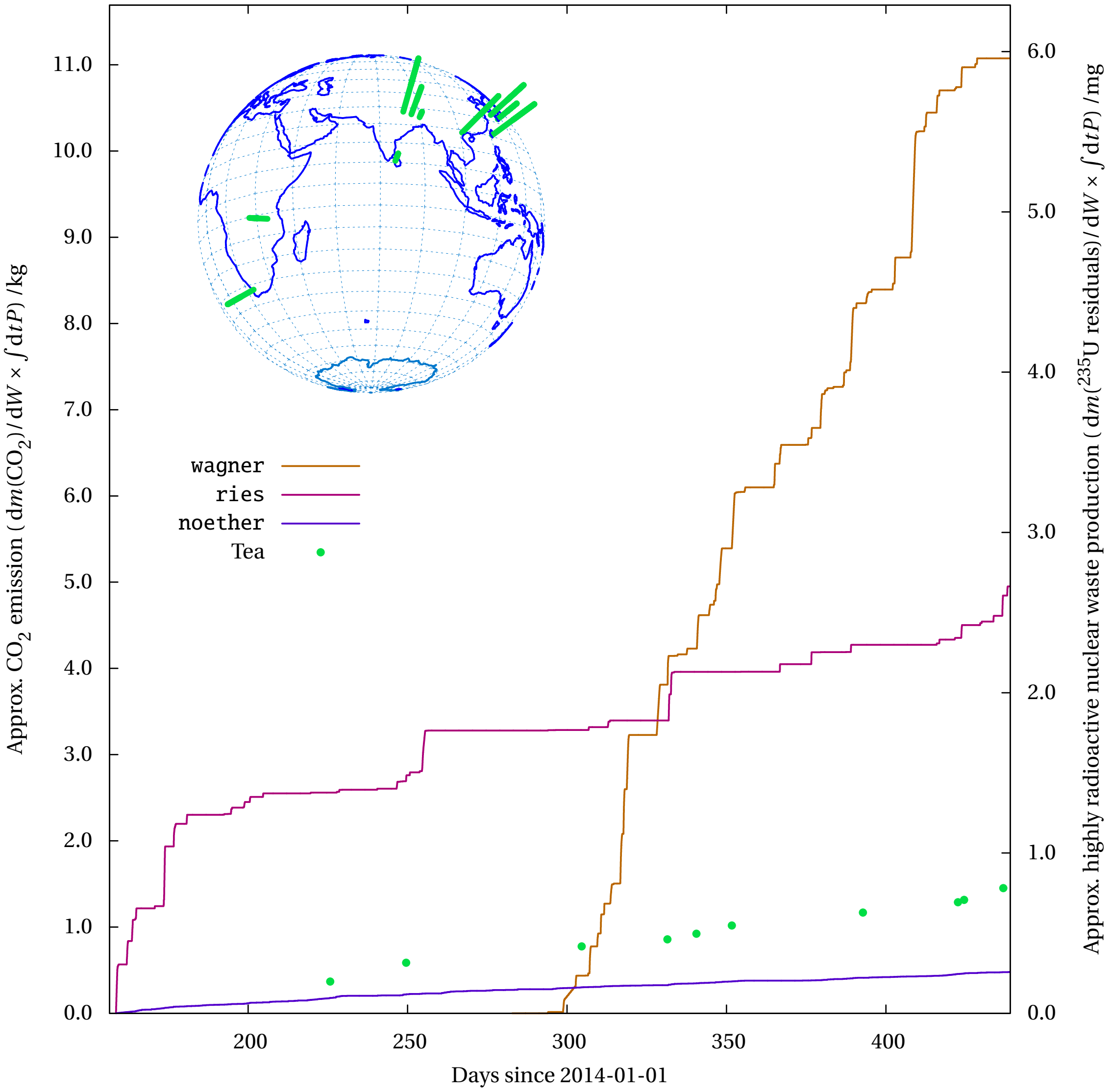

Figure C.1.: Estimated environmental impact from the electrical energy consumed by computing power (separated by host names) and tea preparation (inset: origins of tea; bar heights scaling factor: 159 km L^{-1}; Yerba Maté neglected) throughout writing this thesis, at the location in Erlangen. Assessment base: `http://www.estw.de/stromkennzeichnung` for the Erlangen electric fuel mix disclosure (CO_2 emissions and fraction of nuclear energy), and BDEW Leitfaden „Stromkennzeichnung“ (nuclear waste accumulation rate 7.5 µg J^{-1} of delivered electrical power).

Bibliography

[14] *Reticular Chemistry Structure Resource*. Department of Applied Mathematics, Australian National University et al. June 2014. URL: `http://rcsr.anu.edu.au/rcsr_nets/search`.

[Abd08] I. Abdulhalim. “Effect of the number of sublayers on axial optics of anisotropic helical structures”. In: *Appl. Opt.* 47.16 (2008), pp. 3002–3008. DOI: `10.1364/ao.47.003002`.

[Air33] George B. Airy. “On the phenomena of Newton’s rings when formed between two transparent Substances of different refractive Powers”. In: *Phil. Mag.* 2 (1833), pp. 20–30.

[AM76] Neil W. Ashcroft and N. David Mermin. *Solid State Physics*. Thomson Learning, 1976. ISBN: 0030839939.

[Ama09] David B. Amabilino, ed. *Chirality at the nanoscale*. 2009. ISBN: 978-3-527-32013-4.

[Arn97] L.R. Arnaut. “Chirality in Multi-Dimensional Space With Application To Electromagnetic Characterisation of Multi-Dimensional Chiral and Semi-Chiral Media”. In: *J. Electromagn. Waves Appl.* 11.11 (Jan. 1997), pp. 1459–1482. DOI: `10.1163/156939397x00549`.

[Bér94] Jean-Pierre Bérenger. “A perfectly matched layer for the absorption of electromagnetic waves”. In: *J. Comput. Phys.* 114.2 (Oct. 1994), pp. 185–200. DOI: `10.1006/jcph.1994.1159`.

[Blo29] Felix Bloch. “Über die Quantenmechanik der Elektronen in Kristallgittern”. In: *Z. Phys.* 52.7-8 (July 1929), pp. 555–600. DOI: `10.1007/bf01339455`.

[BN11] Konstantin Y. Bliokh and Franco Nori. “Characterizing optical chirality”. In: *Phys. Rev. A* 83.2 (Feb. 2011). DOI: `10.1103/physreva.83.021803`.

[Bra92] Kenneth A. Brakke. “The Surface Evolver”. In: *Experimental Mathematics* 1.2 (Jan. 1992), pp. 141–165. DOI: `10.1080/10586458.1992.10504253`. URL: `http://www.eecs.berkeley.edu/~sequin/CS284/TEXT/brakke.pdf`.

[BRJ99] Gerald Busse, Jens Reinert, and Arne F. Jacob. “Waveguide characterization of chiral material: experiments”. In: *IEEE Trans. Microwave Theory Techn.* 47.3 (Mar. 1999), pp. 297–301. DOI: `10.1109/22.750230`.

[Bru96] Dan Bruton. *Approximate RGB values for Visible Wavelengths*. 1996. URL: `http://www.physics.sfasu.edu/astro/color/spectra.html`.

[Bur+14] Matteo Burresi et al. “Bright-White Beetle Scales Optimise Multiple Scattering of Light”. In: *Scientific Reports* 4 (Aug. 2014), p. 6075. DOI: `10.1038/srep06075`.

[CFL28] Richard Courant, Kurt Friedrichs, and Hans Lewy. “Über die partiellen Differenzengleichungen der mathematischen Physik”. In: *Mathematische Annalen* 100.1 (Dec. 1928), pp. 32–74. DOI: `10.1007/bf01448839`. URL: `http://resolver.sub.uni-goettingen.de/purl?GDZPPN002272636`.

[CN98] Alongkarn Chutinan and Susumu Noda. "Spiral three-dimensional photonic-band-gap structure". In: *Phys. Rev. B* 57.4 (Jan. 1998), R2006–R2008. DOI: `10.1103/physrevb.57.r2006`.

[Cox55] H. S. M. Coxeter. "On Laves' graph of girth ten". In: *Canad. J. Math.* 7 (Jan. 1955), pp. 18–23. DOI: `10.4153/cjm-1955-003-7`.

[Dec14] Benedikt Decker. "Biophotonic Diamond Membranes: Effect of anisotropic dielectric constants". Bachelor's Thesis. FAU Erlangen, 2014.

[Dem+12] Angela Demetriadou, Sang Soon Oh, Sebastian Wuestner, and Ortwin Hess. "A tri-helical model for nanoplasmonic gyroid metamaterials". In: *New Journal of Physics* 14.8 (Aug. 2012), p. 083032. DOI: `10.1088/1367-2630/14/8/083032`.

[Dol+14] James A. Dolan et al. "Optical Properties of Gyroid Structured Materials: From Photonic Crystals to Metamaterials". In: *Adv. Opt. Mater.* 3.1 (Nov. 2014), pp. 12–32. DOI: `10.1002/adom.201400333`.

[Dom13] Filip Dominec. *MEEP – my notes on FDTD simulation*. 2013. URL: `http://www.fzu.cz/~dominecf/meep/index.html`.

[DV11] Alexei Deinega and Ilya Valuev. "Long-time behavior of PML absorbing boundaries for layered periodic structures". In: *Comput. Phys. Commun.* 182.1 (Jan. 2011), pp. 149–151. DOI: `10.1016/j.cpc.2010.06.006`. URL: `http://fdtd.kintechlab.com/_media/deinega_-_long-time_behavior_of_pml_absorbing_boundaries_for_layered_periodic_structures.pdf`.

[EJ88] Nader Engheta and Dwight Jaggard. "Electromagnetic chirality and its applications". In: *IEEE Antennas Propagat. Soc. Newsletter* 30.5 (1988), pp. 6–12. DOI: `10.1109/map.1988.6086107`.

[ER14] Myfanwy E. Evans and Roland Roth. "Shaping the Skin: The Interplay of Mesoscale Geometry and Corneocyte Swelling". In: *Phys. Rev. Lett.* 112.3 (Jan. 2014). DOI: `10.1103/physrevlett.112.038102`.

[Ere+04] Mikhail I. Eremets et al. "Single-bonded cubic form of nitrogen". In: *Nat. Mater.* 3.8 (July 2004), pp. 558–563. DOI: `10.1038/nmat1146`.

[Far+06] Ardavan Farjadpour et al. "Improving accuracy by subpixel smoothing in FDTD". In: *Opt. Lett.* 31 (Oct. 2006), pp. 2972–2974. DOI: `10.1364/OL.31.002972`.

[Flo83] Gaston Floquet. "Sur les équations différentielles linéaires à coefficients périodiques". In: *Ann. Ecole Norm. Supér.* 12 (1883), pp. 47–88. URL: `http://www.numdam.org/item?id=ASENS_1883_2_12__47_0`.

[Fre+10] Georg von Freymann et al. "Three-Dimensional Nanostructures for Photonics". In: *Adv. Funct. Mater.* 20.7 (Mar. 2010), pp. 1038–1052. DOI: `10.1002/adfm.200901838`. URL: `http://wwwrsphysse.anu.edu.au/nonlinear/papers/pdf/ADFM_2010_20_1038.pdf`.

[Gal09] Mark Galassi. *GNU Scientific Library Reference Manual*. 3rd ed. Network Theory, 2009. ISBN: 978-0-9546120-7-8. URL: `http://www.gnu.org/software/gsl/`.

[Gan+09] J. K. Gansel et al. "Gold Helix Photonic Metamaterial as Broadband Circular Polarizer". In: *Science* 325.5947 (Aug. 2009), pp. 1513–1515. DOI: `10.1126/science.1177031`.

[GR76] H. Ghiradella and W. Radigan. “Development of butterfly scales. II. Struts, lattices and surface tension”. In: *J. Morphol.* 150.2 (Oct. 1976), pp. 279–297. ISSN: 1097-4687. DOI: `10.1002/jmor.1051500202`.

[HL33] Heinrich Heesch and Fritz Laves. “Über dünne Kugelpackungen”. In: *Z. Krist.* 85.1 (Jan. 1933). DOI: `10.1524/zkri.1933.85.1.443`.

[Hol+92] R. D. Hollinger, V. V. Varadan, D. K. Ghodgaonkar, and V. K. Varadan. “Experimental characterization of isotropic chiral composites in circular waveguides”. In: *Radio Sci.* 27.2 (Mar. 1992), pp. 161–168. DOI: `10.1029/91rs02458`.

[HOP08] Stephen T. Hyde, Michael O’Keeffe, and Davide M. Proserpio. “A Short History of an Elusive Yet Ubiquitous Structure in Chemistry, Materials, and Mathematics”. In: *Angew. Chem., Int. Ed.* 47.42 (Oct. 2008), pp. 7996–8000. DOI: `10.1002/anie.200801519`. URL: `http://people.physics.anu.edu.au/~sth110/Angew_Chem_Int_Ed_srs.pdf`.

[Int04] International Union of Crystallography. *International Tables for Crystallography*. Ed. by Hans Wondratschek and Ulrich Müller. Vol. A1: Symmetry Relations between Space Groups. Kluwer Academic Publishers, 2004. ISBN: 1402023553.

[Jac98] John D. Jackson. *Classical Electrodynamics*. Third Edition. Wiley, 1998. ISBN: 047130932X.

[JJ01] Steven Johnson and John Joannopoulos. “Block-iterative frequency-domain methods for Maxwell’s equations in a planewave basis”. In: *Opt. Express* 8.3 (2001), p. 173. ISSN: 1094-4087. DOI: `10.1364/oe.8.000173`.

[JMP79] D. L. Jaggard, A. R. Mickelson, and C. H. Papas. “On electromagnetic waves in chiral media”. In: *Appl. Phys.* 18.2 (Feb. 1979), pp. 211–216. DOI: `10.1007/bf00934418`.

[JMW95] John D. Joannopoulos, Robert D. Meade, and Joshua N. and Winn. *Photonic crystals*. Princeton University Press, 1995. ISBN: 978-0691037448.

[Joa+08] John D. Joannopoulos, Steven G. Johnson, Joshua N. Winn, and Robert D. Meade. *Photonic Crystals: Molding the Flow of Light*. Second edition. Princeton University Press, 2008. ISBN: 978-0-691-12456-8. URL: `http://ab-initio.mit.edu/book/`.

[Joh10] Steven G. Johnson. *Notes on Perfectly Matched Layers (PMLs)*. Mar. 2010. URL: `http://math.mit.edu/~stevenj/18.369/pml.pdf`.

[Joh87] Sajeev John. “Strong localization of photons in certain disordered dielectric superlattices”. In: *Physical Review Letters* 58.23 (June 1987), pp. 2486–2489. DOI: `10.1103/physrevlett.58.2486`. URL: `http://dx.doi.org/10.1103/PhysRevLett.58.2486`.

[Jon89] Douglas S. Jones. *Acoustic and Electromagnetic Waves*. Clarendon, 1989. ISBN: 0-19-853380-2.

[Lav32] Fritz Laves. “Zur Klassifikation der Silikate. Geometrische Untersuchungen möglicher Silicium-Sauerstoff- Verbände als Verknüpfungsmöglichkeiten regulärer Tetraeder”. In: *Z. Krist.* 82.1 (Jan. 1932), pp. 1–14. DOI: `10.1524/zkri.1932.82.1.1`.

[LC05] Jeffrey Chi Wai Lee and C. T. Chan. “Polarization gaps in spiral photonic crystals”. In: *Opt. Express* 13.20 (2005), pp. 8083–8088. DOI: `10.1364/OPEX.13.008083`.

[Lip64] Daniel M. Lipkin. “Existence of a New Conservation Law in Electromagnetic Theory”. In: *J. Math. Phys.* 5.5 (1964), p. 696. DOI: `10.1063/1.1704165`.

[LRT96] Charla A. Lambert, Leonard H. Radzilowski, and Edwin L. Thomas. “Triply Periodic Level Surfaces as Models for Cubic Tricontinuous Block Copolymer Morphologies”. In: *Philos. Trans R. Soc. London, Ser. A* 354.1715 (Sept. 1996), pp. 2009–2023. DOI: `10.1098/rsta.1996.0089`. URL: `http://www.jstor.org/stable/54577`.

[MDS09] Kristel Michielsen, H. De Raedt, and Doekele G. Stavenga. “Reflectivity of the gyroid biophotonic crystals in the ventral wing scales of the Green Hairstreak butterfly, Callophrys rubi”. In: *J. Royal Soc. Interf.* 7.46 (Oct. 2009), pp. 765–771. ISSN: 1742-5662. DOI: `10.1098/rsif.2009.0352`.

[Men01] Ralf Menzel. *Photonics*. Springer, 2001. ISBN: 3-540-67074-2.

[MIT] MIT. *MEEP Reference*. URL: `http://ab-initio.mit.edu/wiki/index.php/Meep_Reference` (visited on 11/25/2014).

[MK03] Kristel Michielsen and J. S. Kole. “Photonic band gaps in materials with triply periodic surfaces and related tubular structures”. In: *Phys. Rev. B* 68.11 (Sept. 2003), p. 115107. DOI: `10.1103/physrevb.68.115107`.

[MS08] Kristel Michielsen and Doekele G. Stavenga. “Gyroid cuticular structures in butterfly wing scales: biological photonic crystals”. In: *J. Royal Soc. Interf.* 5.18 (Jan. 2008), pp. 85–94. DOI: `10.1098/rsif.2007.1065`.

[MTC11] Christian Mille, Eric C. Tyrode, and Robert W. Corkery. “Inorganic chiral 3-D photonic crystals with bicontinuous gyroid structure replicated from butterfly wing scales”. In: *Chem. Commun.* 47.35 (2011), p. 9873. DOI: `10.1039/c1cc11637a`.

[MTC13] Christian Mille, Eric C. Tyrode, and Robert W. Corkery. “3D titania photonic crystals replicated from gyroid structures in butterfly wing scales: approaching full band gaps at visible wavelengths”. In: *RSC Adv.* 3.9 (2013), pp. 3109–3117. DOI: `10.1039/c2ra22506a`.

[Oba11] Salah Obayya. *Computational photonics*. Wiley, 2011. ISBN: 978-0-470-68893-9.

[Oh+12] Sang Soon Oh, Angela Demetriadou, Sebastian Wuestner, and Ortwin Hess. “On the Origin of Chirality in Nanoplasmonic Gyroid Metamaterials”. In: *Adv. Mater.* 25.4 (Oct. 2012), pp. 612–617. DOI: `10.1002/adma.201202788`.

[OJ11] Ardavan Oskooi and Steven G. Johnson. “Distinguishing correct from incorrect PML proposals and a corrected unsplit PML for anisotropic, dispersive media”. In: *J. Comput. Phys.* 230.7 (Apr. 2011), pp. 2369–2377. DOI: `10.1016/j.jcp.2011.01.006`. URL: `http://math.mit.edu/~stevenj/papers/OskooiJo11.pdf`.

[OKe+08] Michael O’Keeffe, Maxim A. Peskov, Stuart J. Ramsden, and Omar M. Yaghi. “The Reticular Chemistry Structure Resource (RCSR) Database of, and Symbols for, Crystal Nets”. In: *Acc. Chem. Res.* 41.12 (Dec. 2008), pp. 1782–1789. DOI: `10.1021/ar800124u`.

[OKJ09] Ardavan F. Oskooi, Chris Kottke, and Steven G. Johnson. “Accurate finite-difference time-domain simulation of anisotropic media by subpixel smoothing”. In: *Opt. Lett.* 34.18 (2009), p. 2778. DOI: `10.1364/ol.34.002778`.

[Osk+08] Ardavan F. Oskooi, Lei Zhang, Yehuda Avniel, and Steven G. Johnson. “The failure of perfectly matched layers, and towards their redemption by adiabatic absorbers”. In: *Opt. Express* 16.15 (2008), p. 11376. DOI: `10.1364/oe.16.011376`.

[Osk+10] Ardavan F. Oskooi et al. “MEEP: A flexible free-software package for electromagnetic simulations by the FDTD method”. In: *Comput. Phys. Commun.* 181.3 (Mar. 2010), pp. 687–702. DOI: `10.1016/j.cpc.2009.11.008`. URL: `http://math.mit.edu/~stevenj/papers/OskooiRo10.pdf`.

[Pap+03] A. Papakostas et al. “Optical Manifestations of Planar Chirality”. In: *Phys. Rev. Lett.* 90.10 (Mar. 2003). DOI: `10.1103/physrevlett.90.107404`.

[Pou12] Caroline Pouya. “Investigating Naturally Occurring 3-Dimensional Photonic Crystals”. PhD thesis. University of Exeter, 2012. URL: `https://ore.exeter.ac.uk/repository/bitstream/handle/10036/3744/PouyaC.pdf?sequence=2`.

[PSB04] Andy C. van Popta, Jeremy C. Sit, and Michael J. Brett. “Optical Properties of Porous Helical Thin Films”. In: *Appl. Opt.* 43.18 (2004), pp. 3632–3639. DOI: `10.1364/ao.43.003632`.

[PSH09] Yong Jun Park, K. M. A Sobahan, and Chang Kwon Hwangbo. “Optical and Structural Properties of a Circular Polarization
Handedness Inverter Prepared by Using Glancing Angle Deposition”. In: *J. Korean Phys. Soc.* 55.32 (Sept. 2009), pp. 1263–1266. DOI: `10.3938/jkps.55.1263`.

[PV12] C. Pouya and P. Vukusic. “Electromagnetic characterization of millimetre-scale replicas of the gyroid photonic crystal found in the butterfly Parides sesostris”. In: *Interface Focus* 2.5 (Oct. 2012), pp. 645–650. DOI: `10.1098/rsfs.2011.0091`.

[Ray87] John W. S. Rayleigh. “On the Maintenance of Vibrations by Forces of Double Frequency, and on the Propagation of Waves through a Medium endowed with a Periodic Structure”. In: *Phil. Mag.* 24 (1887), pp. 145–159. URL: `http://zs.thulb.uni-jena.de/receive/jportal_jpvolume_00128638`.

[RB97] Kevin Robbie and M. J. Brett. “Sculptured thin films and glancing angle deposition: Growth mechanics and applications”. In: *J. Vac. Sci. Technol. A* 15.3 (May 1997), pp. 1460–1465. DOI: `10.1116/1.580562`.

[RBL95] Kevin Robbie, Michael J. Brett, and Akhlesh Lakhtakia. “First thin film realization of a helicoidal bianisotropic medium”. In: *J. Vac. Sci. Technol. A* 13.6 (Nov. 1995), pp. 2991–2993. DOI: `10.1116/1.579626`.

[Sab+11] Matthias Saba et al. “Circular Dichroism in Biological Photonic Crystals and Cubic Chiral Nets”. In: *Phys. Rev. Lett.* 106 (10 Mar. 2011), p. 103902. DOI: `10.1103/PhysRevLett.106.103902`.

[Sab+13] Matthias Saba et al. “Group theory of circular-polarization effects in chiral photonic crystals with four-fold rotation axes applied to the eight-fold intergrowth of gyroid nets”. In: *Phys. Rev. B* 88 (24 Dec. 2013), p. 245116. DOI: `10.1103/PhysRevB.88.245116`.

[Sab+14] Matthias Saba, Bodo D. Wilts, Johannes Hielscher, and Gerd E. Schröder-Turk. “Absence of Circular Polarisation in Reflections of Butterfly Wing Scales with Chiral Gyroid Structure”. In: *Materials Today: Proceedings* 1 (2014), pp. 193–208. DOI: `10.1016/j.matpr.2014.09.023`.

[Sab10] Matthias Saba. “Band Structure Analysis of Gyroid Photonic Crystals for unpolarized and circular polarized light”. Diploma Thesis. FAU Erlangen, 2010.

[Sar+10] Vinodkumar Saranathan et al. “Structure, function, and self-assembly of single network gyroid ($I4_132$) photonic crystals in butterfly wing scales”. In: *PNAS* 107.26 (June 2010), pp. 11676–11681. DOI: `10.1073/pnas.0909616107`.

[SC10] Wahyu Setyawan and Stefano Curtarolo. “High-throughput electronic band structure calculations: Challenges and tools”. In: *Comput. Mater. Sci.* 49.2 (Aug. 2010), pp. 299–312. DOI: `10.1016/j.commatsci.2010.05.010`.

[Sch+11] Gerd E. Schröder-Turk et al. “The chiral structure of porous chitin within the wing-scales of Callophrys rubi”. In: *J. Struct. Biol.* 174.2 (May 2011), pp. 290–295. DOI: `10.1016/j.jsb.2011.01.004`.

[Sch70] Alan H. Schoen. *Infinite periodic minimal surfaces without self-intersections.* Technical Note D-5441. NASA, May 1970. URL: `http://ntrs.nasa.gov/archive/nasa/casi.ntrs.nasa.gov/19700020472.pdf`.

[SN91] H. G. von Schnering and R. Nesper. “Nodal surfaces of Fourier series: Fundamental invariants of structured matter”. In: *Z. Physik B – Condensed Matter* 83.3 (Oct. 1991), pp. 407–412. DOI: `10.1007/bf01313411`.

[SS15] Matthias Saba and Gerd E. Schröder-Turk. “Bloch Modes and Evanescent Modes of Photonic Crystals: Weak Form Solutions Based on Accurate Interface Triangulation”. In: *Crystals* 5.1 (2015), pp. 14–44. DOI: `10.3390/cryst5010014`.

[TH05] Allen Taflove and Susan C. Hagness. *Computational Electrodynamics: The Finite-Difference Time-Domain Method.* Third edition. Artech House, 2005. ISBN: 1-58053-832-0.

[Thi+07] Michael Thiel et al. “Polarization Stop Bands in Chiral Polymeric Three-Dimensional Photonic Crystals”. In: *Adv. Mater.* 19.2 (Jan. 2007), pp. 207–210. DOI: `10.1002/adma.200601497`. URL: `http://www.researchgate.net/profile/Georg_Von_Freymann/publication/36454021_Polarization_Stop_Bands_in_Chiral_Polymeric_Three-Dimensional_Photonic_Crystals/links/09e4151190a4e474af000000.pdf`.

[Thi+10] Michael Thiel, H. Fischer, G. von Freymann, and M. Wegener. “Three-dimensional chiral photonic superlattices”. In: *Opt. Lett.* 35.2 (2010), pp. 166–168. DOI: `10.1364/ol.35.000166`.

[TJ01] Ovidiu Toader and Sajeev John. “Proposed Square Spiral Microfabrication Architecture for Large Three-Dimensional Photonic Band Gap Crystals”. In: *Science* 292.5519 (May 2001), pp. 1133–1135. DOI: `10.1126/science.1059479`.

[VKH08] Peter Vukusic, Robert Kelly, and Ian Hooper. “A biological sub-micron thickness optical broadband reflector characterized using both light and microwaves”. In: *J. R. Soc. Interface* 6.Suppl. 2 (Nov. 2008), S193–S201. DOI: `10.1098/rsif.2008.0345.focus`.

[Was13] Tony Wasserka. *Circular Dichroism of Single-Gyroids in the presence of structural disorder and noise.* FAU *Physics Advanced* research project. Nov. 2013.

[Woh+01] Meinhard Wohlgemuth, Nataliya Yufa, James Hoffman, and Edwin L. Thomas. “Triply Periodic Bicontinuous Cubic Microdomain Morphologies by Symmetries”. In: *Macromolecules* 34.17 (Aug. 2001), pp. 6083–6089. DOI: `10.1021/ma0019499`.

[WP96] A. J. Ward and John B. Pendry. “Refraction and geometry in Maxwell’s equations”. In: *J. Mod. Opt.* 43.4 (Apr. 1996), pp. 773–793. DOI: `10.1080/09500349608232782`.

[Yab87] Eli Yablonovitch. “Inhibited Spontaneous Emission in Solid-State Physics and Electronics”. In: *Phys. Rev. Lett.* 58.20 (May 1987), pp. 2059–2062. DOI: `10.1103/physrevlett.58.2059`.

[Yee66] Kane S. Yee. “Numerical solution of initial boundary value problems involving maxwell’s equations in isotropic media”. In: *IEEE Trans. Antennas Propagat.* 14.3 (1966), pp. 302–307. DOI: `10.1109/tap.1966.1138693`.

[Yeh79] Pochi Yeh. “Electromagnetic propagation in birefringent layered media”. In: *J. Opt. Soc. Am.* 69.5 (1979), pp. 742–756. DOI: `10.1364/josa.69.000742`.

[YGL91] Eli Yablonovitch, T. J. Gmitter, and K. M. Leung. “Photonic Band Structure: The Face-Centered-Cubic Case Employing Nonspherical Atoms”. In: *Phys. Rev. Lett.* 67.17 (1991), pp. 2295–2298. DOI: `10.1103/PhysRevLett.67.2295`.

Epigraph image sources

Page 5 Carl Spitzweg, 1840. *Public domain,* `https://commons.wikimedia.org/wiki/File:Carl_Spitzweg_033.jpg`

Page 11 © 1973 Harvest/Capitol, Storm Thorgerson, Pink Floyd, Discogs `http://cdn.discogs.com/JK5shYwhSbRDxyvMPKMAYh4cL3c=/fit-in/600x598/filters:strip_icc():format(jpeg):mode_rgb():quality(96)/discogs-images/R-1786256-1404031531-5731.jpeg.jpg`

Page 27 Scanned from *The Magic of M. C. Escher.* (Harry N. Abrams, Inc. ISBN 0-8109-6720-0) `https://en.wikipedia.org/wiki/File:DrawingHands.jpg`

Page 47 Adolph von Menzel, 1875. *Public domain,* `https://commons.wikimedia.org/wiki/File:Adolph_Menzel_-_Eisenwalzwerk_-_Google_Art_Project.jpg`

Page 79 Edvard Munch, 1893. *Public domain,* `https://commons.wikimedia.org/wiki/File:The_Scream.jpg`

Page 109 Cornelis Gijsbrechts, 1675. *Public domain,* `https://commons.wikimedia.org/wiki/File:Cornelis_Norbertus_Gysbrechts_002.jpg`

Acknowledgements

Forgiveth me! the gentle reader: might
He come across with stains on consequence
Bewitnessed—in the decent blank verse's metrum
Throughout these meek acknowledgements.
This thesis has *(of course)* to be understood
As a chain link in both a professional

And a social context. With respect to the former,
My gratitude be expressed to Gerd Schröder-Turk,
Whose curiosity infected me, and who encouraged
My challenges on this thesis,
Occasionally came across with fun new ideas—
And hosted my presence at Theorie I in Erlangen.

My particular thanks has Matthias to bear,
For all the prolific discussions, and for sharing
His comprehensive expertise in structure-photonics.
(Alongside profound insights in Stirling engines.)
Moreover, his professional and structural stimulations
Have left their mark throughout this text.

A stanza be dedicated to the technical
Embedment, which made this work possible:
Foremost, of coarse, our all Favourite Admins,
Nourishing Theory I's formidable technical infrastructure.
And all those comfortable FOSS projects of which
LaTeX, gnuplot, vim, hg, and MEEP are an incomplete list.

Finally, the "soft" conditions catch their
Legitimate mentioning: Immeasurable
Gratefulness to my dear and patient family.
And (seasoned with subtle irony) all those
Happy/puzzling distractions, including "Pfeifen",[82]
And 02.585$^{\text{MT}}$ Citrus Share, Inc. *(Canned laughter. Exeunt.)*

—14.3.2015

---

[82] Special thanks to Simon Weis and his handy `\usepackage{chngcntr}\counterwithout{footnote}{chapter}` hack to continuate footnote numberings throughout the whole document.

Erklärung

Hiermit versichere ich, die vorliegende Masterarbeit selbstständig und nur unter Verwendung der angegebenen Hilfsmittel und Quellen angefertigt zu haben. Ich erkläre weiterhin, dass alle Stellen der Arbeit, die wörtlich oder sinngemäß aus anderen Quellen übernommen wurden, als solche kenntlich gemacht sind, und dass die Arbeit in gleicher oder ähnlicher Form noch keiner Prüfungsbehörde vorgelegt wurde.

Erlangen, 15. März 2015

Johannes Hielscher